THE THERMO-MECHANICAL COUPLED ANALYSIS OF FIRE INDUCED DAMAGE FOR UNDERGROUND MINES WITH VARIOUS GEOMECHANICAL DOMAINS

A THESIS SUBMITTED TO
THE GRADUATE SCHOOL OF NATURAL AND APPLIED SCIENCES
OF
MIDDLE EAST TECHNICAL UNIVERSITY

BY

ALAK ABDULSATAR ABDULJABAR ABDULJABAR

IN PARTIAL FULFILLMENT OF THE REQUIREMENTS
FOR
THE DEGREE OF MASTER OF SCIENCE
IN
MINING ENGINEERING

JUNE 2025

Approval of the thesis:

THE THERMO-MECHANICAL COUPLED ANALYSIS OF FIRE INDUCED DAMAGE FOR UNDERGROUND MINES WITH VARIOUS GEOMECHANICAL DOMAINS

submitted by **ALAK ABDULSATAR ABDULJABAR ABDULJABAR** in partial fulfillment of the requirements for the degree of **Master of Science** i**n Mining Engineering, Middle East Technical University** by,

Prof. Dr. Naci Emre Altun
Dean, **Graduate School of Natural and Applied Sciences** _____

Prof. Dr. Naci Emre Altun
Head of the Department, **Mining Engineering** _____

Assist. Prof. Dr. Ahmet Güneş Yardımcı
Supervisor, **Mining Engineering, METU** _____

Examining Committee Members:

Prof. Dr. Bahtiyar Ünver
Mining Engineering, Hacettepe University _____

Assist. Prof. Dr. Ahmet Güneş Yardımcı
Mining Engineering, METU _____

Assist. Prof. Dr. Kutay Emre Karadeniz
Mining Engineering, METU _____

Date: 11.06.2025

I hereby declare that all information in this document has been obtained and presented in accordance with academic rules and ethical conduct. I also declare that, as required by these rules and conduct, I have fully cited and referenced all material and results that are not original to this work.

Name Last name : Alak Abdulsatar Abduljabar Abduljabar

Signature :

ABSTRACT

THE THERMO-MECHANICAL COUPLED ANALYSIS OF FIRE INDUCED DAMAGE FOR UNDERGROUND MINES WITH VARIOUS GEOMECHANICAL DOMAINS

Abduljabar, Alak Abdulsatar Abduljabar
Master of Science, Mining Engineering
Supervisor : Assist. Prof. Dr. Ahmet Güneş Yardımcı

June 2025, 92 pages

Mine fires pose a serious threat to the stability of underground excavations due to complex thermo-mechanical effects on the surrounding rock mass. Understanding the fire-induced damage requires coupled thermo-mechanical assessments and mechanical outcomes are dependent on the geomechanical conditions. Accordingly, this study models the fire-induced damage zone (FIDZ) around a typical underground mine haul road for three different rock mass quality classes representing hard rocks to observe their response to increasing temperatures. The mechanical effects were quantified while changing the scale of the fire and the support configurations. Numerical results show that the damage initiated earlier in lower geomechanical settings. In high quality rocks, the FIDZ concentrates mainly around the crown and sharp edges, while in lower qualities the region extends further to the walls and floor, and the damage zone becomes more uniform around the opening. The presence of excavations above and below the fire zone was observed to influence the progression of the damage. The tension between the bolts and

excavation boundary is affected by fire, resulting in bolt failure between 500°C and 900°C. Experimental remarks showed a temporary increase in strength and stiffness up to 400°C and degradation started only after these levels. In this perspective, classical material constitutive models are questioned in terms of lacking to represent the dependency of mechanical parameters to the temperature change.

Keywords: Underground Mine Fire, Fire Induced Damage, Coupled Geomechanical Simulation

ÖZ

FARKLI JEO-MEKANİK ALANLARA SAHİP YER ALTI MADENLERİNDE YANGIN KAYNAKLI HASARIN TERMOMEKANİK BAĞLANTILI ANALİZİ

Abduljabar, Alak Abdulsatar Abduljabar
Yüksek Lisans, Maden Mühendisliği
Tez Yöneticisi: Dr. Öğr. Üyesi Ahmet Güneş Yardımcı

Haziran 2025, 92 sayfa

Maden yangınları, çevredeki kaya kütlesi üzerinde ortaya çıkan karmaşık termo-mekanik etkiler nedeniyle yer altı kazılarının stabilitesi açısından ciddi bir tehdit oluşturmaktadır. Yangın kaynaklı hasarın doğru bir şekilde anlaşılabilmesi, eşlenik termo-mekanik analizleri gerektirmekte olup, mekanik sonuçlar büyük ölçüde jeomekanik koşullara bağlıdır. Bu çalışmada, artan sıcaklıklara karşı tepkileri gözlemlenmek üzere sert kayaçları temsil eden üç farklı kaya kütlesi kalite sınıfı için, tipik bir yer altı maden taşıma yolu etrafındaki yangın kaynaklı hasar bölgesi (FIDZ) modellenmiştir. Yangın ölçeği ve destek sistemleri değiştirilirken, mekanik etkiler nicel olarak değerlendirilmiştir. Sayısal analiz sonuçları, düşük jeomekanik kaliteye sahip ortamlarda hasarın daha erken başladığını ortaya koymaktadır. Yüksek kaliteli kayaçlarda FIDZ, esasen tavan ve keskin kenarlar etrafında yoğunlaşırken; düşük kaliteli kayaçlarda bu bölge yan duvarlar ve tabana kadar genişlemekte ve hasar bölgesi açıklık çevresinde daha homojen bir dağılım sergilemektedir. Yangın bölgesinin üstünde ve altında bulunan diğer kazıların varlığının hasarın ilerlemesini

etkilediği gözlemlenmiştir. Cıvatalar ile kazı sınırları arasındaki gerilim yangından etkilenmekte olup, 500°C ile 900°C arasındaki sıcaklıklarda cıvata kopmaları meydana gelmektedir. Deneysel bulgular, 400°C'ye kadar malzemenin mukavemet ve rijitliğinde geçici bir artış gözlemlendiğini ve bozulmanın bu sıcaklık seviyelerinden sonra başladığını göstermektedir. Bu çerçevede, klasik malzeme davranış (konstitutif) modellerinin, mekanik parametrelerin sıcaklık değişimlerine olan bağımlılığını yeterince temsil edemedikleri sorgulanmaktadır.

Anahtar Kelimeler: Yer Altı Maden Yangını, Yangın Kaynaklı Hasar, Eşlenik Jeomekanik Simülasyon

To my loved ones

ACKNOWLEDGMENTS

I would like to express my thanks to my supervisor, Assist. Prof. Dr. Ahmet Güneş Yardımcı, for his immense guidance, support, and thoughtful feedback throughout the course of my degree. His expertise, patience, and encouragement have shaped my research and helped me grow both academically and personally. I consider myself truly fortunate to have had the opportunity to gain experience under his supervision.

Extending my appreciation, I would like to thank my thesis defense jury members– Prof. Dr. Bahtiyar Ünver from Hacettepe University and Assist. Prof. Dr. Kutay Emre Karadeniz from METU–for their critical feedback and fruitful discussions during my thesis defense.

I would like to give heartfelt thanks to my parents for all their sacrifices and for encouraging me to be at my fullest potential. I am grateful for my mother, Faten Abdullah; my father, Abdulsatar Abduljabbar; and my siblings, Wid, Tasneem, and Ahmad, for their unconditional love, support, and encouragement throughout. Their belief in me, especially in moments of self-doubt, gave me immense strength to push through my boundaries and is what kept me going forward.

Drafting this thesis has been both a challenging and an enriching experience, and I am very thankful to everyone who has played a part in supporting me along the way.

TABLE OF CONTENTS

ABSTRACT v

ÖZ vii

ACKNOWLEDGMENTS x

TABLE OF CONTENTS xi

LIST OF TABLES xiii

LIST OF FIGURES xiv

CHAPTERS

1 INTRODUCTION 1

1.1 Problem Statement 1

1.2 Research Objectives 2

1.3 Research Methodology 3

1.4 Research Scope 5

1.5 Structure of the Thesis 5

2 LITERATURE REVIEW 7

2.1 Implementation of Thermo-Coupled Modelling in RS2 16

2.2 Prediction of Geomechanical Parameters 17

3 PARAMETRIC ANALYSIS OF A HYPOTHETICAL MINE FIRE 21

3.1 Determination of Domains and Mechanical Properties 22

3.1.1 Geomechanical Properties Before Thermal Effects 23

3.1.2 Geomechanical Properties After Thermal Damage 27

3.2 Support Configurations for the Specified Rock Mass Quality Classes 35

3.3 Model Geometry and Boundary Conditions 36

3.4 Assessment of Fire Induced Damage Zone (FIDZ) with Thermocoupled Models 37
4 RESULTS AND DISCUSSION 41
4.1 Mining Induced Stresses Around the Openings 41
4.2 Fire Induced Damage in a Small-Scale Fire 42
4.3 Fire Induced Damage in a Large-Scale Fire 47
4.4 Effects of Road Grade on the Fire Induced Damage 53
4.5 Comparitive Analysis between Mechanical Modelling and Coupled Thermomechanical Modelling 66
5 CONCLUSION 73
REFERENCES 77
APPENDICES 83
A. Stress-Strain Curves for Static Deformability Tests 83
B. Stress-Strain Curves for Triaxial Compression Tests 86
C. Total Displacement Contours for Coupled Thermo-Mechanical Models 89

LIST OF TABLES

TABLES

Table 2.1. Summary table listing the major outcomes from the literature survey.. 11
Table 2.2. Empirical formulas for the uniaxial compressive strength (UCS) of rock mass..... 18
Table 2.3. Empirical formulas for Young's modulus (E) of rock mass..... 18
Table 2.4. Empirical formulas for the internal friction angle (ϕ) of rock mass..... 19
Table 2.5. Empirical formulas for poisson's ratio (ν) for rock mass..... 19
Table 3.1. The mechanical parameters assigned to the model domains. 25
Table 3.2. Bolt pattern for the specified rock mass quality classes. 36
Table 3.3. Mechanical properties of the bolts used..... 36
Table 3.4. Stages in the model with corresponding temperature, analysis type, and duration. 38
Table 3.5. Thermal parameters used in the models. 39
Table 4.1. Summary of the numerical outcomes. 53
Table 4.2. Material properties used in the mechanical models for VGQRM. 66
Table 4.3. Material properties used in the mechanical models for GQRM. 67
Table 4.4. Material properties used in the mechanical models for FQRM. 67

LIST OF FIGURES

FIGURES

Figure 1.1. Flowsheet of the computational study. 4
Figure 3.1. Parametric models of mine fire simulations. 22
Figure 3.2. Experimental setups for (a) Static deformability test, (b) Triaxial compression test, (c) Indirect tensile strength test, and (d) molten specimen after pre-treatment of 1100°C. 29
Figure 3.3. Trend of axial stress vs axial strain in (a) Static deformability test for three specimens, and (b) Triaxial compression test at different lateral compression values at room temperature. 30
Figure 3.4. Trend of (a) uniaxial compressive strength and (b) elastic modulus in samples treated with different temperature levels for 1, 7, and 14 days. 31
Figure 3.5. Trend of confined compressive strength in samples treated with different temperature levels for long term tests (14 days). 32
Figure 3.6. Trend of (a) confined elastic modulus, (b) cohesion, and (c)_internal friction angle in samples treated with different temperature levels for long term tests (14 days). 33
Figure 3.7. Trend of Poisson's ratio according to (a) static deformability tests (treated for 1, 7, and 14 days), and (b) triaxial compression tests (treated for 14 days). 34
Figure 3.8. Trend of tensile strength in samples treated for 14 days..... 35
Figure 3.9. Model view of the ramp cross-section in 2D, with clippings of front view (Left) and cross-section of a typical excavation in VGQRM (Right). 37
Figure 3.10. Temperature-time curve of fuel-controlled fires (Ma and Makelainen, 2000). 39
Figure 3.11. Model view of the ramp cross-section showing the thermal boundaries with snippet of thermal boundaries around one of the excavations in VGQRM. ... 40

Figure 4.1. The cross-section view showing stress contours around supported excavations of a ramp for VGQRM, GQRM, and FQRM. 42
Figure 4.2. The span of the thermal damage zone around L2 in the case of VGQRM (X and Y values represent the maximum horizontal and vertical spans respectively). 43
Figure 4.3. The span of the thermal damage zone around L2 in the case of GQRM (X and Y values represent the maximum horizontal and vertical spans respectively). 44
Figure 4.4. The span of the thermal damage zone in FQRM (X and Y values represent the maximum horizontal and vertical spans respectively). 46
Figure 4.5. The major principal stress ($\sigma 1$) around the fire zone (L2) for all three rock mass classes. 47
Figure 4.6. The extent of the thermal damage zone in VGQRM (X and Y values represent the maximum horizontal and vertical spans respectively). 48
Figure 4.7. The extent of the thermal damage zone in GQRM (X and Y values represent the maximum horizontal and vertical spans respectively). 50
Figure 4.8. The extent of the thermal damage zone in FQRM (X and Y values represent the maximum horizontal and vertical spans respectively). 51
Figure 4.9. Major principal stress ($\sigma 1$) around the fire zones (L2 and R1) for all rock mass classes at 1200°C. 52
Figure 4.10. Stress contours for 10% (above) and 12% (below) road grade cases for 600°C, 900°C, and 1200°C a during a small-scale fire for VGQRM. 54
Figure 4.11. Progression of damaged zone for 10% (above) and 12% (below) road grade cases for 600°C, 900°C, and 1200°C during a small-scale fire for VGQRM. 55
Figure 4.12. Stress contours for 10% (above) and 12% (below) road grade cases at 1050°C during a large-scale fire for VGQRM. 56
Figure 4.13. Progression of damaged zone for 10% (above) and 12% (below) road grade cases at 1050°C during a large-scale fire for VGQRM. 58

Figure 4.14. Maximum stress contours for 10% (above) and 12% (below) road grade cases for 600°C, 900°C, and 1200°C during a small-scale fire for GQRM. 59
Figure 4.15. Progression of fire-induced damaged zone (FIDZ) for 10% (above) and 12% (below) road grade cases for 600°C, 900°C, and 1200°C during a small-scale fire for GQRM. 60
Figure 4.16. Stress contours for 10% (above) and 12% (below) road grade cases at 1200°C during a large-scale fire for GQRM. 61
Figure 4.17. FIDZ for 10% (above) and 12% (below) road grade cases at 1200°C during a large-scale fire for GQRM. 62
Figure 4.18. Stress contours for 10% (above) and 12% (below) road grade cases for 600°C, 900°C, and 1200°C during a small-scale fire for FQRM. 63
Figure 4.19. Development of FIDZ for 10% (above) and 12% (below) road grade cases for 600°C, 900°C, and 1200°C during a small-scale fire for FQRM. 64
Figure 4.20. Development of FIDZ for the 10% (above) and 12% (below) road grade cases at 1200°C during a large-scale fire for FQRM. 65
Figure 4.21. Variations in the damage zone around the opening L2 in VGQRM in mechanical model (left) and coupled thermo mechanical model (right) at 1000°C. 68
Figure 4.22. Variations in $\sigma 1$ around the opening L2 in VGQRM in mechanical model (left) and coupled thermo mechanical model (right) at 1000°C. 69
Figure 4.23. Variations in the damage zone around the opening L2 in GQRM in mechanical model (left) and coupled thermo mechanical model (right) at 1000°C. 69
Figure 4.24. Variations in $\sigma 1$ around the opening L2 in GQRM in mechanical model (left) and coupled thermo mechanical model (right) at 1000°C. 70
Figure 4.25. Damage zone surrounding L2 in mechanical model (left) and coupled thermo mechanical model (right) at 1000°C in FQRM. 71
Figure 4.26. Variations in $\sigma 1$ around the opening L2 in mechanical model (left) and coupled thermo mechanical model (right) at 1000°C in FQRM. 71

CHAPTER 1

INTRODUCTION

Mine fires are a commonly occurring risk in underground mines and tunnels. Such an event poses a high risk to the stability of the underground structures and to the safety of the personnel, leading to significant economic losses. Studies on the nature of underground fires have shown a rapid increase of temperatures within a few minutes of the onset of fire. Such high temperatures may exceed the melting point of the rock mass and of the support materials used in the mine and tunnel excavations. In many cases, mine fires burn for hours before extinguishing. This gives rise to the need to understand the degrading effects of high temperatures, coupled with mechanical effects on underground excavations. Recent research has mainly focused on support systems and rescue plans, while less emphasis has been given to the effects on the rock mass itself. A thorough understanding of thermomechanical effects is essential for improving the design of underground excavations and associated safety management systems. This thesis addresses the coupled TM effects of mine fires in a hypothetical mine ramp model with different classes of rock mass quality under various parameters.

1.1 Problem Statement

Research on fires in underground spaces has mainly focused on their impact on the concrete lining, the support elements used, ventilation systems, and emergency plans used for rescue. However, the effects of the fire on the geomechanical properties of the surrounding rock mass are poorly understood.

Existing studies on the coupled thermomechanical (TM) effects of fire in underground spaces are limited by temperature range and rock types.

This lack of in-depth research on fires–particularly mine fires–leads to a generalized understanding of fire effects and results in incorrect perceptions of how mine fires affect different rock mass qualities and how they respond to rapidly increasing temperatures. This often leads to inadequate support designs for underground openings and poor preparedness for such events. There is a clear need to understand the TM-coupled effects of fire on different rock mass qualities in order to have better design features for support systems and improve fire management in fire-prone underground excavations.

1.2 Research Objectives

The aim of this work is to investigate the damaging effects of fire on the geomechanical properties of underground excavations in hard rock mass by considering different rock mass quality classes, support configurations, and mine ramp layout designs. This study aims to provide a thorough understanding of the geomechanical behavior of the rock mass before the occurrence of fire, the coupled thermomechanical effects during the onset of fire and until it reaches its peak temperature, and the mechanical effects on the rock mass after the fire is extinguished. This goal is achieved by computing the fire-induced damage zone (FIDZ) and the stress contours around the excavations at the different stages in a progressive manner and by comparing these parameters among different model setups. The outcomes from this research provide a complete understanding of the effects of mine fires and can be used in improving the support design and fire management plans in the future.

1.3 Research Methodology

This study employs experimental and computational analyses for interpretation of thermomechanical impacts of fire on hard rocks in underground mines. In the experimental stage, hard rock cores were subjected to various temperature levels over different time spans. After thermal treatment, changes in geomechanical properties were observed by standard rock mechanics tests. In the numerical part, a typical underground mine ramp was simulated. The model input parameters were identified as the model geometry, the domains, the boundary conditions, the geomechanical parameters, and the thermal parameters. The radius of curvature and the grade of the ramp were derived from common mine ramp designs. Three geological domains presenting common quality classes in hard rocks were selected for very good, good, and fair rock mass conditions. The thermal boundary conditions were defined based on previous studies investigating field-scale underground mine fires. The geomechanical properties were assigned to the domains using the empirical correlations and test results (lab & in situ) in the literature. Similarly, the thermal parameters were determined from experimental studies on thermo-mechanical properties of Andesite samples. For the hypothetical ramp model, the relevant support configurations were selected from the suggestions of the Q-tunneling index system.

Model solutions were conducted in two progressive stages. In the first stage, the mechanical solution reveals the excavation-induced stress and deformations around the openings. The second stage of the solution executes thermal sources and boundary conditions to observe the temperature-related damage zone around the openings. Mine fires were simulated on small and large scales. The associated coupled thermomechanical (TM) damage effects were examined in both scales. The stress distribution, the performance of bolts with increasing temperature, and the propagation of plastic damage zones around fire regions were quantified for each model.

To ensure the reliability of simulations, the fire-induced damage zone formed in the post-fire stages was validated against previously documented mine fire incidents from literature. The comparison focused on the span and progression of the plastic damage zone in mine fire cases within a similar quality of rock mass. The effects of temperature on bolts were compared to reported cases of mining and tunnel fires. The failure temperature and progressive damage of the bolts were compared. Figure 1.1 shows the flowsheet of the computational study.

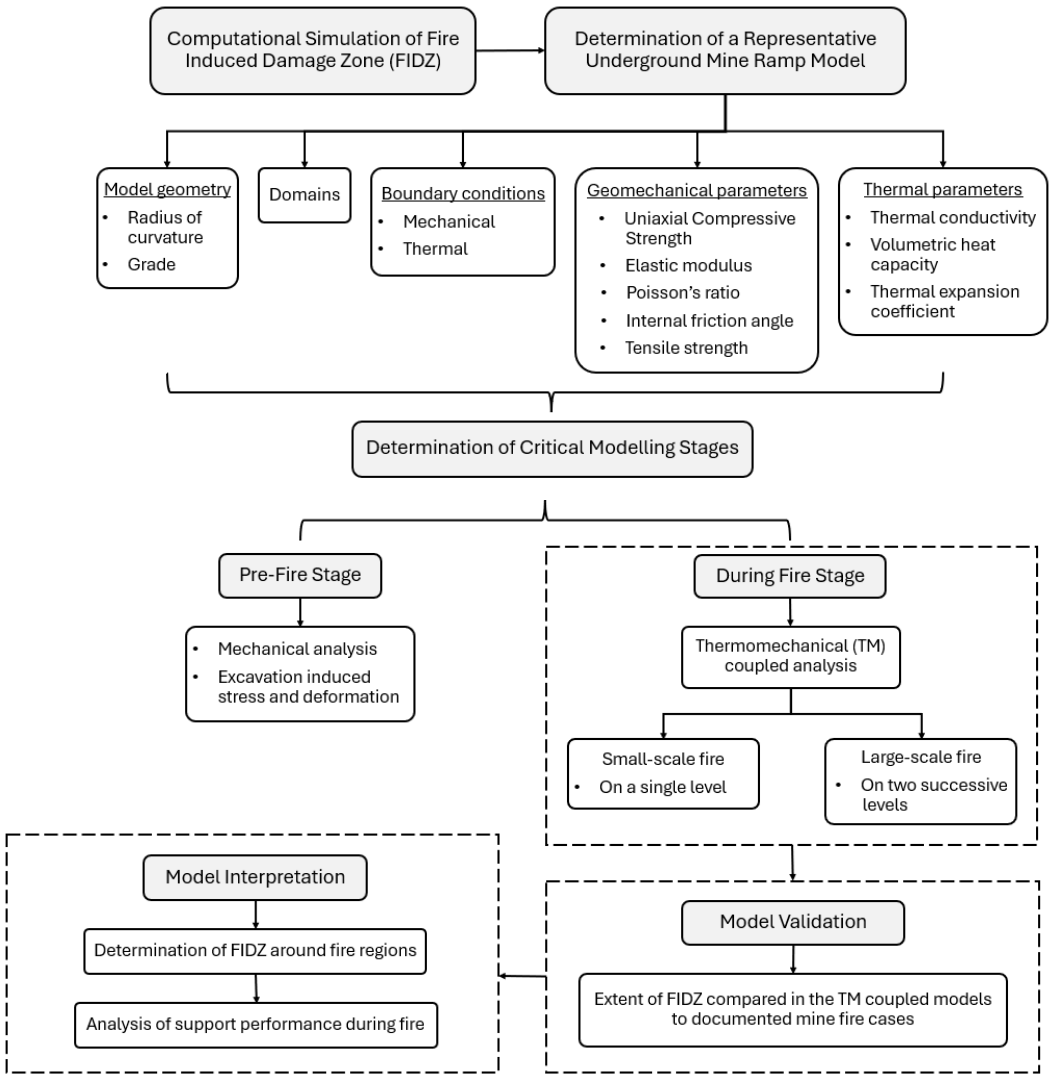

Figure 1.1. Flowsheet of the computational study.

1.4 Research Scope

This study explores the effects of high temperatures induced by mine fires on the behavior of different geomechanical domains in hard rocks. Both experimental and computational analyses were carried out to estimate the damaging effects of high temperatures during and after a mine fire event and to characterize its effects on the mechanical parameters of hard rocks. Coupled thermo-mechanical (TM) models were used to simulate the effects of the scale of fire, support configurations, and road grades for a hypothetical underground mine ramp environment. This study focused on finding the location and extent of the fire-induced damage zone (FIDZ) across different scenarios. The outcomes of this study reveal the changes in the fire-induced damage zone (FIDZ) and stress field under varying configurations.

1.5 Structure of the Thesis

This thesis includes a total of five chapters. An overview of the contents of each chapter is given in this section. Chapter 1 introduces the topic, starting with the negative effects of mine fires on underground spaces. It includes a problem statement that highlights the lack of research done on mine fires and their effects on the surrounding rock mass and a brief methodology of this work. The second chapter is a detailed literature review on the effects of fires in closed spaces such as tunnels and underground mines. This section also involves studies performed on different rock types to observe the change in their mechanical properties when exposed to high temperatures. Experimental and numerical simulations of tunnel fires are also included from previous studies, and the effects of high temperatures on the rock mass and supports is briefly introduced. Chapter 3 is the heart of this thesis. This chapter is titled “Parametric analysis of a hypothetical mine fire”. The first section of this chapter covers the choice of geological domains considered in this work. This section also involves all the literature-based selection of mechanical parameters for the

different rock mass classes before the occurrence of a mine fire and the experiment-based mechanical properties after the mine fire. The selection of the supports are discussed in the second section. The third section describes the model geometry and boundary conditions. The last section of this chapter revolves around the assessment of the fire-induced damage zone (FIDZ) with thermocouple models. Chapter 4 is the results and discussion, where all the findings are discussed and the interpreted models are compared. Chapter 5 covers the conclusion of this work.

CHAPTER 2

LITERATURE REVIEW

Fires occurring in underground spaces (like mines or tunnels) may lead to catastrophic incidents, such as loss of life or substantial economic consequences. Current research in experimental rock mechanics and observations from case histories support that thermal damage compromises the mechanical integrity of the rock mass and the condition of support elements. For example, Smith and Pells (2008) observed the impact of fire on sandstone in terms of spalling that was triggered at temperatures as low as 110°C due to a constant decrease of uniaxial compressive strength (UCS) of the rock and increase in strain. In Lappeenrata tunnel fire, mobilization of rock blocks as heavy as 400 kg was observed at the roof, where the temperature reached 210°C (Keski-Rahkonen et al., 1986). In the Runehamar tunnel fire, rock blocks fell from the roof when temperatures reached 800-1000°C (Lönnermark and Ingason, 2003). In a fire test performed by Palmqvist (1998), as quoted in Larsson (2006), it was observed that the shotcrete layer as well as the surrounding rock were heavily fractured, so much so that some rocks were easily removed by hand.

Experimental studies into the thermal damage have demonstrated that exposure to high temperatures can yield complex effects on the physical and mechanical properties of diverse rock types. For instance, Xu et al. (2008) treated granite samples to temperatures up to 1300°C and observed a decrease in their UCS with increasing temperature. The failure mode has also changed with increasing temperature, which was brittle to semi-brittle failure under 800°C, semi-ductile failure over 800°C, and plastic behavior at 1200°C. On the other hand, Li et al. (2019) observed an increase in the strength of andesite samples above 500°C due to

sealing of cracks by partially melted clay content. To investigate the impact of tunnel fire on hard rock tunnels, Nordlund et al. (2014) performed mechanical tests on granite, gabbro, and schist specimens, which were exposed to temperatures up to 1100°C. It was observed that the UCS increased with increasing temperature till 400°C and then decreased sharply afterwards. A decrease in Young's modulus and tensile strength, as well as an increase in microcracks, were also observed, especially when temperatures were above 400°C. Another study by Wang and Konietzky (2019) used laboratory experiments and coupled simulations to investigate the Thermo-Mechanical (TM) behavior of granite samples under load. The UCS revealed an increasing trend from 25 to 300°C and decreased afterwards. In addition, simulations under a temperature of 800°C demonstrated that microscopic indicators of thermal damage start at low temperatures, while macroscopic thermal cracks become visible only between 600 and 800°C.

Despite the heating stage being commonly accused of the majority of the thermal damage, rapid cooling by fire extinguishers can also significantly alter the residual strength of rock mass (Wang et al., 2019; Fehérvári, 2008). Experimental study of Ge et al. (2021) on granite samples confirms that exposure to high temperatures followed by a rapid cooling stage intensifies degradation of geomechanical properties. The effect of the cooling rate on the rock is nearly as important as the heating rate, since the sudden cooling of the rocks following tunnel fires can lead to thermal shock (Wasantha et al., 2021). Wang et al. (2019) studied the effects of high-speed heating and cooling on granite samples. It was observed that the specimen cooled to temperatures below 150°C experienced thermal shock. Another study showed that a cooling-induced fracture zone (CIFZ) was formed on granite samples that were cooled down after high-speed heating; however, this was followed by a shrinkage and closure of cracks, increasing the UCS and compaction of the specimen (Wang et al., 2020). Kim et al. (2014) exposed igneous, sedimentary, and metamorphic rocks to high temperature followed by rapid cooling. They reported crack initiation, propagation, and a decrease in tensile strength in granite, diabase,

and Cretaceous volcanic sediments, while microcrack closure and an increase in tensile strength were observed in rocks like quartzite, skarn, and other diabase.

Support elements are also affected by thermal damage in terms of mechanical performance. In their parametric study on the post-fire behavior of a tunnel shield, Lu et al. (2024) proved that fire induces crack propagation, spalling, and deterioration of concrete and bolts. It was found that below 200°C, spalling was the primary reason for reducing residual strength by 36%, whereas concrete and bolt deterioration at temperatures higher than 200°C reduces strength by 28% and 20%, respectively. Above 600°C, the stiffness of the concrete liner decreases by 50%, followed by a breakdown at 800-900°C and melting by 1200°C (Erdakov and Khokhryachkin, 2005). Such plastic behavior is also observed in steel reinforcements at 1100-1200°C (Jha et al., 1998). In a parallel study by Wasantha et al. (2021), bolts and anchors were found to lose most of their capacity at 300-400°C. Lahouar et al. (2018) performed a validation test on post-installed rebars in a concrete slab by subjecting them to fire. It was found that the rebars had a thermal gradient along their length, with a change of 55% in temperature along a length of 135 mm.

While the severity of the resulting damage is mainly influenced by the duration of a fire, there are other factors contributing to the overall impact. These include the source of fire, the type of surrounding rock, ventilation systems, and the combustible materials present in the underground space (Hansen, 2019). Current knowledge on the characteristics of underground fires relies on field-scale trial fires, laboratory models, and computational simulations. For instance, mine fire models of Fernández-Alaiz et al. (2020) showed that under different ventilation conditions in a mine, the temperature-time curve presents a rapid increase of temperature to a peak value in the initial stages, followed by stabilization and a gradual decay. In advance, studies by Lowndes et al. (2006) revealed the temperature gradient during a mine fire, which is higher at the source and decreases through the roof of excavation.

Researchers have also looked into the behavior of fire depending on the combustible materials found in underground environments. Hansen (2023) found that hydraulic hoses exhibited the highest heat release rates in an underground mine, followed by low-voltage cables, cab interiors, and tires. It was also observed that pool fires have more severe effects; however, line fires attained peak temperature more rapidly when fueled by electrical cables than by hydraulic hoses. Moreover, Tang et al. (2022) observed that electrical cables closer to the ceiling burned faster than those farther away, and iron cable hooks were observed to slow down the spread of fire by hindering the flow of air. A numerical and experimental study by Yuan et al. (2014) revealed the behavior of a conveyor belt in an underground tunnel when exposed to fire. Large-scale fire experiments on a conveyor belt showed that the temperature on its surface first reached 650°C within 5 minutes and over 900°C within 10 minutes of ignition. These were seen to decrease with increasing distance from the ignition source. The presence of wood–besides coal–significantly increased the spread of fire on the conveyor belt in the 2014 Soma-Manisa underground coal mine accident. This provided an additional combustible material to fuel the fire (Aksoy et al., 2024). Gao et al. (2021) performed experimental and numerical analysis on a timber-lined tunnel. The presence of timber provided a continuous fuel layer and guided the flow of fire, and the fire was also observed to intensify along the vertical direction and slow down at the corners of the timber-lined walls. A study on flame-retardant cables in underground mines showed that ventilation conditions affect the ignition process. While moderate wind speeds fuel the combustion, spreading it further to the rest of the cable, high-speed winds restrain the combustion process (Ke et al., 2020).

Besides the control parameters, understanding the root cause of underground mine fires is embraced as a key for efficient fire management. Investigations by Hansen (2013, 2010) on Swedish mines between 1988 and 2010 point out that vehicle fire is the most common, which is typically caused by electrical sources (171 cases), flammable liquids (99 cases), and flammable solids ignited by hot surfaces (37 cases). Observations on fires caused by diesel- and electric-powered vehicles in

underground mines show that the fire lasts at a minimum of 200 minutes and can reach temperatures as high as 1000°C within the first 100 minutes (Hansen, 2017). On the other side, studies of Larsson (2006) on the duration of the tunnel fires from the start until they were completely put out show that the Channel Tunnel fire lasted for 7 hours (Kirkland, 2002), the Mont Blanc Tunnel fire lasted for 53 hours (LaCroix, 2001), the Tauern Tunnel fire lasted for 17 hours (Leitner, 2001), and the St. Gotthard Tunnel fire lasted 36 hours (Turner, 2001). In all these cases, the temperature in the tunnel and near the source reached 1000-1200°C (Abraham and Dérobert, 2003; Larsson, 2006). The summary of the relevant literature work is provided in Table 2.1. This table shows, for each author, the major problem statement and the main solution found from their work.

Table 2.1. Summary table listing the major outcomes from the literature survey.

Authors	Main Study	Major Outcome (s)
Smith and Pells (2008)	Studied the impact of fire on Hawkesbury sandstone through a field test.	Spalling was triggered when rock temperature was 110 °C.
Keski-Rahkonen et al. (1986)	Conducted fire tests in Lappeenranta tunnel where the rock is made up of 90% calcite.	Rock blocks as heavy as 400 kg were observed to fall from the roof, where the temperature reached 210°C.
Lönnermark and Ingason (2003)	Conducted a fire test in Runehamar tunnel in hard gneiss.	Rock blocks fell from the roof when temperatures reached 800-1000°C
Palmqvist (1998), as quoted in Larsson (2006)	A fire test was performed in a rock tunnel.	The shotcrete layer as well as the surrounding rock were heavily fractured, some rocks were easily removed by hand.

Table 2.1. (continued)

Xu et al. (2008)	Treated granite specimens to temperatures up to 1300°C to investigate mechanical behavior.	UCS decreased with increasing temperature. The failure mode changed from brittle to semi-brittle under 800°C, semi-ductile over 800°C, to plastic at 1200°C.
Li et al. (2019)	Thermally cracked Andesite to observe its physical and mechanical properties under pressure.	An increase in the crack density and the strength of andesite samples above 500°C due to the sealing of cracks by partially melted clay content.
Nordlund et al. (2014)	Investigated the impact of fire on hard rock tunnels in Sweden consisting of granite, gabbro, and schist.	UCS increased till 400°C. UCS, Young's modulus and tensile strength decreased, especially after 400°C. Microcracks increased after 400°C in granite and after 750°C in schist.
Wang and Konietzky (2019)	Laboratory experiments and coupled simulations to understand the Thermo-Mechanical (TM) behavior of granite.	UCS increased with increasing temperature at 25-300°C and decreased afterwards. Macroscopic thermal cracks appeared between 600-800°C.
Wang et al. (2019)	Studied the coupled thermomechanical (TM) effects of high-speed heating on granite samples.	High speed heating followed by cooling to 150°C before testing likely crushed the specimens into smaller blocks due to thermal shock.
Fehérvári (2008)	Investigated the characteristics of tunnel fires.	Rapid cooling after a fire significantly alters the residual strength of rock mass.

Table 2.1. (continued)

Ge et al. (2021)	Experimental study on granite samples.	Exposure to high temperatures followed by a sudden cooling stage leads to thermal stress and increases the discontinuity in the rock material.
Wasantha et al. (2021)	Reviewed studies regarding the effects of tunnel fires on the surrounding rock mass.	Sudden cooling after tunnel fires can lead to thermal shock, further degrading the geomechanical properties of the rocks. Explosive spalling is very common in tunnel fires. Bolts and anchors lose most of their capacity at 300-400°C.
Wang et al. (2020)	Impact of cooling after high-speed heating of granite.	A cooling induced fracture zone (CIFZ) was formed on the specimens. Later, the CIFZ shrunk, leading to closure of cracks, increasing the UCS and compaction of the rock.
Kim et al. (2014)	Exposed different rock specimens to high temperatures followed by rapid cooling.	An increase in crack density was observed in granite, diabase, and KVS (cretaceous volcanic sediments). A decrease in crack density and increase in tensile strength were observed in quartzite, skarn, and other diabase rock.

Table 2.1. (continued)

Lu et al. (2024)	AI- based parametric study on the post-fire behavior of a shield tunnel.	Spalling occurs at low temperatures (below 200°C) and reduces residual strength by 36%. Concrete and bolt deterioration occurs at high temperatures (above 200°C) and reduces strength by 28% and 20%, respectively.
Erdakov and Khokhryachkin (2005)	The impact of fire on the stability of tunnels was studied.	Above 600°C, stiffness of concrete liner decreases by 50%, followed by a breakdown at 800-900°C, and melting by 1200°C.
Jha et al. (1998)	Studied the effects of high temperature on concrete.	Young's modulus of steel reinforcements decreases by 50% at 640°C and fully by 850°C. Full plastic behavior is observed at 1100-1200°C.
Lahouar et al. (2018)	Performed a validation test on post-installed rebars in a concrete slab by subjecting them to fire.	The rebars had a thermal gradient along their length (135 mm), with a change of 55% in temperature along the length.
Hansen (2019)	Observed the behavior of tunnel fire with changing factors.	The behavior of fire depends on the source of fire, combustible materials present in the underground space, and the ventilation system.

Table 2.1. (continued)

Fernández-Alaiz et al. (2020)	Mine fire models and numerical simulations under different ventilation conditions.	The temperature-time curve presents a rapidly increasing temperature at early stage of fire to a peak value, followed by stabilization at the peak and then a slow decay.
Lowndes et al. (2006)	The spread of fire was modelled in underground mine tunnels.	The temperature during a mine fire is higher at the source and near the floor and decreases as it reaches the roof of excavation.
Hansen (2013, 2010)	Investigated the causes and behavior of fire based on fire cases between 1988-2010.	Vehicle fire is the most common. This is generally caused by electrical sources, flammable liquids, and flammable solids ignited by hot surfaces.
Hansen (2017)	Performed fire experiments on diesel and electric-powered vehicles to observe fire behavior in underground hard rock mines.	The fire lasts at a minimum of 200 minutes. It can reach 1000°C within the first 100 minutes.
Larsson (2006)	Reviewed studies regarding the behavior of tunnel fires and their effects on the rock mass.	Duration of previous tunnel fires: Channel tunnel: 7 hours, Mont Blanc tunnel: 53 hours, Tauern tunnel: 17 hours, and St. Gotthard tunnel: 36 hours.
Abraham and Dérobert (2003)	Performed a case study using non-destructive testing of tunnel walls after a fire.	The temperature in the tunnel reached up to 1200°C.

A comprehensive review of the literature reveals that the relationship between the geomechanical properties of the surrounding rock mass and thermo-mechanical coupled damage effects caused by mine fires in underground spaces is poorly understood. More emphasis has been given to the impact on support elements, ventilation systems, rescue plans, and smoke spread during a mine fire. In addition, TM-coupled simulations are limited by temperature range as well as rock types. Therefore, this work presents experimental and computational analyses on hard rocks to reveal the thermomechanical impacts during and after a fire. Strength and deformability tests on andesite samples provided an understanding of the evolution of mechanical parameters when they are exposed to different thermal treatment conditions. In the following stage, the fire-induced thermal damage in a typical underground mine ramp was investigated with parametric models. The geomechanical characteristics of the surrounding rock mass were determined to represent three different rock mass quality conditions in hard rock mines. Thermo-coupled finite element models were computed to simulate the fire-induced damage zones (FIDZ) and stress field at various temperature levels. The study outcomes provide useful insights for the effective management of fires in underground spaces.

2.1 Implementation of Thermo-Coupled Modelling in RS2

RS2 is a rock science finite element code equipped to solve small strain problems in models due to the accumulation of stress under different boundary conditions. The transient heat conduction model allows the calculation of thermal stress based on the temperature exposure in the model at each stage. This procedure is governed by equation 1:

$$[C] * \frac{\partial T}{\partial t} + [K]\{T\} = \{\mathrm{f}\} \qquad 1$$

Where [C] is the heat capacity matrix, T is the temperature, t is the time, [K] is the global stiffness matrix, {T} is the temperature distribution vector, and {f} is the force vector representing the heat flux boundary conditions.

For computing the coupled thermal and mechanical effects, RS2 first computes the mechanical and then the thermal boundary conditions for each stage. The thermal computation is analyzed by finding thermal stress based on incremental thermal strains according to the following relations:

$$\Delta\sigma_{ij} = D^e * \Delta\varepsilon_{ij} \quad 2$$

$$\Delta\varepsilon_{ii}^T = \alpha_T * \Delta T \quad 3$$

Where $\Delta\sigma_{ij}$ is the incremental stress tensor, D^e is the elastic constitutive tensor, $\Delta\varepsilon_{ij}$ is the incremental strain tensor, $\Delta\varepsilon^T$ is the thermal strain, α_T is the coefficient of linear thermal expansion, and ΔT is the change in temperature between successive stages. Furthermore, equation 4 is used to compute the coupled effects of mechanical and thermal stresses.

$$\Delta\sigma_{ij} = D^e\left(\Delta\varepsilon_{ij} - \Delta\varepsilon_{ii}^T\right) \quad 4$$

This allows RS2 to compute the accumulated stresses across successive stages in the model.

2.2 Prediction of Geomechanical Parameters

The geomechanical parameters used for different rock mass quality classes were obtained from a literature survey. These parameters were calculated based on relevant empirical and theoretical formulas. Equations for uniaxial compressive strength (UCS), Young's modulus (E), internal friction angle (ϕ), cohesion (c), and tensile strength (t) are available in previousely published works since the early development of rock mechanics. Relevant formulas for the uniaxial compressive

strength, elastic modulus, internal friction angle, and Poisson's ratio with their sources are given in Tables 2.2 to 2.5.

Table 2.2. Empirical formulas for the uniaxial compressive strength (UCS) of rock mass.

Empirical Formulas	Sources
$UCS_{RM} = UCS_i * \frac{RMR}{RMR + \beta(100 - RMR)}, where\ \beta = 6$	Aydan and Dalgic (1998)
$UCS_{RM} = UCS_i * EXP\left(\frac{7.65 * (RMR - 100)}{100}\right)$	Yudhbir et al. (1983)
$UCS_{RM} = UCS_i * EXP\left(\frac{RMR - 100}{18.75}\right)$	Ramamurthy (1986)
$UCS_{RM} = UCS_i * EXP\left(\frac{RMR - 100}{24}\right)$	Kalamaris and Bieniawski (1995)
$UCS_{RM} = UCS_i * EXP\left(\frac{RMR - 100}{20}\right)$	Sheorey (1997)
$UCS_{RM} = 0.5 * EXP\ (0.06 * RMR)$	Trueman (1998)

Table 2.3. Empirical formulas for Young's modulus (E) of rock mass.

Empirical Formulas	Sources
$E_{RM} = 25 * log(Q), for\ Q > 1$	Barton et al. (1980)
$E_{RM} = 2 * RMR - 100, for\ RMR > 50$	Bieniawski (1978a)
$E_{RM} = 10^{\frac{RMR-10}{40}}, for\ RMR \leq 50$	Serafim and Pereira (1983)
$E_{RM} = 0.1 * \left(\frac{RMR}{10}\right)^3$	Read et al. (1999)
$E_{RM} = 10 * \left(\frac{Q * UCS_{RM}}{100}\right)^{\frac{1}{3}}$	Barton (2002)

Table 2.4. Empirical formulas for the internal friction angle (ϕ) of rock mass.

Empirical Formulas	Sources
$\phi_{RM} = 20 * (UCS_{RM})^{0.25}$	Aydan et al. (1993)
$\phi_{RM} = 20 + 0.5 * RMR$	Aydan and Kawamoto (2001)
$\phi_{RM} = \tan^{-1}\left(\frac{J_r}{J_a} * \frac{J_w}{1}\right)$	Barton (2002)

Table 2.5. Empirical formulas for poisson's ratio (ν) for rock mass.

Empirical Formulas	Sources
$\nu_{RM} = 0.25\,[1 + e^{-0.25 * UCS_{RM}}]$	Aydan et al. (1993)
$\nu_{RM} = 0.5 - 0.2 * \frac{RMR}{RMR + 0.2 * (100 - RMR)}$	Tokashiki and Aydan (2010a)
$\nu_{RM} = 0.5 - \frac{1.8\ln(Q) + 8.8}{7.2\ln(Q) + 55.2}$	Narimani et al. (2023)

CHAPTER 3

PARAMETRIC ANALYSIS OF A HYPOTHETICAL MINE FIRE

Figure 3.1 shows the 2D plane strain models that were created to simulate the fire-induced damage in underground hard rock mines. Parametric models cover three different geomechanical characteristics, two different scales of mine fires, and two different support configurations. Small-scale and large-scale fire simulations were implemented in RS2 and computed with the finite element method. In a small-scale fire model, the thermal source was located in a single level of the ramp. On the other hand, the thermal source was located in two successive levels in a large-scale fire model. Two different support configurations were tested to reveal their effect on the damage zone. While the 'light support' complies with the suggestions of the Q-tunneling index system for the related rock mass quality classes and the opening dimensions, in 'heavy support' the configuration was improved by closely spaced systematic bolts covering the whole excavation boundaries on the walls and the roof.

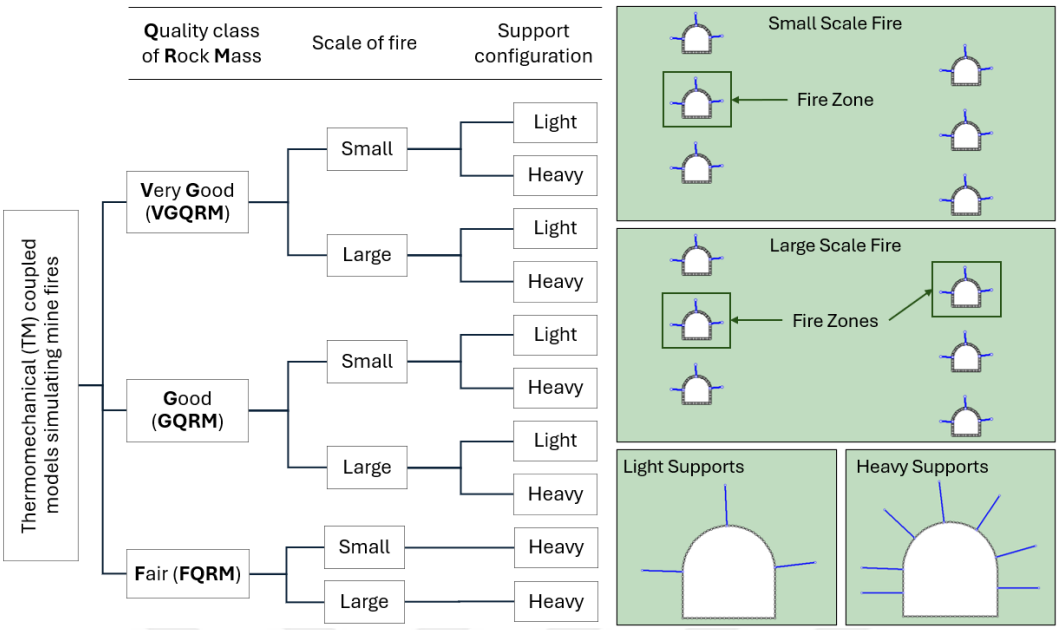

Figure 3.1. Parametric models of mine fire simulations.

3.1 Determination of Domains and Mechanical Properties

The initial phase of the numerical investigation involved determining the geomechanical parameters for different rock mass quality classes that are common in hard rocks. Three domains were defined to later associate with elastoplastic material parameters in the models, representing very good (VGQRM), good (GQRM), and fair quality rock masses (FQRM). Regarding the suggestions by NGI (2015) and Somodi et al. (2022) and consistent with the structural and geological guidelines outlined in the Rock Mass Rating (RMR) system, the quality score of VGQRM ranges between 81 and 100, while GQRM is between 61 and 80 and FQRM is between 41 and 60.

3.1.1 Geomechanical Properties Before Thermal Effects

The mechanical inputs for rock mass were determined by comprehensively interpreting the literature involving field studies complemented with laboratory-scale mechanical tests, in-situ mechanical tests, empirical expressions, and expert opinion. This section presents an overview for each individual parameter.

The uniaxial compressive strength (UCS) of intact rock (σ_c) was determined from mean values suggested by Hoek and Brown (1997) for each domain. Several expressions have been suggested in the literature for finding UCS for rock mass (σ_{cm}). However, Equation 5, recommended by Aydan and Dalgic (1998), outweighed the alternatives by making use of the RMR score to make relevant predictions for the σ_{cm}/σ_c range suggested by Dinc et al. (2011).

$$\sigma_{cm} = \sigma_c * \left[\frac{RMR}{RMR + 600 - 6RMR}\right] \quad 5$$

The rock mass elastic modulus (E) was calculated using Equation 6 (Barton, 2002), which was suggested for tunnels exhibiting an intact rock uniaxial compressive strength range of 10-200 MPa and a Q-index range of 0.1-100 (Singh and Goel, 2011). Literature research and expert opinion approved the validity of this expression to estimate a well-suited value for the elastic modulus for the given domain features.

$$E_m = 10 * \left(Q * \frac{\sigma_c}{100}\right)^{\frac{1}{3}} \quad 6$$

Poisson's ratio (ν_m) for the rock mass was found using Equation 7 as suggested by Tokashiki and Aydan (2010).

$$\nu_m = 0.25 * [1 + e^{-0.25*\sigma_{rm}}] \quad 7$$

Using the UCS of rock mass, cohesion was calculated from Equation 8 as recommended by Barton and Pandey (2011).

$$c_m = \frac{RQD}{Jn} * \frac{1}{SRF} * \frac{\sigma_{cm}}{100} \quad (8)$$

The internal friction angle ϕ_m for the rock mass was calculated using Equation 9 as recommended by Tokashiki and Aydan (2010). Other available expressions for ϕ_m made calculations out of the range that were suggested by Bieniawski (1978).

$$\phi_m = 20 * \sigma_m^{0.25} \quad (9)$$

By using the values found for cohesion and internal friction angle, the tensile strength of the rock mass, σ_t was calculated from Equation 10 (Ranasooriya, 2009). Alternative expressions available in literature for tensile strength depend on other rock mass variables and are considered irrelevant to this work.

$$\sigma_t = \frac{2 * c * cos\phi}{1 + sin\phi} \quad (10)$$

In calculating the model parameters, the following assumptions were made: (1) the rock mass is homogenous, (2) the materials are linear elastic–perfectly plastic, and (3) the failure is governed by the Mohr-Coulomb criterion. Table 3.1 shows the mechanical parameters used in the model in comparison to values found in literature.

Table 3.1. The mechanical parameters assigned to the model domains.

Rock Mass Quality Class	VGQRM			GQRM			FQRM		
Rock Mass Rating Interval, RMR	81-100			61-80			41-60		
Mechanical Properties	Literature		Calculated	Literature		Calculated	Literature		Calculated
	Empirical Prediction	In-situ Test		Empirical Prediction	In-situ Test		Empirical Prediction	In-situ Test	
Elastic Modulus (GPa)	[**42**] (Hoek and Brown, 1997). [**40**] (Barton, 2002). [**21.7, 25.3**] (Cai et al., 2004). [**21.8, 46.4**] (Alemdag et al., 2015)	[**29.4, 36.6**] (Plate Load Test) (Cai et al., 2004). [**20, 80**] (Back Analysis, and Flat Jack) (Hoek and Diederichs, 2006)	39.8	[**9.0**] (Hoek and Brown, 1997). [**25**] (Barton, 2002). [**10.1, 19.6**] (Cai et al., 2004). [**10.7, 27.3**] (Alemdag et al., 2015)	[6.7, 15.7] (Plate Load Tests) (Cai et al., 2004). [1, 40] (Back Analysis, Flat Jack, and Plate Tests) (Hoek and Diederichs, 2006)	15.1	[**13**] (Jalote et al., 1996). [**15**] (Barton, 2002). [**12.6**] (El-Naqa and Al Kuisi, 2002). [**7.7, 9.7**] (Cai et al., 2004). [**3.6, 7.8**] (Alemdag et al., 2015)	[**10.0, 13.4**] (Plate Load Tests) (Cai et al., 2004). [**0.9, 11.7**] (Back Analysis, Flat Jack) (Hoek and Diederichs, 2006)	7.0
Poisson's Ratio	[**0.25, 0.27**] (Narimani et al., 2023)	-	0.25	[**0.25, 0.27**] (Narimani et al., 2023)	-	0.25	[**0.26, 0.27**] (Narimani et al., 2023). [**0.28**] (Cai et al., 2022). [**0.34**] (Yertutanol et al., 2020)	-	0.29

Table 3.1. (continued) The mechanical parameters assigned to the model domains.

Uniaxial Compressive Strength (MPa)	[**64.8**] (Hoek and Brown, 1997). [**43.8, 105.0**] (Dinc et al., 2011)	-	79.6	[**13**] (Hoek and Brown, 1997). [**15.0, 43.5**] (Dinc et al., 2011)	-	20.6	[**8.2**] (Jalote et al., 1996). [**4**] (El-Naqa and Al Kuisi, 2002). [**4.5, 18.0**] (Dinc et al., 2011)	-	7.1
Tensile Strength (MPa)	[**0.9**] (Hoek and Brown, 1997). [**10.3, 13.5**] (Cai, 2009)	-	12.9	[**0.15**] (Hoek and Brown, 1997). [**4.1, 4.8**] (Cai, 2009)	-	1.5	[**0.14**] (Jalote et al., 1996)	-	0.5
Cohesion (MPa)	[**13**] (Hoek and Brown, 1997). [**3.1, 4.3**] (Cai et al., 2004). [**35, intact**] (Köken et al., 2024)	-	23.9	[**3.5**] (Hoek and Brown, 1997). [**1.1, 2.9**] (Cai et al., 2004)	[**0.8, 1.5**] (Block shear test) (Cai et al., 2004)	1.8	[**2.0**] (Jalote et al., 1996). [**1.04, 1.24**] (Cai et al., 2004). [**0.97**] (El-Naqa and Al Kuisi, 2002). [**0.25**] (Yertutanol et al., 2020)	[**1.9**] (Block shear test) (Cai et al., 2004)	0.5
Internal Friction Angle (°)	**[46]** (Hoek and Brown, 1997) [**56, 59**] (Cai et al., 2004)	[**57**] (Block shear test) (Cai et al., 2004)	60	[**33**] (Hoek and Brown, 1997) [**49.6, 57.3**] (Cai et al., 2004)	[**55, 58**] (Block shear test) (Cai et al., 2004)	43	**[40.0]** (Jalote et al., 1996). [**38.5**] (El-Naqa and Al Kuisi, 2002). [**40.4, 43.4**] (Cai et al., 2004) [**30**] (Yertutanol et al., 2020) [**35**] (Cai et al., 2022)	**[40]** (Block shear test) (Cai et al., 2004)	33

To validate the proposed hard rock domains, estimations were compared to the literature associating rock mass geomechanical properties with the rock mass quality classifications. The comparison was done in terms of the empirical predictions and in-situ tests. For example, Bhasin et al. (1996) compared measured and predicted geotechnical data of an underground cavern in the Himalayas. For rocks similar to FQRM, the elastic modulus was calculated as 10.78 GPa (7.0 GPa in our study), and the intact UCS was found to be 20-50 MPa, closely aligned to the range we determined as 25-50 MPa. In another study in Taiwan and China, the elastic modulus for FQRM was found to be 0.9-11 GPa, for GQRM it is 1-40 GPa, and for VGQRM it is under 20-80 GPa, aligning well with our calculated values (Hoek and Diederichs, 2006). For a rock mass with properties equivalent to VGQRM, Cai et al. (2004) found elastic modulus to be between 7.9 and 45.3 GPa, cohesion as 0.8-5.2 MPa, and internal friction angle as 55-58° from in-situ tests. Similarly, for FQRM, the elastic modulus, cohesion, and internal friction angle were found to be 11.7 GPa, 1.9 MPa, and 40°, respectively. To conclude, our estimations for geomechanical properties of the three proposed domains are relevant to the literature.

3.1.2 Geomechanical Properties After Thermal Damage

An experimental program was designed to understand the post-fire effects on the geomechanical properties of hard rocks. In this scope, core andesite specimens were exposed to twelve temperature levels between 50°C and 1000°C for short and long terms, and their strength parameters were measured afterwards. Short-term treatment was completed in 1 day, whereas for long-term treatment, it was 7 and 14 days. The cylindrical specimens were prepared with a diameter of 54 mm and a length/diameter ratio of 2.5:1 in accordance with the methods suggested by the International Society of Rock Mechanics (ISRM). Intact core samples were preconditioned to the target temperature and then left to cool down at room temperature. Later, they were exposed to static deformability tests, triaxial

compression tests, and indirect tensile strength tests to quantify their elastic and plastic properties.

For the static deformability test, core samples were conditioned at said temperatures for short and long terms. In the preparation for the triaxial compression test, all specimens were preconditioned for 14 days and exposed to different confining pressures of 5 MPa, 10 MPa, and 15 MPa after cooling down. The specimens for the indirect tensile strength test were also preconditioned for 14 days only. For temperature levels of 50°C to 200°C, the temperature was kept for the entire duration, whereas for temperatures higher than 200°C, the specimens were exposed to target temperatures for the final 4 hours only, while being kept at 200°C for the duration before that. All mechanical tests were performed with the help of a servo-controlled 2800 kN MTS 815 stiff testing frame, and the data was recorded by an external data acquisition system, TDG test box 1001. Specimens were loaded until the failure point with a displacement rate of 0.002 mm/s. To measure the deformations, axial and lateral extensometers were attached to samples in uniaxial loading, and strain gauges were used in the triaxial compression tests. The experimental setup and a deformed specimen for each test type are provided in Figure 3.2 (a-c). The stress-strain curves for uniaxial and triaxial tests were used to calculate the remaining parameters. These graphs are shown in Figure 3.3 for room temperature cases. The stress-strain graphs for the remaining temperature levels are provided in Appendix A and B.

For the post-fire condition, the short-term exposure to increasing temperatures is relevant to understanding the behavior of hard rocks right after the fire and before the fire is extinguished. Hence, the focal point will be the results of the short-term static deformability test. It can be observed that uniaxial compressive strength (UCS) first increases sharply from room temperature (RT) to 100°C by 49%, after which it decreases and then increases again at 400°C by 45% more than RT. Following 400°C, it decreases with an increasing temperature, falling below RT at 1000°C. The general trend shows an increase from RT to 400°C, after which it drops to RT value at 600°C and below RT value afterwards. The elastic modulus was

observed to decrease sharply from RT to 150°C by 13%, rising again at 200°C and decreasing afterwards. It reaches below the RT value at 1000°C. The general trend shows an increase in value from RT to 400°C, followed by a decrease to RT value after 600°C and below RT at 800°C. The values of Poisson's ratio range between 0.15 and 0.25, generally increasing with increasing temperature. During the experiments, only one sample was exposed to 1100°C for 4 hours, and it displayed a molten texture when taken out of the oven, after which it cooled down to room temperature in a deformed state, as shown in Figure 3.2 (d-e). Data representing the change in UCS and elastic modulus with increasing temperature for short and long terms is given in Figure 3.4.

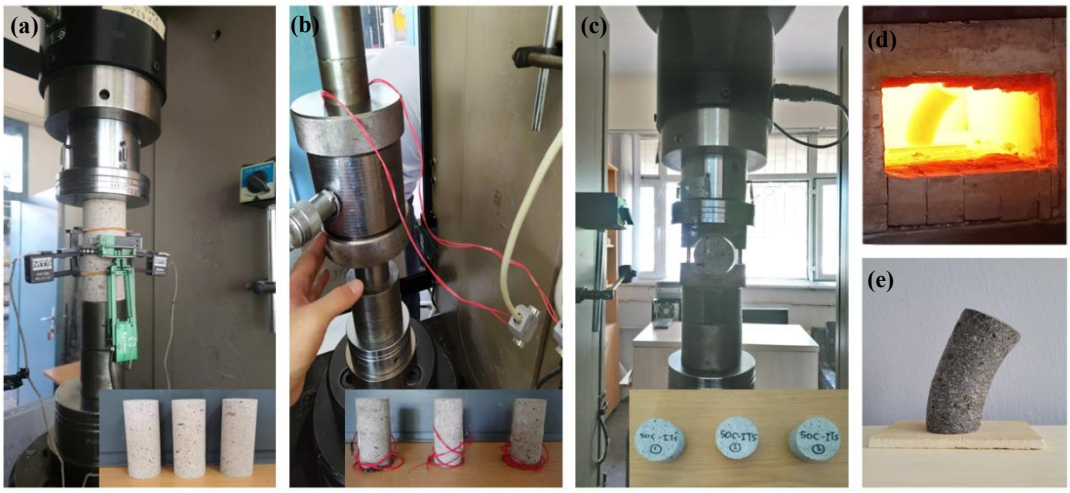

Figure 3.2. Experimental setups for (a) Static deformability test, (b) Triaxial compression test, (c) Indirect tensile strength test, and (d) molten specimen after pre-treatment of 1100°C.

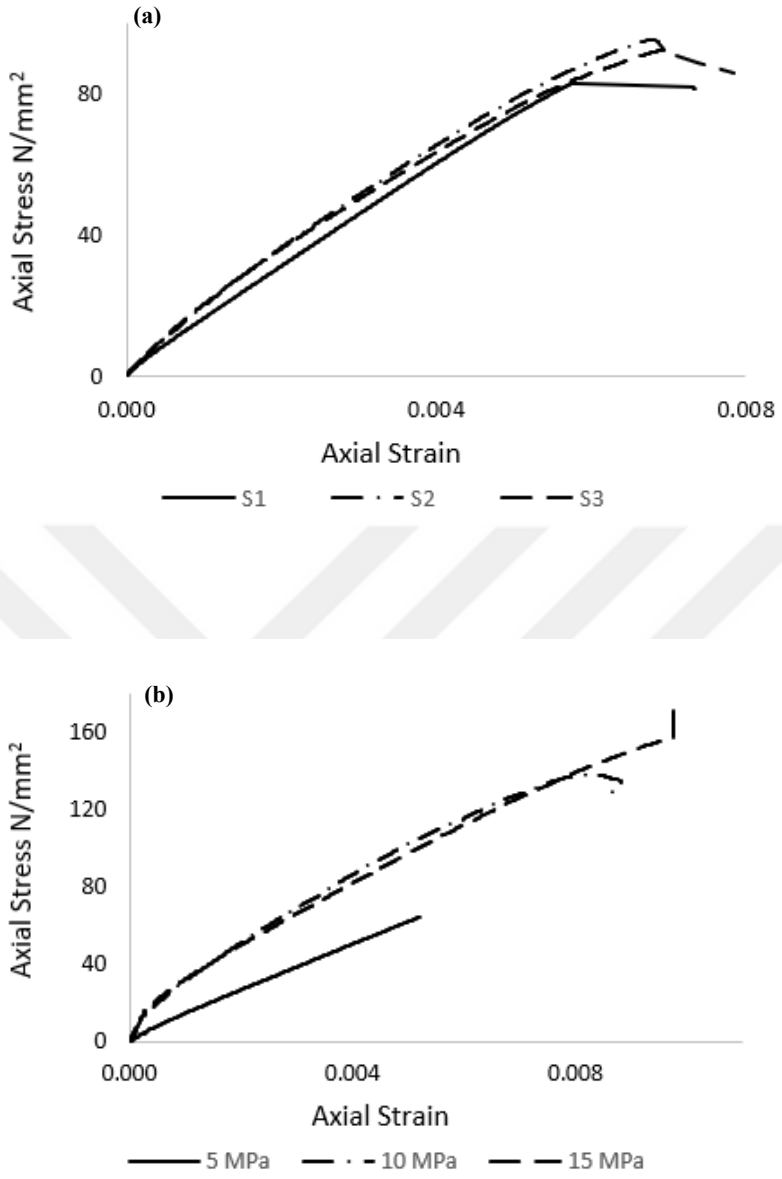

Figure 3.3. Trend of axial stress vs axial strain in (a) Static deformability test for three specimens, and (b) Triaxial compression test at different lateral compression values at room temperature.

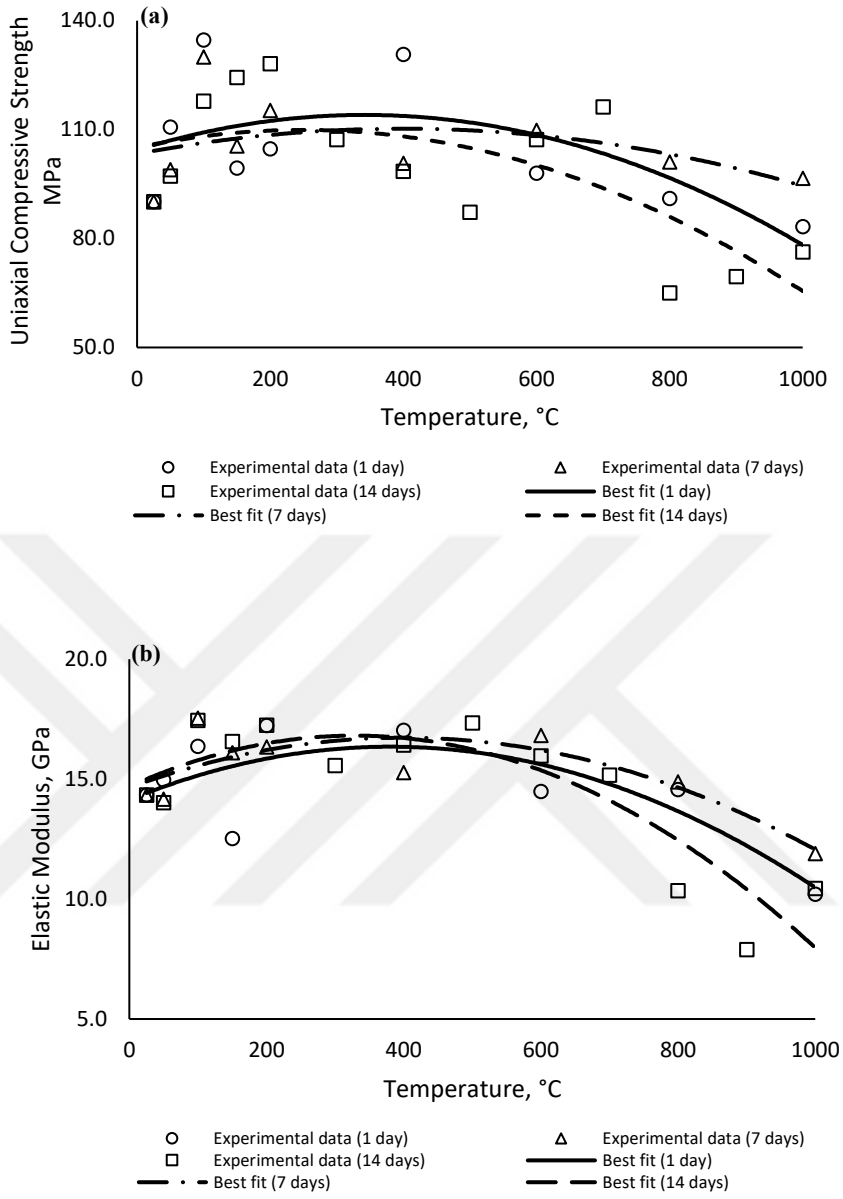

Figure 3.4. Trend of (a) uniaxial compressive strength and (b) elastic modulus in samples treated with different temperature levels for 1, 7, and 14 days.

The changes in plastic properties observed in the long-term exposure of Ankara Andesite are shown in Figures 3.5 and 3.6. With the help of triaxial compression tests, the effects of temperature on the cohesion and internal friction angle were observed. The value of cohesion increases with the increasing temperature. The internal friction angle first increases from RT to 400°C and

decreases afterwards. It reaches a value less than RT as the temperature gets closer to 1000°C. Comparing the values under different confinement pressures, UCS and elastic modulus are higher when the confinement pressures are high, especially between 200°C and 800°C. The values for Poisson's ratio from the triaxial compression tests are higher than those found in static deformability tests, ranging between 0.21 and 0.47 instead of 0.15 and 0.25, as can be seen in Figure 3.7. For a pressure of 5 MPa, the value decreases from RT to 600°C and then increases afterwards. A similar trend can be seen in the cases of 10 MPa and 15 MPa, where they decrease until 400°C and 200°C, respectively, and increase afterwards. Comparing the values of Poisson's ratio in the first experiment for specimens conditioned for 14 days to the ones in the triaxial compression test, the presence of pressure on the lateral sides of the specimen increases the values of UCS, elastic modulus, as well as Poisson's ratio.

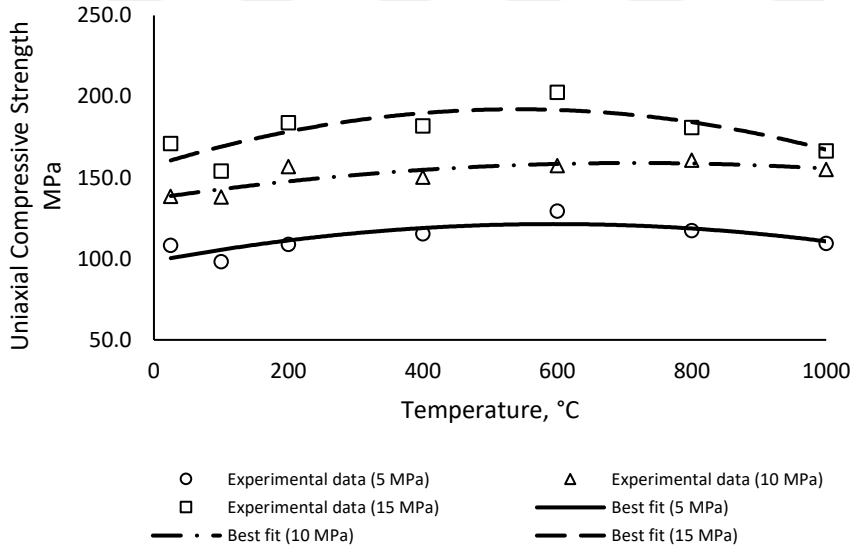

Figure 3.5. Trend of confined compressive strength in samples treated with different temperature levels for long term tests (14 days).

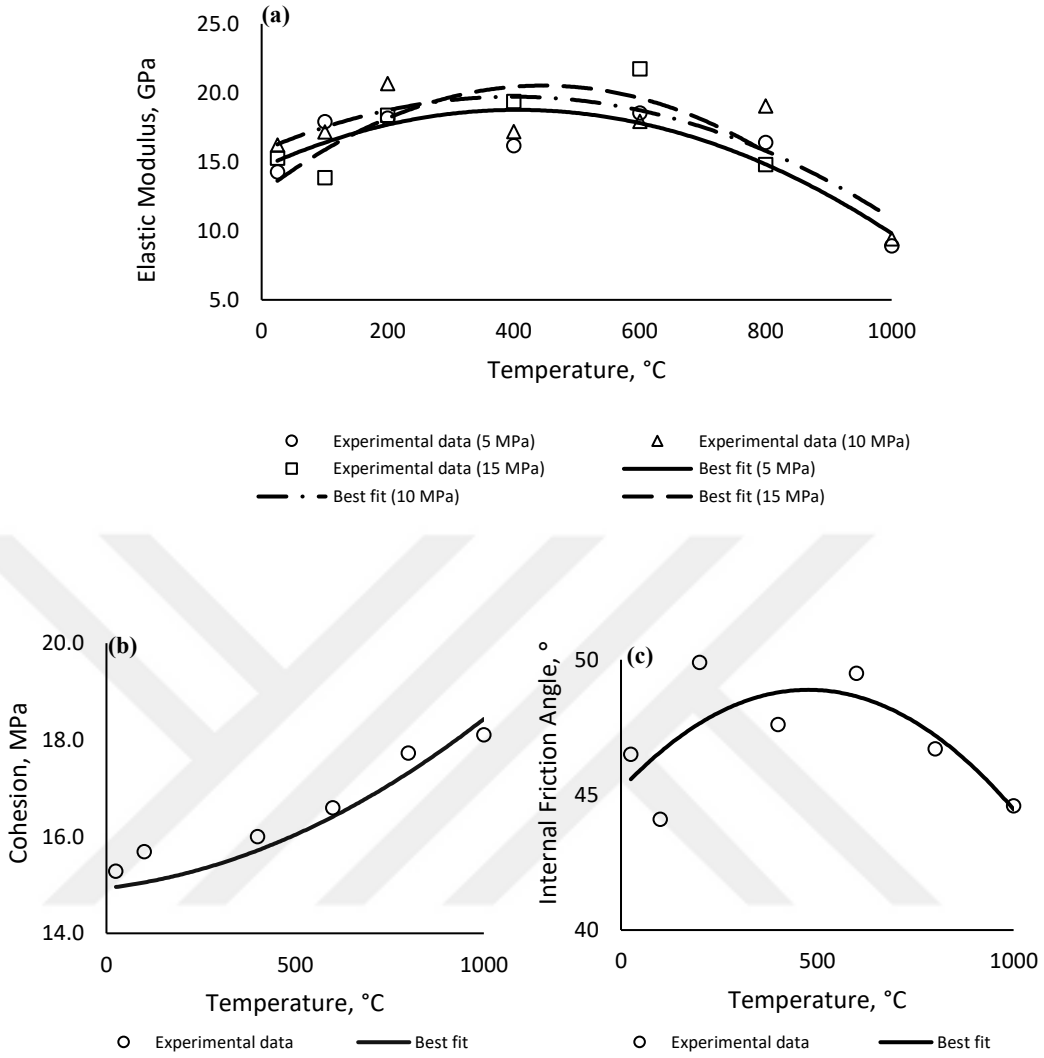

Figure 3.6. Trend of (a) confined elastic modulus, (b) cohesion, and (c) internal friction angle in samples treated with different temperature levels for long term tests (14 days).

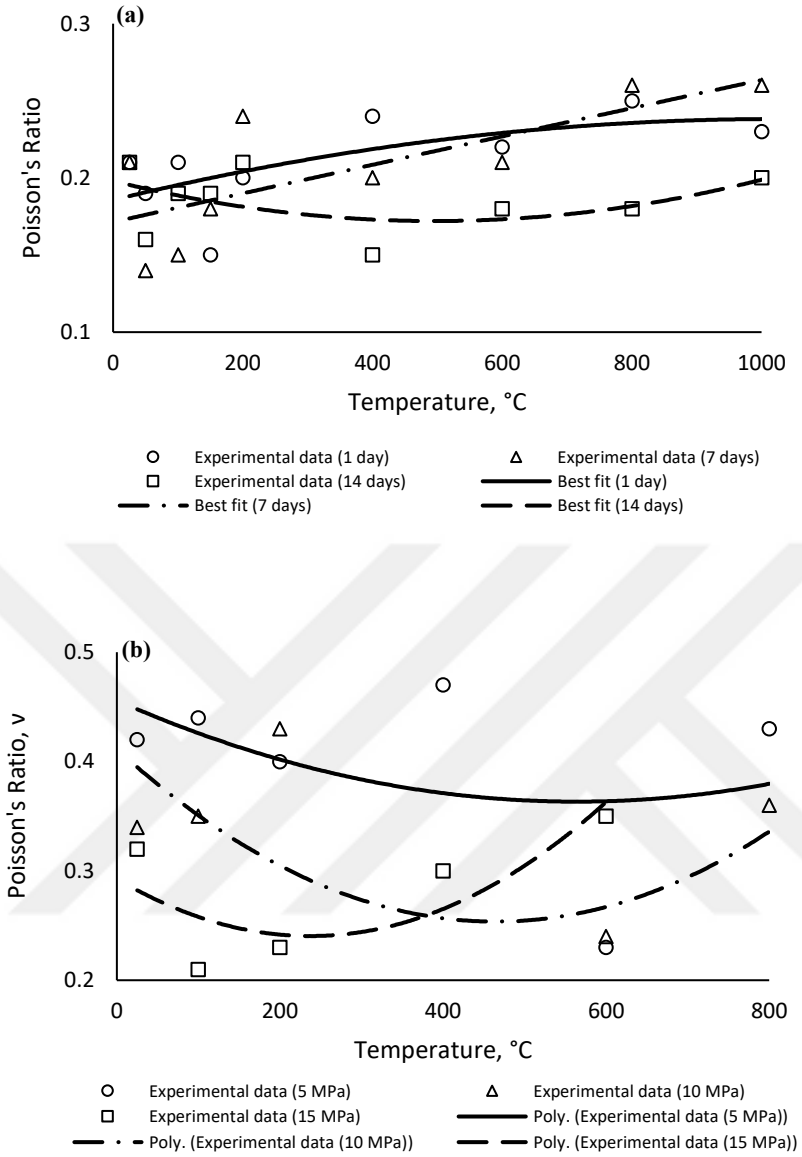

Figure 3.7. Trend of Poisson's ratio according to (a) static deformability tests (treated for 1, 7, and 14 days), and (b) triaxial compression tests (treated for 14 days).

In Brazilian tests measuring the indirect tensile strength, the tensile strength peaked at 200°C, after which it decreased to below RT value by 400°C and dropped sharply afterwards, decreasing by 65% of RT value. The trend for tensile strength is illustrated in Figure 3.8.

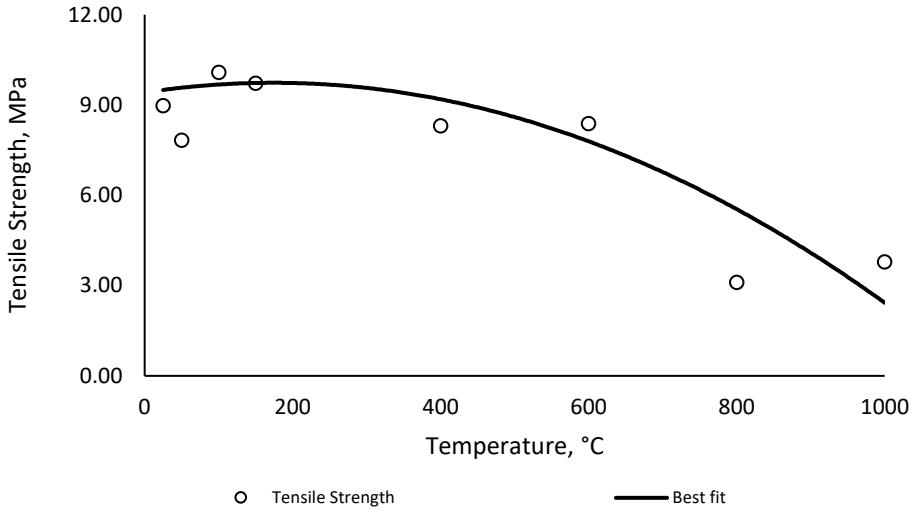

Figure 3.8. Trend of tensile strength in samples treated for 14 days.

3.2 Support Configurations for the Specified Rock Mass Quality Classes

Haul roads in underground mining are considered permanent openings and instrumented with support configurations to keep long-term stability. Therefore, the fire-induced damage should be considered for supported excavations. To make a suitable support design for the specified rock mass conditions, Q-tunneling index guidelines were used (NGI, 2022). The excavation support ratio was assigned from the permanent mine openings category. For the crown and wall supports, the equivalent dimension and Q index were used. Details on bolt length and bolt spacing for each rock mass quality are given in Table 3.2. The properties of the bolts used in the models are given in Table 3.3.

Table 3.2. Bolt pattern for the specified rock mass quality classes.

Support Properties	Bolt Length (m)		Bolt Spacing (m)	
	Crown	Walls	Crown	Walls
VGQRM	2.2	-	3.8	-
GQRM	2.2	2.2	2.5	3.8
FQRM	2.2	2.2	1.8	2.3

Table 3.3. Mechanical properties of the bolts used.

Bolt Type	Fully Bonded
Bolt Diameter (mm)	26
Bolt Modulus, E (MPa)	50000
Tensile Capacity (MN)	0.35
Out-of-Plane Spacing (m)	1

3.3 Model Geometry and Boundary Conditions

A helical mine ramp in a homogenous andesite rock mass was modeled with a 25 m turning radius and a 12% gradient. A vertical cross-section of the ramp was taken and modeled to observe the effects of small- and large- scale fires. Each opening in the cross-section was a 5m x 5m horseshoe-shaped excavation. Figure 3.9 shows the front view of the ramp in 3D, the model view of the cross-section of the ramp in 2D, and the support configuration around one opening in the case of heavily supported VGQRM.

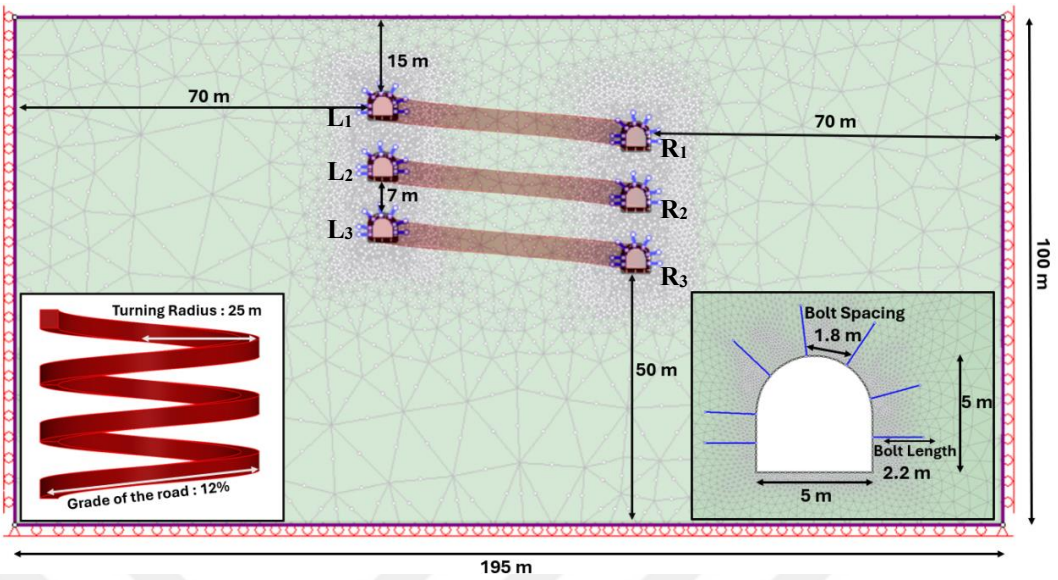

Figure 3.9. Model view of the ramp cross-section in 2D, with clippings of front view (Left) and cross-section of a typical excavation in VGQRM (Right).

The horizontal distance between the excavations and the nearest boundaries is set as 70 m. The top-most and bottom-most distances are taken as 15 m and 50 m, respectively. The far-field stress ratio was set as 1. These exact boundary conditions were used across all the models in the unsupported, supported, and thermal-mechanical coupled cases for all variations.

3.4 Assessment of Fire Induced Damage Zone (FIDZ) with Thermocoupled Models

Taking into account the pattern of the increase in temperature in mine fires, a thermal-mechanical coupled model was created to analyze the gradual effects of fire in the rock mass. The effects were observed for the first stage of fire, i.e., the sudden increase in temperature. The model assessed temperatures starting at room temperature until 400°C at an increment of 20°C, and then up to 1200°C with an increment of 50°C between each stage, as presented in Table 3.4. A transient flow

of temperature was applied according to the temperature-time graph of fuel-controlled mine fires given by Ma and Mäkeläinen (2000), as given in Figure 3.10. To understand the effects of the span of fire on the mechanical parameters of the surrounding rock, the fires were modeled in one excavation and in two consecutive excavations for each case where the increasing temperature was applied to the excavation boundary of the fire-affected zones according to Table 3.4.

Table 3.4. Stages in the model with corresponding temperature, analysis type, and duration.

Stage Number	Analysis Type	Temperature (°C)	Time (s)	Stage Number	Analysis Type	Temperature (°C)	Time (s)
1	Elastic	RT	0	20	Plastic	370	54
2	Plastic	RT	1	21	Plastic	390	57
3	Plastic	RT	3	22	Plastic	400	60
4	Plastic	50	6	23	Plastic	450	75
5	Plastic	70	9	24	Plastic	500	90
6	Plastic	90	12	25	Plastic	550	105
7	Plastic	110	15	26	Plastic	600	120
8	Plastic	130	18	27	Plastic	650	135
9	Plastic	150	21	28	Plastic	700	150
10	Plastic	170	24	29	Plastic	750	165
11	Plastic	190	27	30	Plastic	800	180
12	Plastic	210	30	31	Plastic	850	210
13	Plastic	230	33	32	Plastic	900	240
14	Plastic	250	36	33	Plastic	950	270
15	Plastic	270	39	34	Plastic	1000	300
16	Plastic	290	42	35	Plastic	1050	375
17	Plastic	310	45	36	Plastic	1100	450
18	Plastic	330	48	37	Plastic	1150	525
19	Plastic	350	51	38	Plastic	1200	600

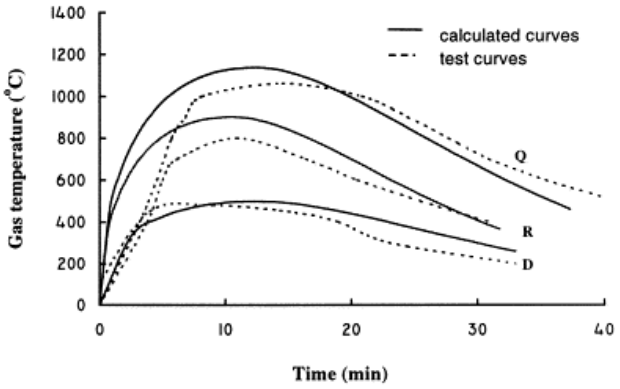

Figure 3.10. Temperature-time curve of fuel-controlled fires (Ma and Makelainen, 2000).

The surface temperature was set at 25°C. The temperature increased from the surface to the base of the model according to a geothermal gradient of 25°C/km, and this was applied to the model boundaries. The value for thermal conductivity for andesite was referenced from a study regarding thermophysical properties of the Tauhara geothermal site in New Zealand (Mielke et al., 2015), and that of the thermal expansion coefficient was taken from a study using Rotokawa andesite (Siratovich et al., 2015). The complete thermal parameters used are given in Table 3.5. Figure 3.11 illustrates the thermal boundaries of the model at 400°C for heavily supported VGQRM.

Table 3.5. Thermal parameters used in the models.

Thermal Conductivity (W/m/C)	0.72
Volumetric Heat Capacity (J/m3/C)	1514
Thermal Expansion Coefficient	1.0E-05

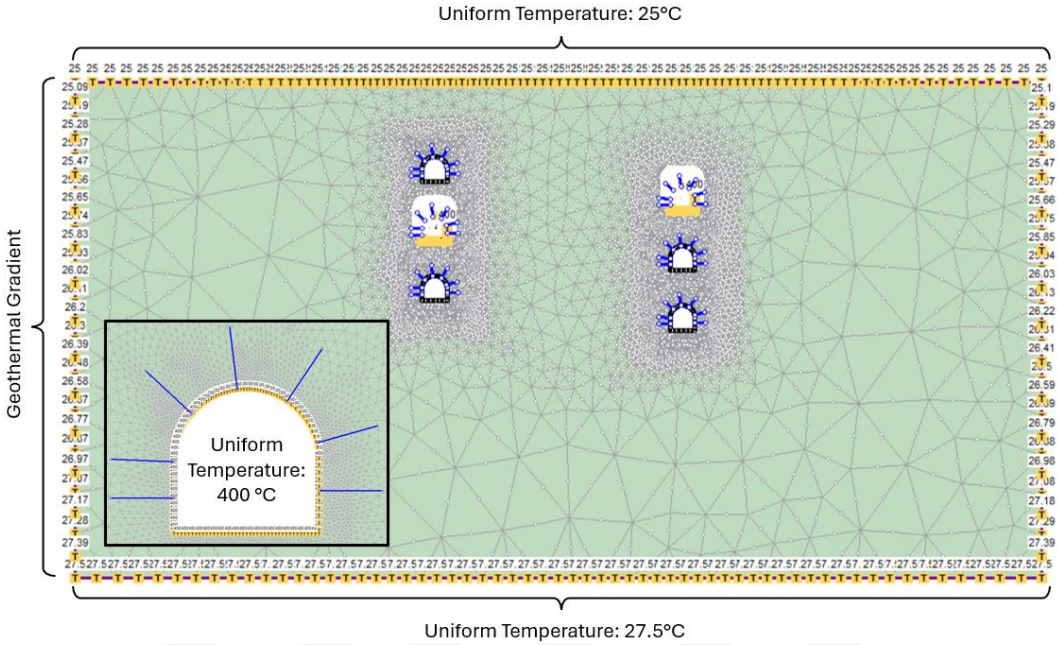

Figure 3.11. Model view of the ramp cross-section showing the thermal boundaries with snippet of thermal boundaries around one of the excavations in VGQRM.

CHAPTER 4

RESULTS AND DISCUSSION

Model results reveal the performance of a typical underground mine haul road excavated in different rock mass quality classes in terms of the excavation-induced deformations and the coupled thermo-mechanical effects of small- and large-scale fires. The following sections provide interpretations for parametric models.

4.1 Mining Induced Stresses Around the Openings

Models for in-situ unexcavated cases as well as excavated cases were compared to observe the effects of excavation on the stability of the ramp. No yielding was observed in VGQRM and GQRM cases. However, stress distribution and deformations were seen to change between the different levels, increasing as we go from the top to the bottom openings due to the weight of the rock mass. In the case of FQRM, yielding was observed on the sharp edges and crown of the openings. The extent increases with increasing depth of excavations, with the maximum span being 32 cm. When supports are applied, a clear change in the yielding pattern was observed, indicating how supports reduce the extent of the damage zone around an excavation. Figure 4.1 illustrates the stress distribution among different levels in the ramp for VGQRM, GQRM, and FQRM.

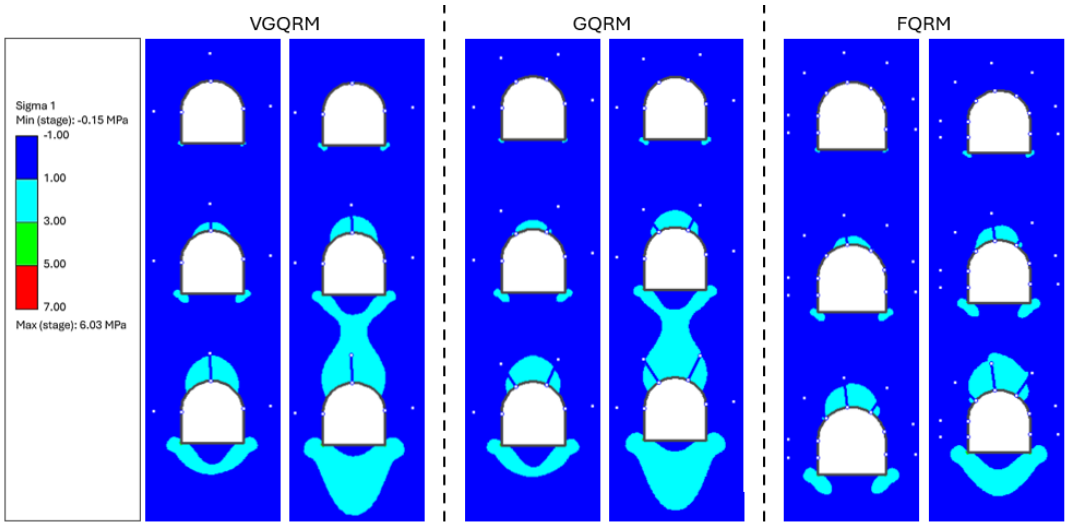

Figure 4.1. The cross-section view showing stress contours around supported excavations of a ramp for VGQRM, GQRM, and FQRM.

4.2 Fire Induced Damage in a Small-Scale Fire

In the case of VGQRM, the fire-induced deformations first localize at 150°C around sharp edges, expanding with increasing temperature. At 600°C, the whole excavation boundary is affected. By this temperature, the compressive stress around the opening increases, creating a fire-induced damage zone (FIDZ). This zone tries to detach from the rest of the rock mass, which creates a localization in terms of a tensile stress ring around it, which in turn spreads the damage zone even farther. A similar FIDZ is also created near the floor of the opening, and both intensify. At 850°C, the roof of the opening below starts to yield, followed by the floor of the above opening at 900°C. The interaction between the two elevations continues, affecting the upper elevation more intensely and merging with the ramp level above at 1050°C. The effect of fire spreads to the far ends of the levels above and below, creating a shear failure zone at 1050°C and 1100°C, respectively. The progression of FIDZ in the recommended as well as the heavier support cases is quite similar. However, in the case of heavier support, the openings above and below initiate

yielding at 900°C instead of 850°C. Additionally, the damage zone above the fire source is more intense in the light support case. This explains that heavier supports in mines prone to fire are a good precaution in controlling the spread of fire. The progression of the thermal damage zone around L2 in the case of VGQRM is shown in Figure 4.2.

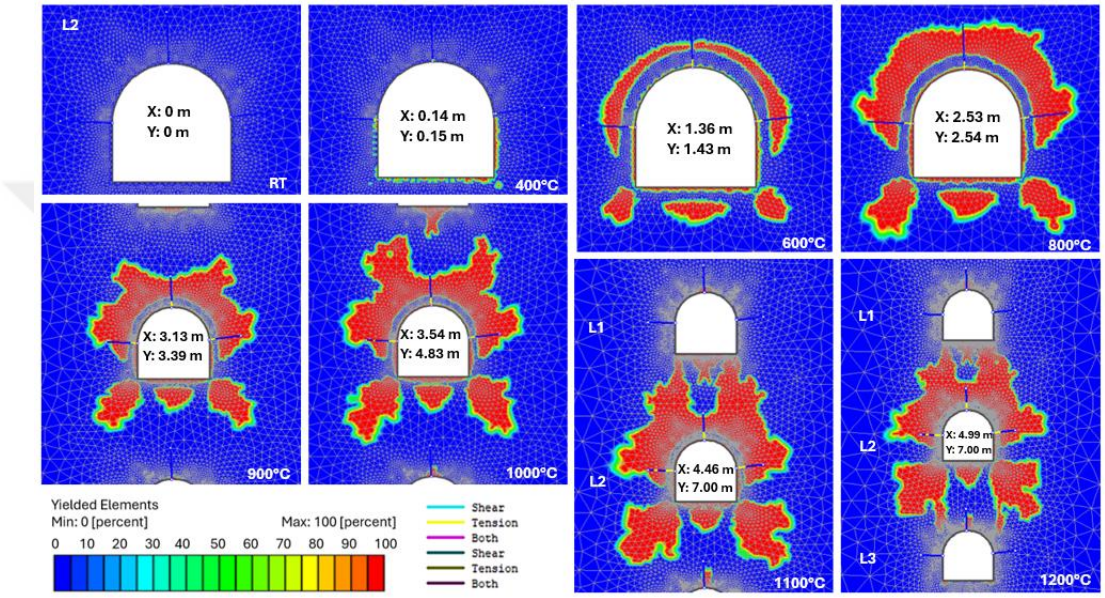

Figure 4.2. The span of the thermal damage zone around L2 in the case of VGQRM (X and Y values represent the maximum horizontal and vertical spans respectively).

The tensile stress exceeds the bolts capacity at 190°C, making them partially ineffective by 600°C and completely failing at 800°C. The displacement contours were observed to concentrate around sharp edges and the region between the fire source and the upper level of the ramp. This is also where the major principal plastic strain concentrates in the model. Overall, the FIDZ is concentrated on the crown and sharp edges, progressing aggressively. Moreover, the progression is more vertical than horizontal due to the presence of excavated levels above and below.

In GQRM, the yielding starts at 70°C, covering the entire boundary by 130°C. The FIDZ is quite uniform around the walls and the crown in this case, with a higher concentration around sharp edges. Between 650 and 850°C, a tensile stress ring starts to form around the excavation, which spreads with increasing temperature, following which the concentration of FIDZ on the crown and sharp edges becomes noticeable. The damage effects initiate on the lower and above excavations due to shear failure at 1050°C. At temperatures higher than 1050°C, more interaction occurs with the upper and lower openings, reaching the boundary of the upper level at 1100°C. In GQRM, the far end of the ramp level above is affected by the fire as well, displaying shear failure at 1200°C. The progression of FIDZ is very similar in the cases of light and heavy supports. The tensile stress rings in the latter form between 700 and 800°C. Detailed illustrations of the development of FIDZ around L2 in the case of GQRM are given in Figure 4.3.

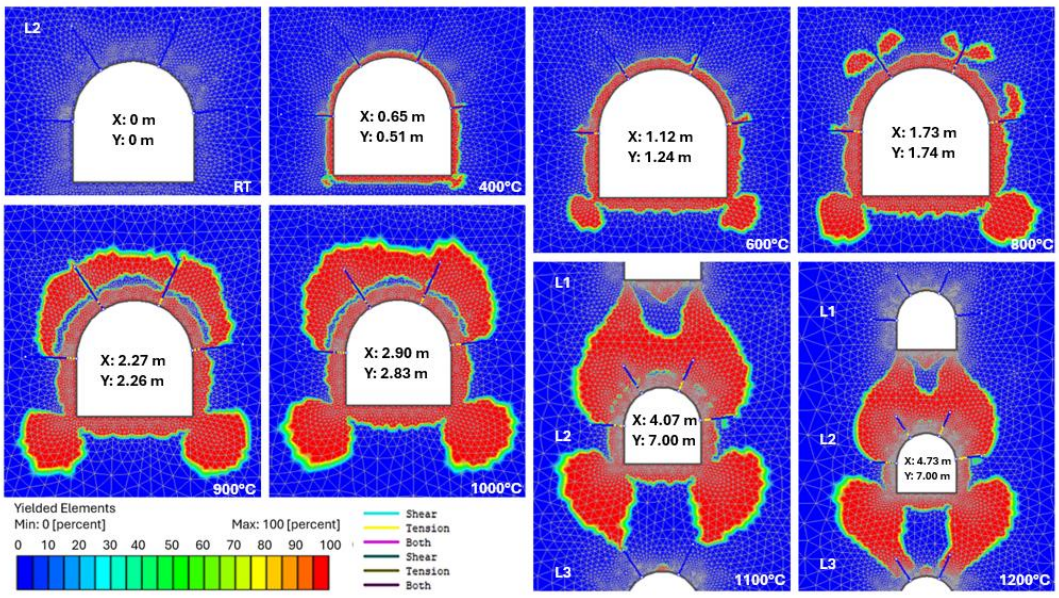

Figure 4.3. The span of the thermal damage zone around L2 in the case of GQRM (X and Y values represent the maximum horizontal and vertical spans respectively).

Bolts in the support system start yielding at 250°C in GQRM, becoming partially inactive by 330°C and then failing completely at 900°C. The total displacement contours in this case, as well as the major principal plastic strains, are concentrated around the excavation boundary. This indicates that the region around the excavation is affected more, followed by the zones leading to the upper and lower excavations. The FIDZ at higher temperatures is concentrated on the entire crown and the sharp edges, with a higher concentration on the walls as compared to VGQRM.

In FQRM, the thermal damage zone appears as soon as the ramp is excavated due to mechanical damage and intensifies as the depth of the excavation increases. In the fire zone, the FIDZ grows uniformly around the excavation with increasing temperature. When temperatures are over 200°C, concentration on the region of bolts can be seen, slowly inactivating them. The bolts start to yield at 230°C and become completely useless by 500°C. This occurs due to the damage zone loosening the bolts, hence reducing the tension between the bolts and the excavation boundary, and the bolts fail to hold up. A high tensile stress ring forms around the excavation near the sharp edges at 850°C and concentrates on the bolts at 1050°C, leading to rock failures. The damage zone affects the floor of the above excavation further at 1200°C. The total displacement as well as the major principal plastic strain are concentrated around the excavation boundary only. The yield zone in FQRM is very uniform around excavation geometry. This progression of the FIDZ around L2 in the case of FQRM is illustrated in Figure 4.4.

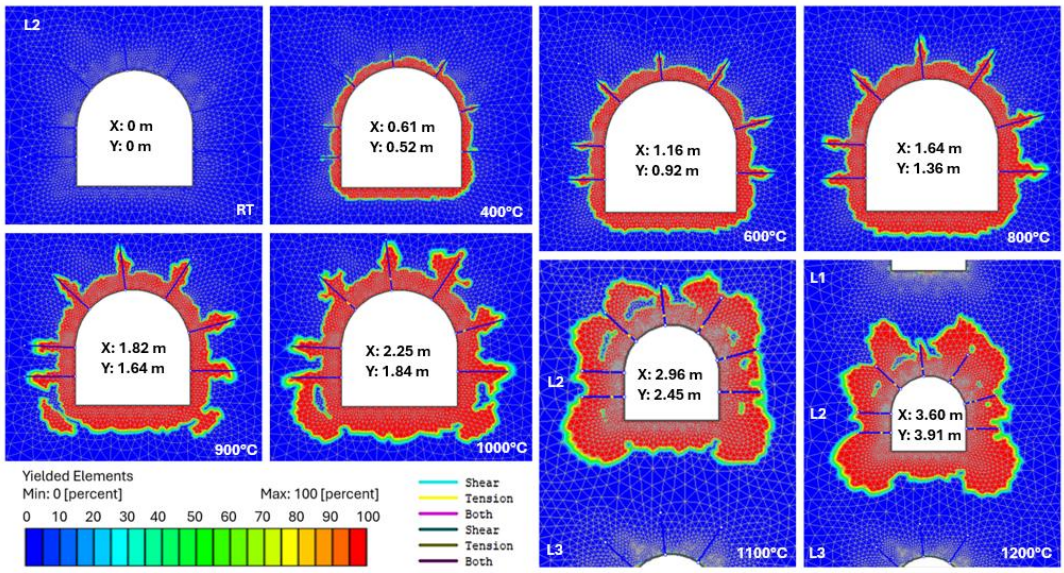

Figure 4.4. The span of the thermal damage zone in FQRM (X and Y values represent the maximum horizontal and vertical spans respectively).

The coupled damage zone in the case of VGQRM is spread more vertically, creating roof problems, merging with the opening above, and progressing sharply. This is due to the deformations expanding more easily in brittle rock mass as compared to low-quality classes, where it concentrates around the affected zone. The one in GQRM progresses softly and interacts with the levels above and below much later, after 1000°C and clearly more than the VGQRM. In GQRM, roof as well as slight wall problems can be observed. The failure shown by this rock mass is a mixture of tensile and shear failures. In the case of FQRM, the damage zone is very uniform around the excavation boundary and affects the entire boundary at an equal amount. In all cases, the sharp edges are affected due to mechanical as well as thermal loading, indicating that round edges withstand more stress and less concentrations; hence, avoiding sharp edges makes it safer for long-term uses of underground excavations. The progression of the major principal stress in all three cases is shown in Figure 4.5. Contours for the total displacements around the fire-affected zones are given in Appendix C.

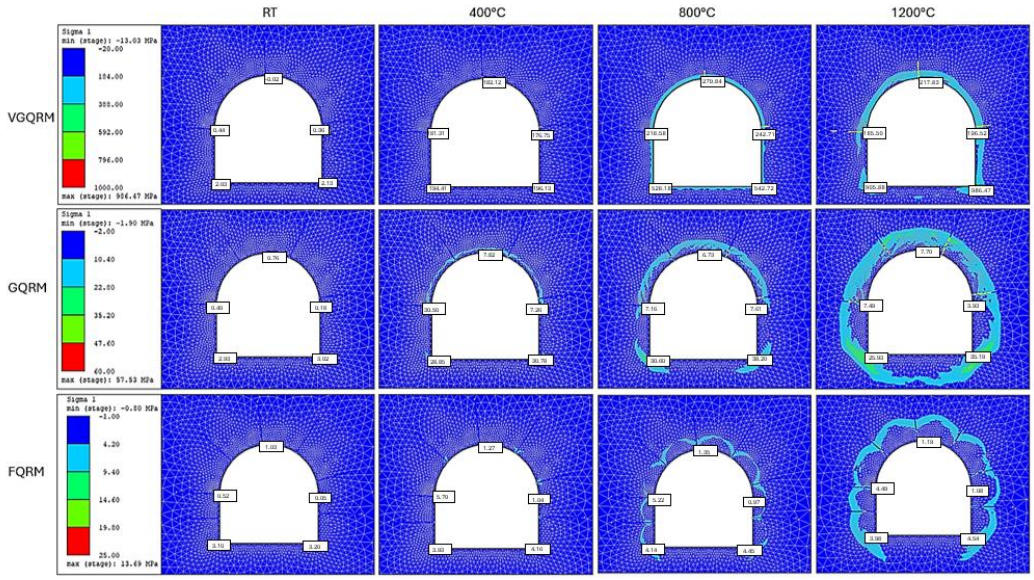

Figure 4.5. The major principal stress (σ_1) around the fire zone (L2) for all three rock mass classes.

4.3 Fire Induced Damage in a Large-Scale Fire

In VGQRM, the yielding pattern until 800°C is very similar to the small-scale case of VGQRM, forming tensile stress localizations at 600°C around both openings and exceeding the tensile strength of the bolts, rendering them inactive at 800°C. Starting from 850°C, the FIDZ surrounding the left opening progresses more vertically, whereas the one around the right opening progresses more horizontally. This difference becomes more obvious at higher temperatures. The interaction with the adjacent levels occurs between 850 and 900°C, starting on the right opening first. The damage spreads with increasing temperatures, affecting the far ends of the upper and lower levels and merging with them at 1050°C and 1100°C, respectively.

The presence of excavations above and below fire zones affects the flow of the thermal damage zone and changes the concentration accordingly. Due to an excavation above the fire zone, the damage zone is directly influenced, progressing more and more towards the opening rather than sideways. At 1200°C, the maximum

horizontal extent of the FIDZ from the excavation boundary is 5.6 m for the left opening and 7.7 m for the right opening. However, for the vertical extent from the excavation boundary, the left opening reaches 7 m and the right opening only 5.5 m. In the case of heavy support, the vertical extent of the right opening reaches 6.4 m. Additionally, the total displacements are concentrated on sharp edges for both fire zones and on the region between the crown and above level in the left zone. The major principal strains and the major principal plastic strains are concentrated on the floor, crown, and left side of the left opening as well as the region between the opening and the above level. For the right opening, the concentration is on the floor only. The progression of the yielded zone in both openings is illustrated in Figure 4.6 from RT to 1200°C.

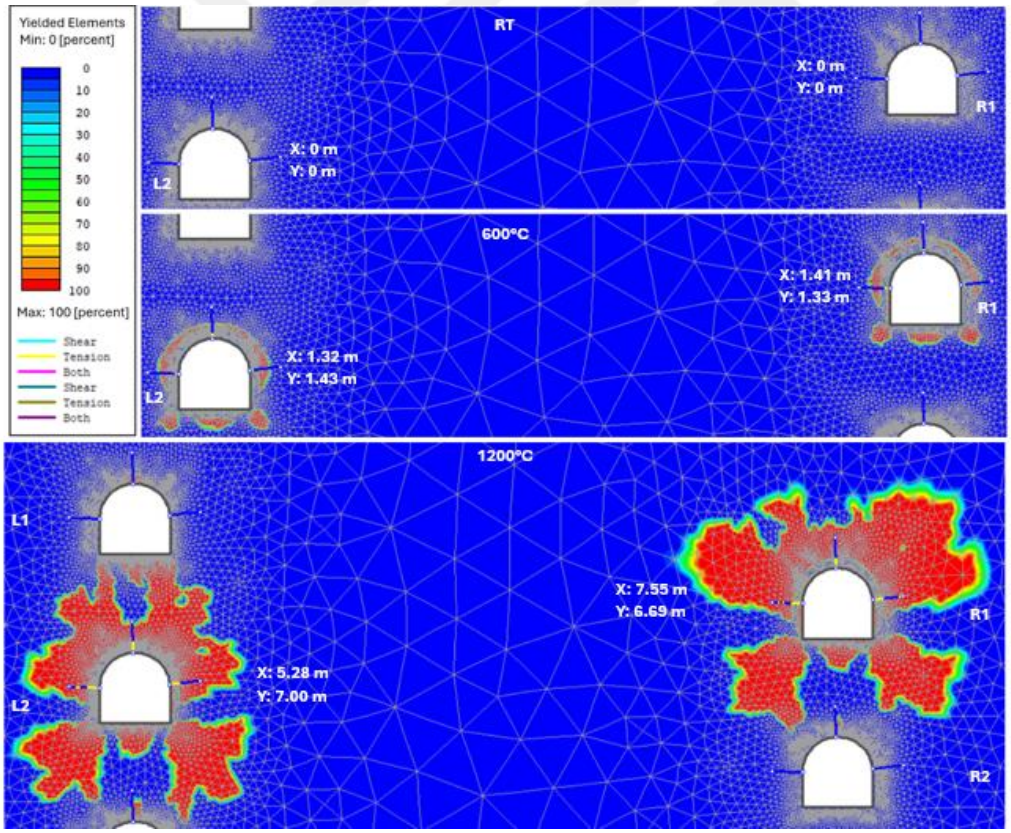

Figure 4.6. The extent of the thermal damage zone in VGQRM (X and Y values represent the maximum horizontal and vertical spans respectively).

In the case of GQRM, the damage pattern of the excavations is quite similar to each other and to the case of small-scale fire until 500°C. Between 600°C and 850°C, a tensile-stress localization starts to form above the excavations. The FIDZ around the right opening progresses much faster than the left opening due to a higher concentration of differential stresses around the right excavation within that temperature range. At 500°C, the bolts are partially inactive, and at 900°C, they have completely failed. As the fire temperature exceeds 1050°C, the interaction with the nearest excavations starts, with shear failure occurring on the floor of the upper and the roof of the lower levels near both the fire-affected zones. When the temperatures reach 1100°C, the interaction of the damage zone with the upper level intensifies, eventually merging with its boundary. The FIDZ below the fire-affected zones intensify as well. Similar to the case of the large-scale fire in VGQRM, the FIDZ formed on the left opening is more vertical, and the right opening is more horizontally spread. In both light and heavy support cases, the damage zone above the crown on the left reaches 7 m vertically, while the right one reaches only around 6 m. Horizontally, the damage zone formed at the right opening reaches 5.84 m from the closest boundary, while that of the left opening reaches only 4.98 m in both cases.

The total displacement in both light and heavy support cases is mainly concentrated at the excavation boundaries and slightly in the zone between the excavation and closest ramp levels. The major principal strain is concentrated mostly on the crown region and at the sharp edges in heavy supports, whereas in light supports it affects the walls as well. The major principal plastic strains are uniformly distributed at the excavation boundary in both cases. The progression of the yielded zone in both openings for the lightly supported case is illustrated in Figure 4.7.

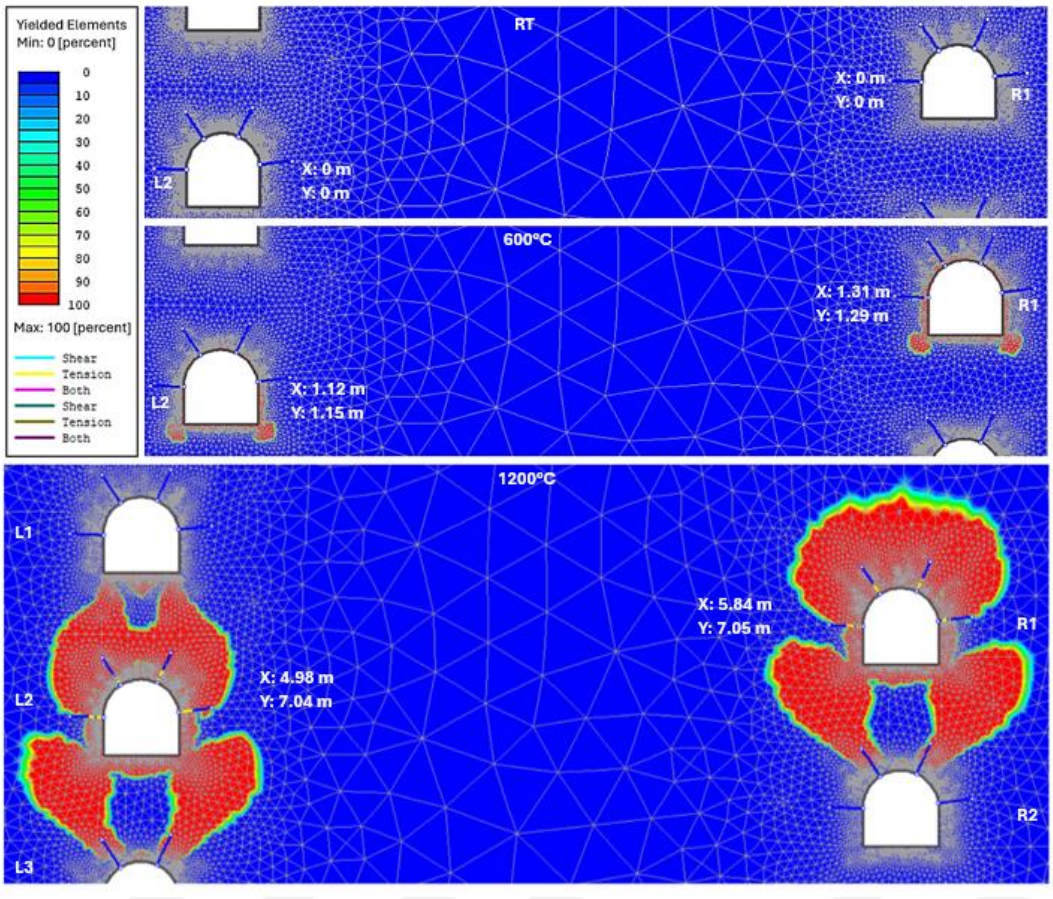

Figure 4.7. The extent of the thermal damage zone in GQRM (X and Y values represent the maximum horizontal and vertical spans respectively).

In FQRM, the damage zone first appears at 50°C and spreads with an increasing temperature. This zone progresses through the bolt region, detaching them slowly starting at 230°C, making them lose their function entirely by 500°C. When the temperatures are between 800°C and 1100°C, a higher concentration zone forms close to the crown and sharp edges near both fire zones but progresses faster around the right opening. The FIDZ is quite uniform around the excavation boundaries in FQRM, with a higher concentration on sharp edges. At temperatures higher than 1050°C, crown problems are more pronounced. At 1200°C, the fire zone starts to interact with the upper level, leading to a shear failure on the floor of the upper opening. The FIDZ surrounding the right opening is slightly more spread in both

width and height, reaching a horizontal extent of 3.88 m from the closest boundary, whereas the one on the left reaches up to 3.60 m only. The vertical extent of the right excavation reaches 3.94 m, while the one on the left spans to 3.58 m only. The total displacement in FQRM is concentrated around the excavation boundaries. The major principal strain as well as the major principal plastic strain are concentrated around the excavations as well, mostly at the bolt regions and sharp edges. The extent of the damage zone is illustrated in Figure 4.8.

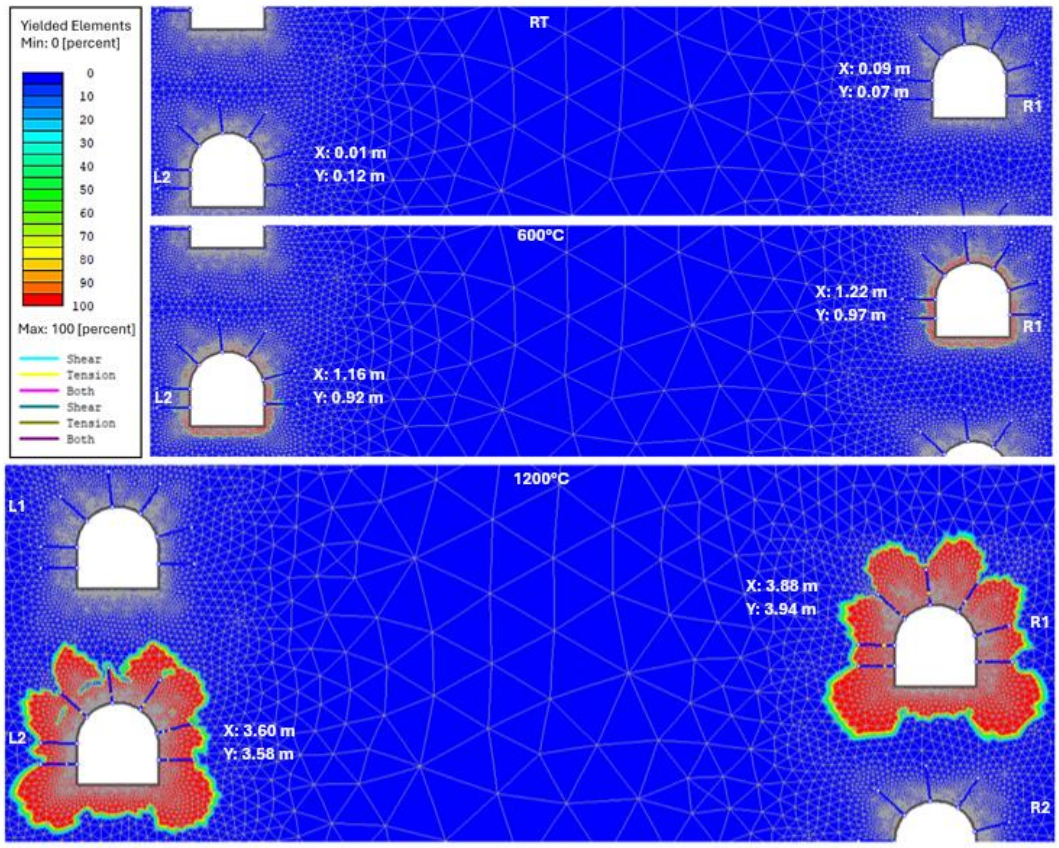

Figure 4.8. The extent of the thermal damage zone in FQRM (X and Y values represent the maximum horizontal and vertical spans respectively).

The progression of FIDZ in all three rock mass quality classes is similar in small- and large-scale fires in the corresponding openings. It can be observed that

the right openings have a more horizontally spread FIDZ, contrary to the vertical extension of the left zone. This can be explained by the presence of an excavation close enough above the left opening, which is directing the development of FIDZ and worsening the spread. In all three cases, the sharp edges reveal higher damage concentrations due to thermal and mechanical loading. In all three cases, the major principal stress is concentrated on sharp edges as well, proving that sharp edges are highly unstable in excavations where mine fires are possible. The distribution of the major principal stress around both left and right openings at 1200°C is illustrated in Figure 4.9 for VGQRM, GQRM, and FQRM. Contours for the total displacement at 1200°C are shown in Appendix C.

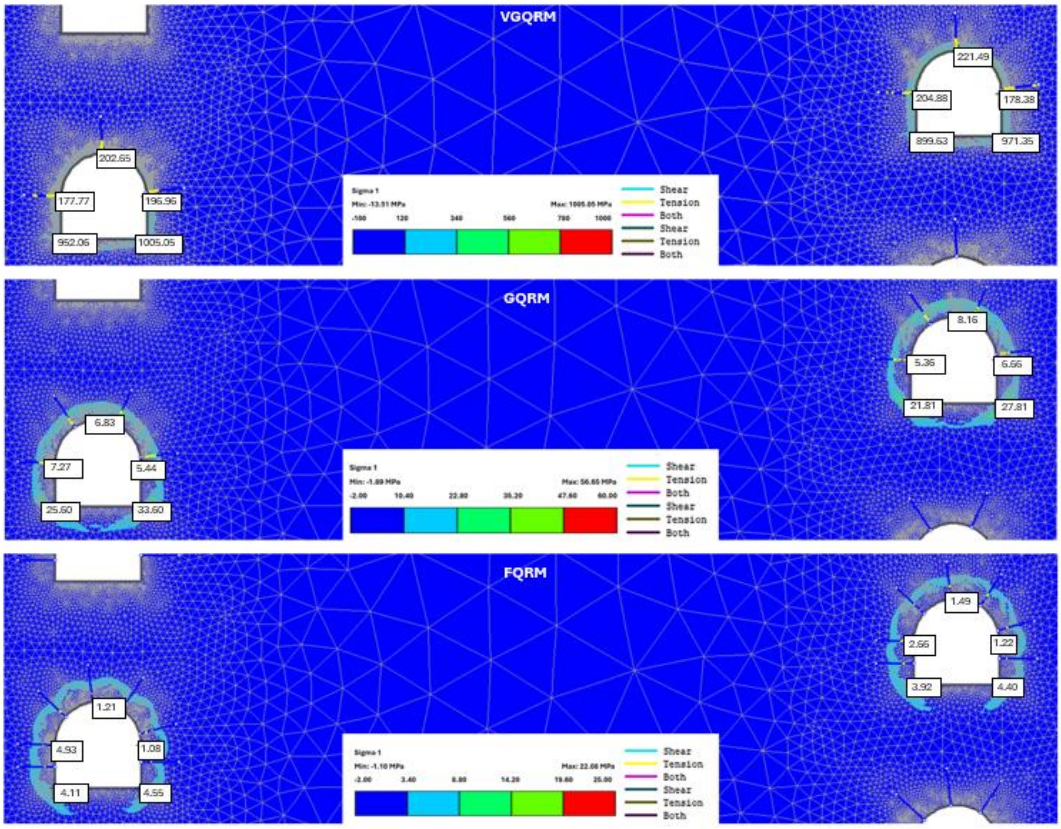

Figure 4.9. Major principal stress (σ_1) around the fire zones (L2 and R1) for all rock mass classes at 1200°C.

A summary of the results and span of FIDZ in all the models is given in Table 4.1.

Table 4.1. Summary of the numerical outcomes.

Rock Mass Qualities	VGQRM		GQRM		FQRM	
Scale of fire	Small	Large	Small	Large	Small	Large
Initiation of the damage zone (°C)	150	150	70	70	50	50
Development of the tensile stress ring (°C)	600	600	650	600	850	800
Interaction with lower level (°C)	850	850	1050	1050	-	-
Interaction with upper level (°C)	900	900	1050	1050	1200	1200
Merging with upper level (°C)	1050	1050	1100	1100	-	-
Tension on the bolts (VGQRM)/ Start of the yielding near the bolts (GQRM, FQRM) (°C)	190	190	250	250	230	230
The bolts become completely inactive by (°C)	800	800	900	900	500	500

4.4 Effects of Road Grade on the Fire Induced Damage

The influence of different road grades in the underground mine ramp was modeled to understand the associated changes in stress and strain, as well as in the progression of the fire-induced damage zone around the excavations. In one of the models, the road grade was taken as 12%, and in the other as 10%. This made the distance between two successive excavations 7 m and 5 m, respectively.

In VGQRM with small-scale fire, the maximum stress concentration is higher in the case of 12% grade until 400°C, after which it becomes lower until 650°C and higher again until 1200°C. The minimum stress concentration reaches higher values in the case of 10% grade until 650°C, after which the values are higher in the 12% case until 1200°C. Variations between the distribution of maximum principal stress

are given in Figure 4.10 for 600°C, 900°C, and 1200°C. In the case of a 10% road grade, the total displacement is concentrated on the crown and sharp edges. In the 12% road grade case, it extends to the floor as well. In both cases, the immediate walls and floor region have the least displacement. The maximum shear plastic strain and the major principal strains in both cases are concentrated on the crown and floor but also extend to the walls and the region above the excavation.

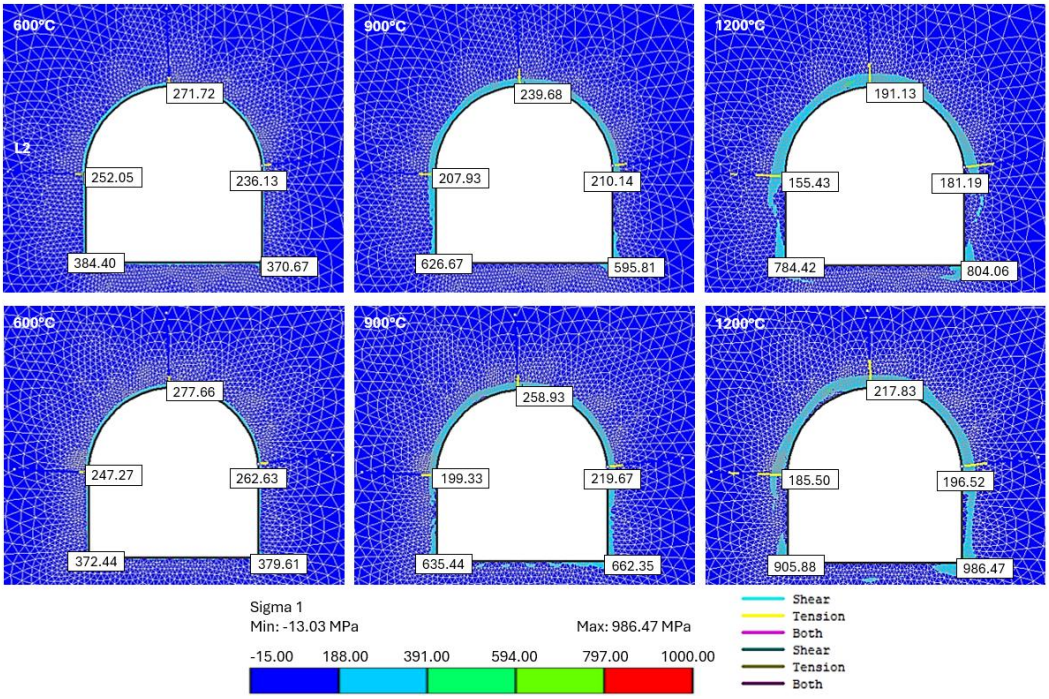

Figure 4.10. Stress contours for 10% (above) and 12% (below) road grade cases for 600°C, 900°C, and 1200°C a during a small-scale fire for VGQRM.

The progression of the fire-induced damage zone is similar in both cases until 600°C. In the case of a 10% road grade, interaction with the upper level starts at 700°C, and with the lower level it starts at 800°C. The damage zone is more concentrated on the shoulders and sharp edges, followed by the crown and floor regions. In the case of a 12% road grade, the concentration is higher around the entire crown and sharp edges, followed by the floor region. The interaction with the upper

and lower floors start at 900°C in this case. Also at 900°C, in the case where the distance between successive excavations is smaller, the damage zone merges with the upper opening, creating a roof failure for the above region and involving the entire 5 m distance above. At the same temperature, when the distance was greater, the damage only reached 3.4 m. With more distance between the levels, the rock mass withstands the high temperature, and the failure occurs much later, after 1000°C. In the case of a 10% grade, the far ends of the upper and lower excavations are affected at 950°C and 1000°C, respectively. For the case of 12% road grade, this effect is delayed to 1050°C and 1100°C, respectively. The difference in the progression of the damage zone can also be seen in Figure 4.11 for 600°C, 900°C, and 1200°C.

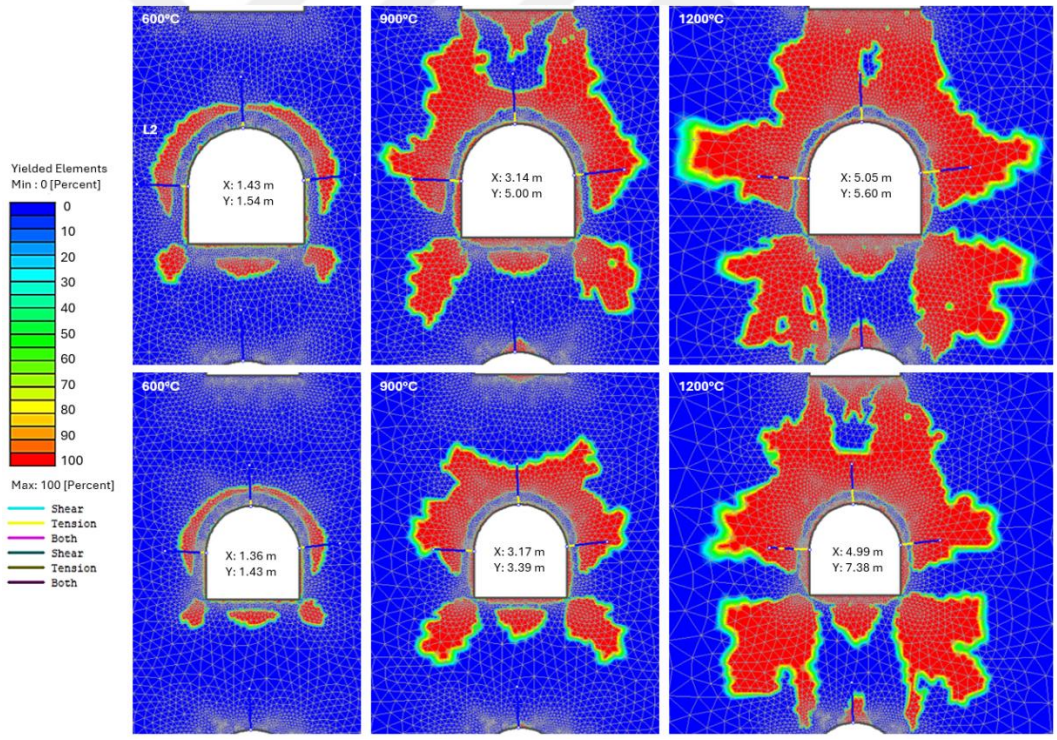

Figure 4.11. Progression of damaged zone for 10% (above) and 12% (below) road grade cases for 600°C, 900°C, and 1200°C during a small-scale fire for VGQRM.

When the scale of fire increases, no relation between maximum stress concentration is observed between different road grade cases; however, in general, the stress increases with increasing temperatures. Variations between the distribution of maximum principal stress at 1050°C are given in Figure 4.12. The minimum stress concentration reaches higher values in the 10% road grade case as compared to the 12% case. Moreover, σ_3 is concentrated around the excavation, focusing on the sharp edges. In the case of smaller vertical distance, the total displacement is concentrated on the sharp edges and in the region towards the above opening. In the large-distance case, it is only concentrated near sharp edges. The maximum shear plastic strain in both cases is concentrated on the floor but also extends to the walls when the distance is shorter. The major principal strains are concentrated more on the floor and the crown and extend to the region above the excavation when the road grade is 10%.

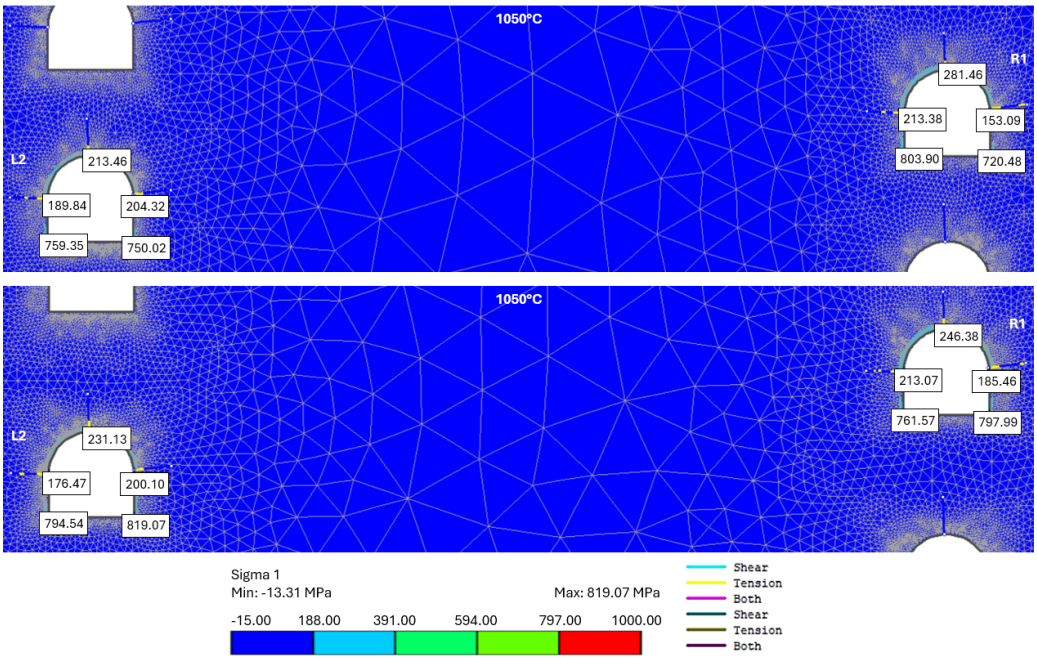

Figure 4.12. Stress contours for 10% (above) and 12% (below) road grade cases at 1050°C during a large-scale fire for VGQRM.

The progression of the fire-induced damage zone starts earlier in the 12% case and later when the gradient is smaller. They then progress in a similar way until 500°C. The right excavation is affected more than the left one at any given temperature in both cases. After this temperature, the simulation with the smaller road grade gets more intense fire damage as compared to the other case, and the nearby excavations get affected as well. At 700°C the upper excavation's floor is affected, and at 750°C the crown of the lower opening follows. At 850°C, the crown of the lower excavation on the right opening is affected as well. The damage zone progresses above the opening, merging with its boundary at 950°C. At higher temperatures, the far ends of nearby excavations show shear failure. In the case of a 12% road grade, the nearby excavations are affected at 850°C (right) and 900°C (left). At 1050°C, the damage zone extended to the boundary of the above excavation as well, causing roof failure near the affected zone. Comparisons were only done until the temperature level of 1050°C because in the 10% road grade case, the model experienced large strain failure beyond that stage. The difference in the formed damage zone at 1050°C can be seen in Figure 4.13.

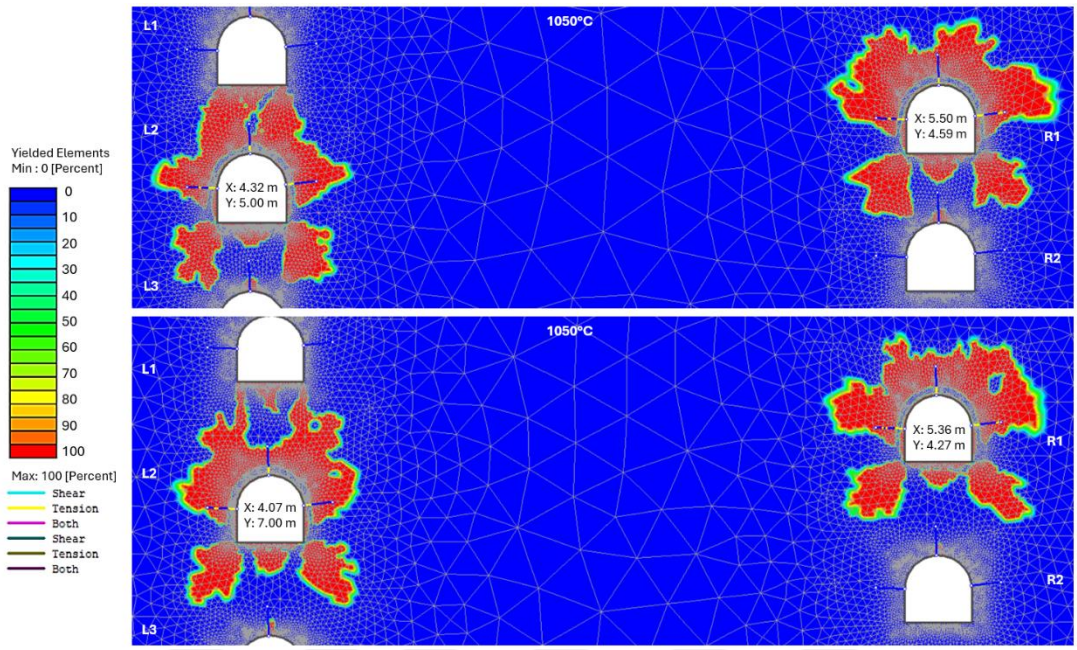

Figure 4.13. Progression of damaged zone for 10% (above) and 12% (below) road grade cases at 1050°C during a large-scale fire for VGQRM.

In GQRM, during a small-scale fire event, the maximum stress concentration is higher around the sharp edges and forms a high-stress ring around the excavation in both cases. When the road grade is smaller, the concentration extends to the upper and lower openings as well. For the minimum stress, the concentration forms a higher stress ring around the excavations, and the pattern is similar in both the 10% and 12% cases. In the case of a 10% road grade, the concentration extends to the nearby openings as well. The distribution patterns of maximum principal stresses are given in Figure 4.14 for 600°C, 900°C, and 1200°C. The total displacement in both cases is concentrated at the excavation boundary, especially on the walls. In the case of a 10% road grade, it also extends towards the closest openings. The maximum shear plastic strain and the major principal strains in both cases are concentrated around the excavation boundary as well.

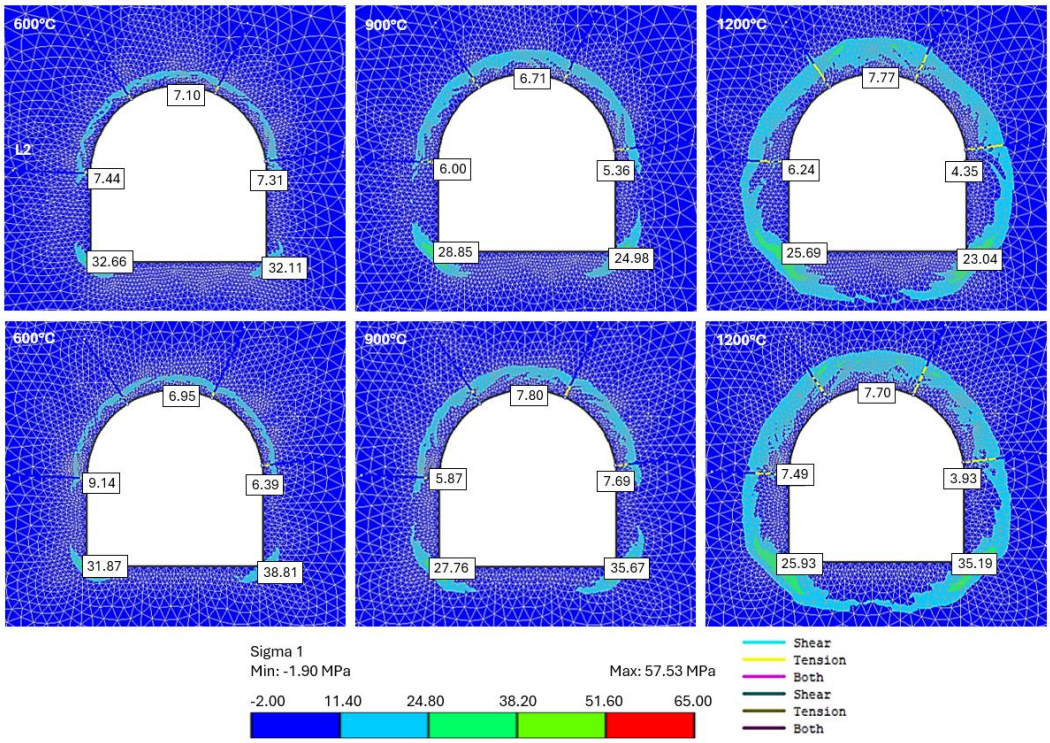

Figure 4.14. Maximum stress contours for 10% (above) and 12% (below) road grade cases for 600°C, 900°C, and 1200°C during a small-scale fire for GQRM.

The yielded zone around the openings initiates at 70°C and follows a similar pattern around the excavation. The damage zone progresses through the bolt regions, due to which the bolts lose most of their capacity by 600°C in the 10% case and by 650°C in the 12% case. In the case of a 10% road grade, the bolts lose their entire capacity by 850°C, and at the same temperature, the interaction with the upper opening starts. At 900°C, the interaction with the lower opening starts as well. At temperatures of 1000°C and 1200°C, entire zones towards the upper and lower openings fail, respectively. At 1100°C, the far end of the upper excavation fails due to shear stresses, and the far end of both lower excavations follows at 1200°C. In the case of a 12% grade, bolts completely fail at 900°C. Additionally, the interaction with upper and lower openings starts much later, at 1050°C, merging with the upper opening at 1100°C and almost merging with the lower at 1200°C. The far end of the

above excavation is affected in this case as well, but only at 1200°C. Figure 4.15 illustrates the development of the damage zone at 600°C, 900°C, and 1200°C.

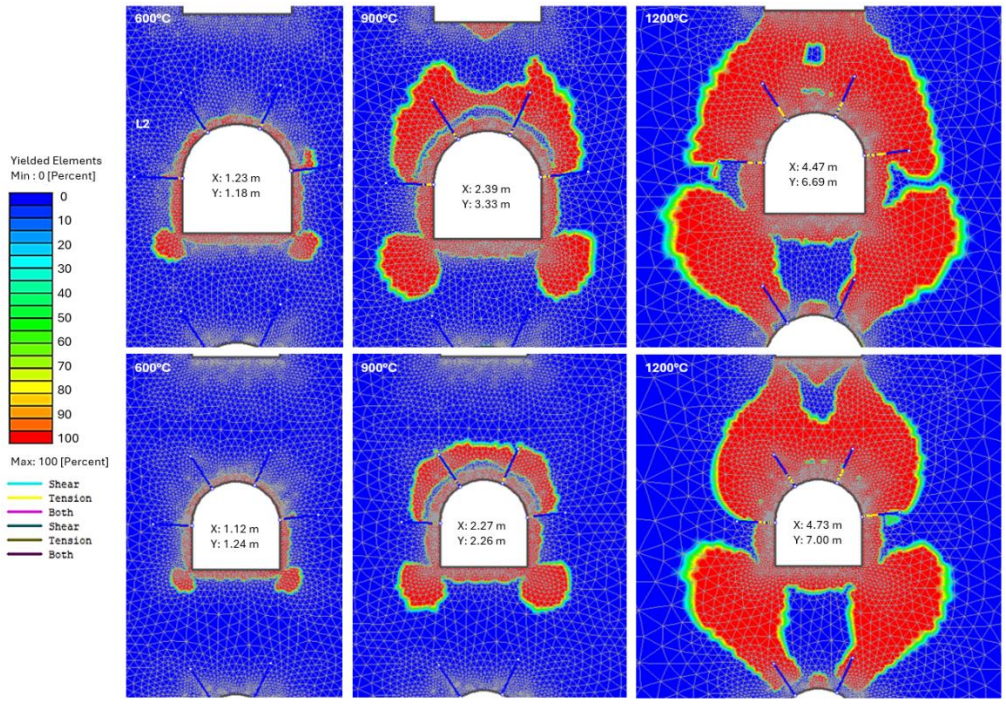

Figure 4.15. Progression of fire-induced damaged zone (FIDZ) for 10% (above) and 12% (below) road grade cases for 600°C, 900°C, and 1200°C during a small-scale fire for GQRM.

In the case of a large-scale fire, the concentration of maximum stress is at the sharp edges and in the shape of a high-stress ring around the excavations. Similar to the small-scale scenario, the 10% road grade case has higher stresses close to the nearest excavations as well. This can be seen in Figure 4.16 for 1200°C. The concentration of the total displacement is similar to the small-scale fire case, where it is around the excavation boundary and extends to nearby openings when the distance is smaller. The plastic strain concentrations are also similar to the small-scale fire case, mostly being around the excavation boundaries.

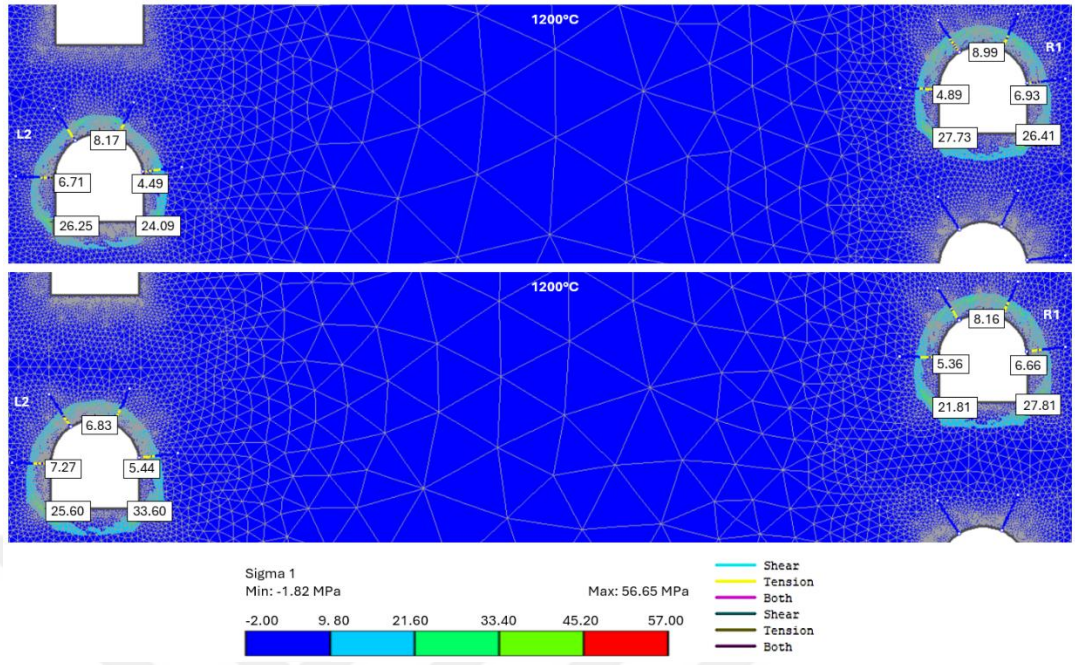

Figure 4.16. Stress contours for 10% (above) and 12% (below) road grade cases at 1200°C during a large-scale fire for GQRM.

The fire-induced damage starts at 70°C and propagates around the excavation boundary. It advances through the bolt region, inactivating the bolts partially when the temperature reaches 600°C in the 10% road grade case and at 650°C in the 12% case. In the 10% scenario, the damage zone progresses faster on the left side, where there are excavations close to the fire zone. This enables a complete failure of the bolts at 850°C. The damage zone starts affecting the above opening at 850°C as well. The lower opening on the right is affected at 900°C, and that on the left at 950°C. The region above the fire zone on the left completely fails at 1000°C, and the region below fails at 1150°C (right) and 1200°C (left). The damaged zone progresses more horizontally on the right side, where there is no excavation above it. However, on the left side, it is influenced by the presence of the excavation above it, and the damage zone is more vertically stretched. Here, the far end of the above excavation is also affected, at 1150°C. In the case of a 12% road grade and a larger distance between two successive openings, the damage zone on the right progresses faster

than the left one, leading to complete bolt failure at 900°C. The interaction with the nearby openings starts at 1050°C for all the excavations, failing due to shear forces. The yield zone merges with the above opening at 1100°C and almost merges with the lower one at 1200°C.

The FIDZ in GQRM is uniform around the excavation, with major concentrations at the crown and sharp edges. It starts to extend towards the upper and lower openings at 900°C and 1000°C, respectively, for the 10% case and at 1050°C and 1100°C for the 12% case. Figure 4.17 shows the damage zone in GQRM at 1200°C for both distances.

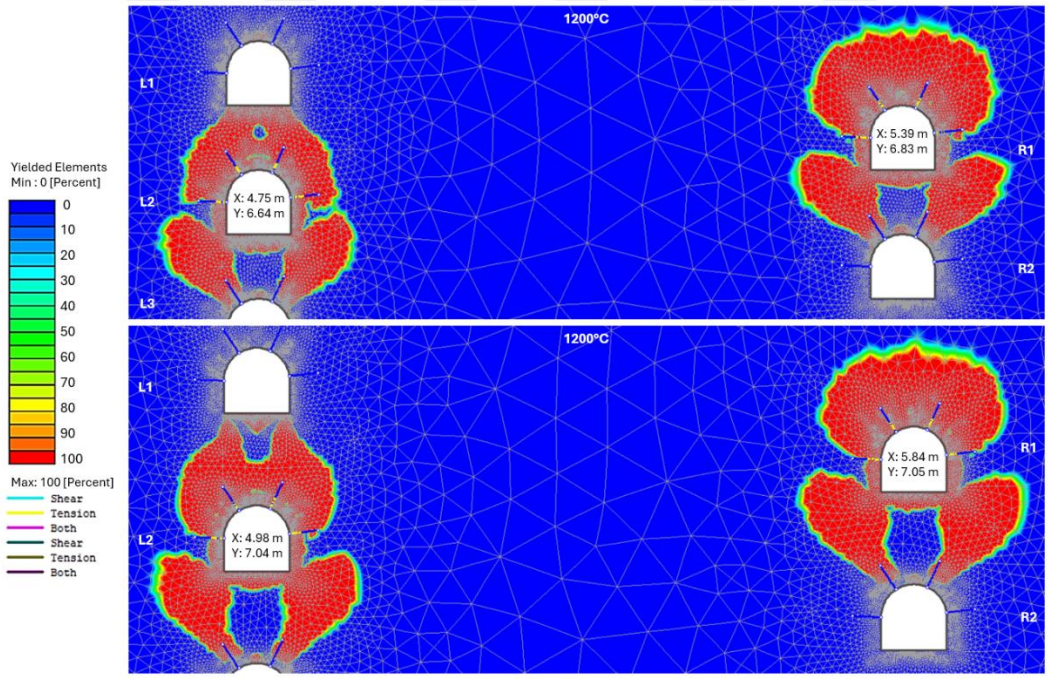

Figure 4.17. FIDZ for 10% (above) and 12% (below) road grade cases at 1200°C during a large-scale fire for GQRM.

In the case of FQRM, the maximum stress is higher in the case of 10% grade, from RT to 350°C, after which the opposite trend can be seen until 900°C, and again the 10% case becomes higher at 950°C to 1150°C. The concentration in both cases

is closer to the bolts and forms a high-concentration stress ring around the excavations. The values for σ_3 are higher in the 10% case until 190°C, after which the trend shifts until 850°C, and then back again between 900°C and 1200°C. The concentration of σ_3 is mostly around the bolts as well and forms a ring around the walls and crown of the excavations. σ_1 contours are given for both cases in Figure 4.18. The total displacement, maximum shear plastic strain, and major principal plastic strain contours are highest around the excavation boundary in both cases of FQRM.

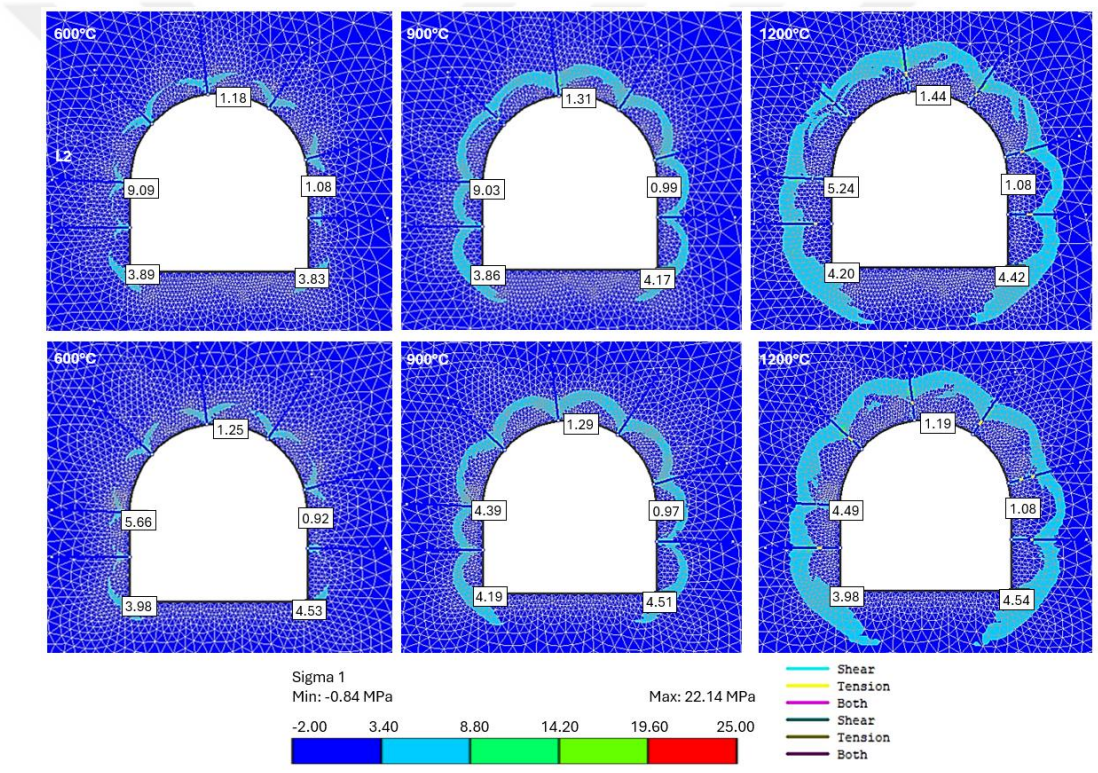

Figure 4.18. Stress contours for 10% (above) and 12% (below) road grade cases for 600°C, 900°C, and 1200°C during a small-scale fire for FQRM.

Studying the progression of the fire-induced damage zone, similar patterns can be observed in both cases. The yield zone forms around the opening boundary and progresses uniformly through the bolt region. This inactivates the bolts partially

by 450°C for the 10% grade case and 500°C for the 12% case, gradually detaching them from the excavation boundary. When temperatures reach 950°C, the entire bolt length is within the damage zone. The damage zone is very uniform around the excavation until 1000°C in the 10% case, after which it merges directly with the upper excavation at 1050°C, affecting both upper and lower excavations with increasing temperature. In the case of 12%, the uniformity is until 1150°C, after which it starts to interact with the upper excavation. This development of the FIDZ can be seen in Figure 4.19.

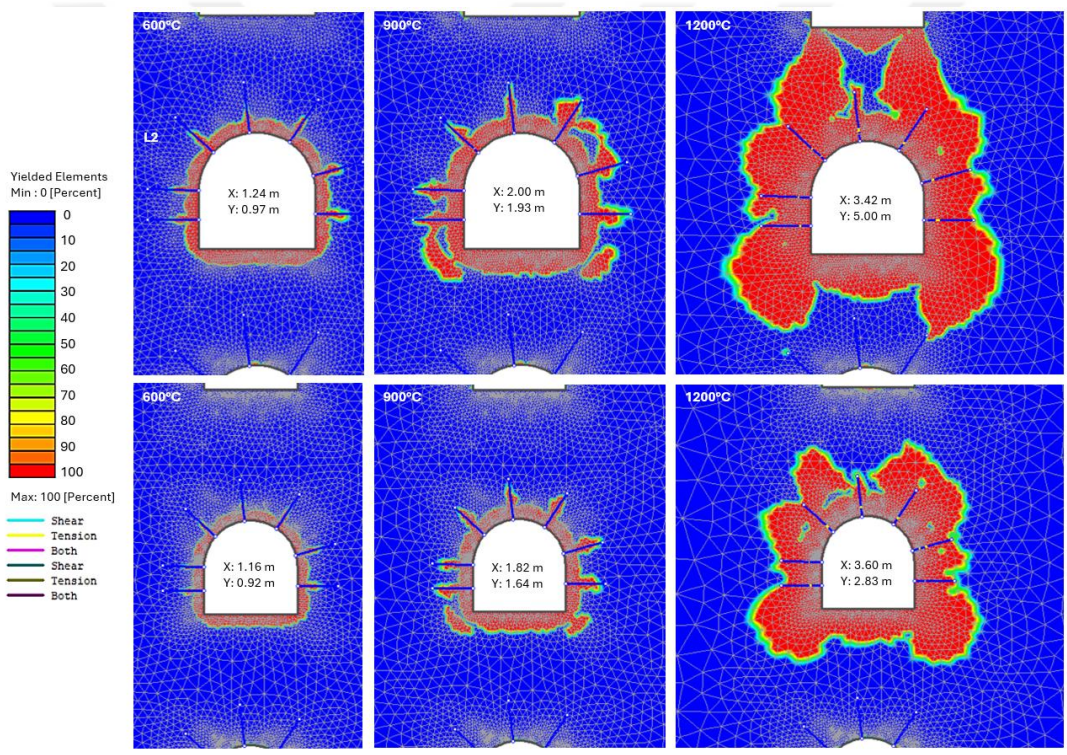

Figure 4.19. Development of FIDZ for 10% (above) and 12% (below) road grade cases for 600°C, 900°C, and 1200°C during a small-scale fire for FQRM.

When the fire extends to a larger scale, no visible trend can be observed in σ_1 and σ_3. The contours of both quantities are formed as a ring around the excavations, joined by higher concentration zones at the bolts. The total displacement and strain

contours are similar to the smaller-scale scenarios. The FIDZ inactivates the bolts partially at around 450°C in both cases and fully by 950°C in both cases. The development of FIDZ is faster in the left opening in the case of 5 m distance and in the right opening in the case of 7 m. This is because less distance affects the progression of the FIDZ and increases it, whereas more distance keeps it from forming faster. In the 12% road grade case, the FIDZ is quite uniform around the excavation and interacts with nearby openings at higher temperatures over 1150°C. However, in the case of 10%, the damage zone extends to the upper boundary at 1050°C and gradually interacts with the lower excavations afterwards. Figure 4.20 illustrates the progression of the FIDZ in a large-scale mine fire in FQRM.

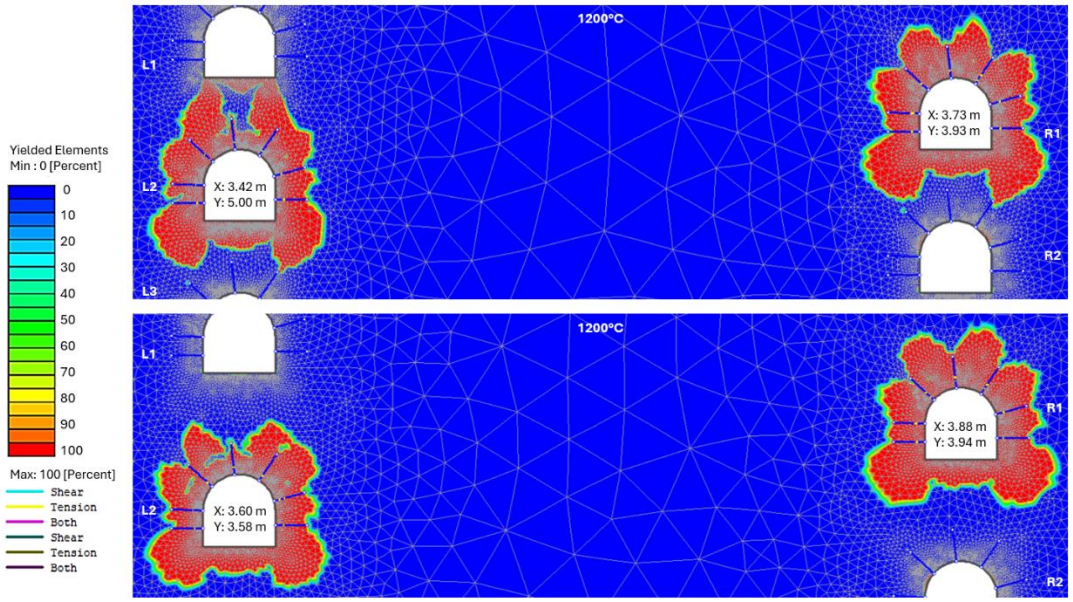

Figure 4.20. Development of FIDZ for the 10% (above) and 12% (below) road grade cases at 1200°C during a large-scale fire for FQRM.

4.5 Comparitive Analysis between Mechanical Modelling and Coupled Thermomechanical Modelling

In this section, a comparison between the outputs of mechanical models and coupled thermomechanical models is presented. Mechanical models simulate the behavior of excavations in thermally degraded material; however, no heat-stress interaction was added in the models themselves. Instead, degraded material properties are used for each successive stage to represent the effects of progressing fire temperatures. The material properties were found from experimental analysis, where core specimens of Ankara andesite were exposed to temperatures between 50°C and 1000°C and then tested for their strength in unconfined and confined settings. The resulting values were used to derive rock mass scale parameters with the help of RocData software for the three rock mass quality classes. These parameters were then used as input parameters in the 2D underground mine ramp models with a 12% road grade. The rock mass scale input parameters for VGQRM, GQRM, and FQRM are given in Tables 4.2-4.4, respectively.

Table 4.2. Material properties used in the mechanical models for VGQRM.

Temperature Level	Elastic Modulus (GPa)	Poisson's Ratio	Uniaxial Compressive Strength (MPa)	Tensile Strength (MPa)	Cohesion (MPa)	Internal Friction Angle (°)
RT	12630	0.21	51.7	1.00	3.38	62
100	14399	0.21	77.3	1.49	4.90	63
200	15156	0.21	60.0	1.16	3.88	63
400	15030	0.21	75.0	1.45	4.76	63
600	12766	0.21	56.2	1.09	3.65	63
800	12883	0.21	52.3	1.01	3.41	62
1000	8968	0.21	47.8	0.92	3.14	62

Table 4.3. Material properties used in the mechanical models for GQRM.

Temperature Level	Elastic Modulus (GPa)	Poisson's Ratio	Uniaxial Compressive Strength (MPa)	Tensile Strength (MPa)	Cohesion (MPa)	Internal Friction Angle (°)
RT	5154	0.21	10.3	0.17	1.09	59
100	5876	0.21	15.4	0.26	1.41	61
200	6185	0.21	12.0	0.20	1.20	59
400	6134	0.21	15.0	0.25	1.38	60
600	5206	0.21	11.2	0.19	1.14	59
800	5257	0.21	10.4	0.18	1.09	59
1000	3660	0.21	9.5	0.16	1.02	58

Table 4.4. Material properties used in the mechanical models for FQRM.

Temperature Level	Elastic Modulus (GPa)	Poisson's Ratio	Uniaxial Compressive Strength (MPa)	Tensile Strength (MPa)	Cohesion (MPa)	Internal Friction Angle (°)
RT	1103	0.21	2.2	0.03	0.54	50
100	1258	0.21	3.3	0.04	0.63	53
200	1323	0.21	2.5	0.03	0.57	51
400	1313	0.21	3.2	0.04	0.62	53
600	1114	0.21	2.4	0.03	0.55	51
800	1125	0.21	2.2	0.03	0.54	51
1000	783	0.21	2.0	0.02	0.52	50

While mechanical models use previously degraded material properties followed by mechanical testing, the coupled thermomechanical models simulate the effects of increasing temperatures in real time as a function of the duration of exposure to each temperature level. The coupled models, as described earlier, include both mechanical and thermal degradation of the rock mass by computing thermal and mechanical stresses for each stage to simulate the fire conditions. The mechanical models, however, describe the effects of excavation in previously

degraded rock mass. A comparison of the stress distribution as well as damage zones in both models is given in the following paragraphs.

In the mechanical models for VGQRM, no damage zone was formed, even when thermal treatment of 1000°C was considered; however, in the coupled model, the damage zone formed as early as 150°C. The variation between the damage zones at 1000°C is given in 4.21. The scale of the stress distribution is significantly larger in the coupled models as well. Variations in the distribution of σ_1 around the opening L2 between the two modelling approaches can be seen in Figure 4.22.

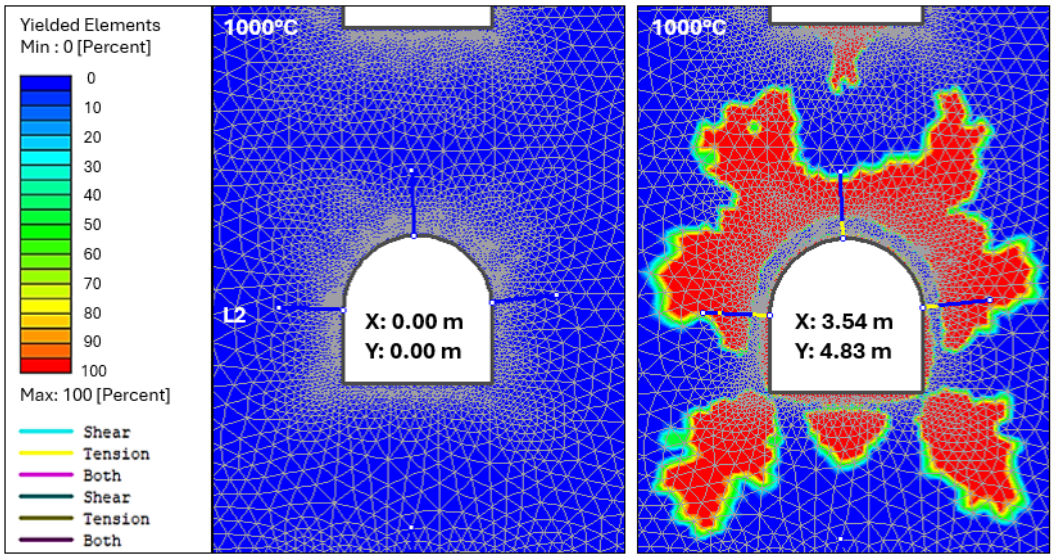

Figure 4.21. Variations in the damage zone around the opening L2 in VGQRM in mechanical model (left) and coupled thermo mechanical model (right) at 1000°C.

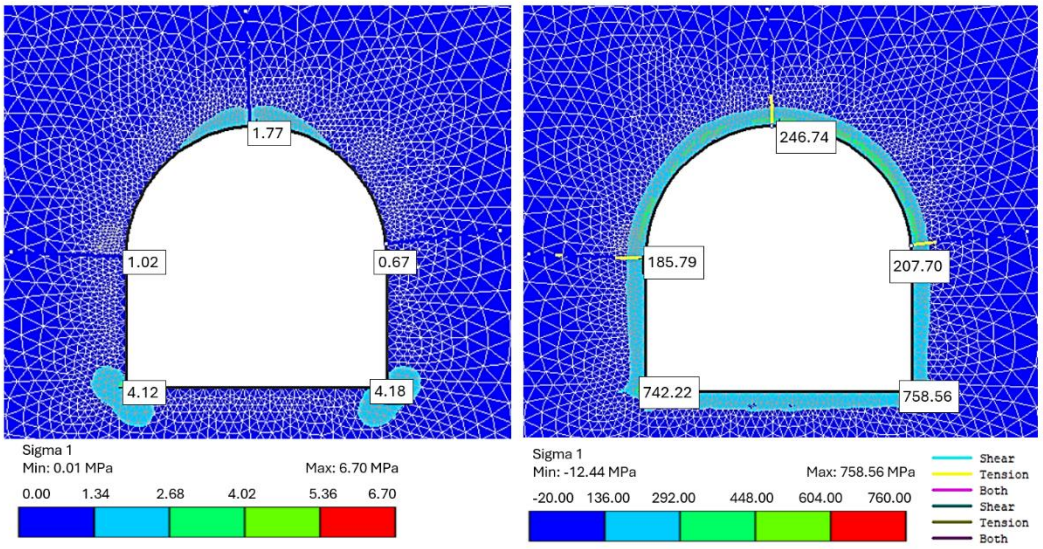

Figure 4.22. Variations in σ_1 around the opening L2 in VGQRM in mechanical model (left) and coupled thermo mechanical model (right) at 1000°C.

In the case of GQRM, no yielding can be observed near L2; however, the maximum extent of the damage zone across all excavations was no more than 10 cm at 1000°C in the mechanical model. This is significantly lower than that of the TM-coupled model, where it reaches up to 2.90 m, as can be seen in Figure 4.23.

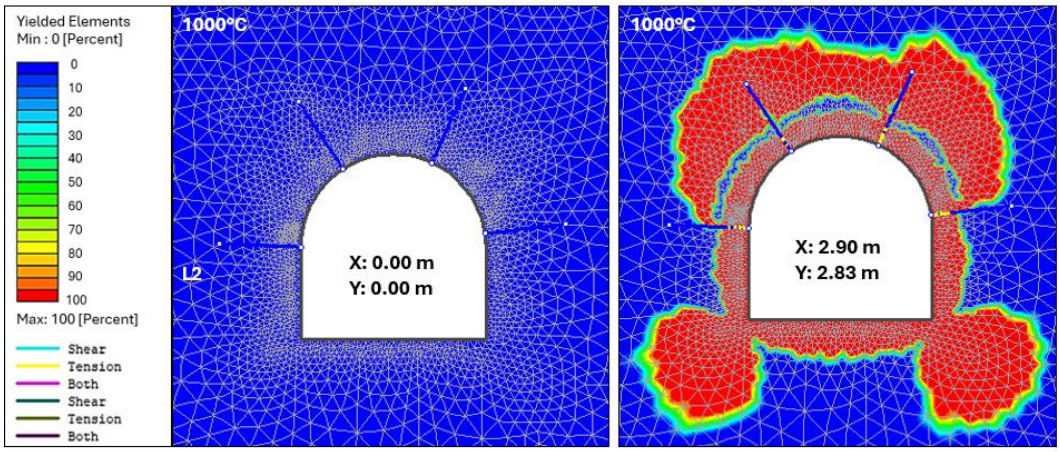

Figure 4.23. Variations in the damage zone around the opening L2 in GQRM in mechanical model (left) and coupled thermo mechanical model (right) at 1000°C.

The variations in the scale of stress is significant as well. This is illustrated in Figure 4.24.

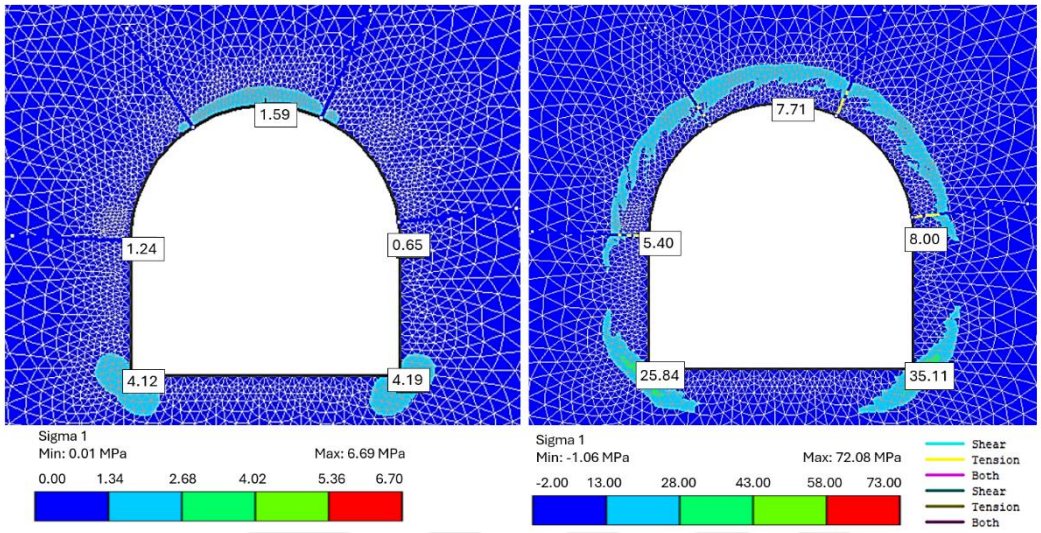

Figure 4.24. Variations in σ_1 around the opening L2 in GQRM in mechanical model (left) and coupled thermo mechanical model (right) at 1000°C.

For FQRM, a damage zone can be observed at the bolt regions in the mechanical model, but this zone does not exceed 16 cm. Comparing it to the coupled TM models, the extent of the damage zone reached 2.25 m. The comparison between the damage zones as well as the major principal stress contours are given in Figures 4.25 and 4.26, respectively.

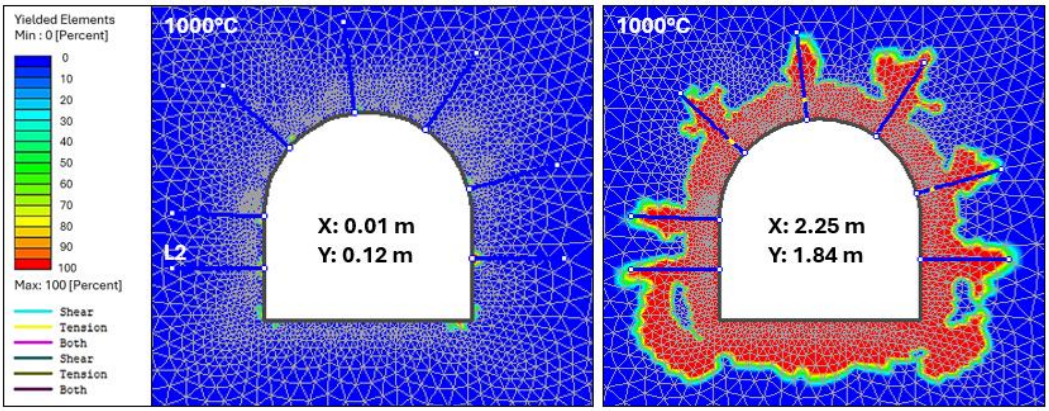

Figure 4.25. Damage zone surrounding L2 in mechanical model (left) and coupled thermo mechanical model (right) at 1000°C in FQRM.

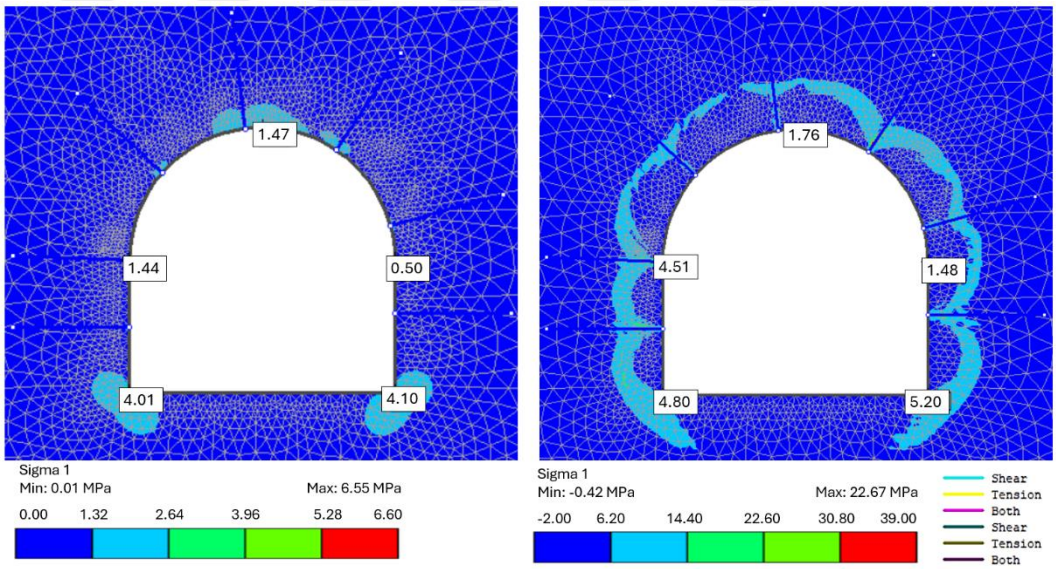

Figure 4.26. Variations in σ_1 around the opening L2 in mechanical model (left) and coupled thermo mechanical model (right) at 1000°C in FQRM.

While mechanical models are faster and easier to compute, coupled models are more costly in terms of time but describe better the damaging effect of fire on surrounding rock mass for different hard rock conditions. Even though degraded material properties were used in the mechanical models, it failed to display the

expected thermal damage around the excavation. The scale of damage was observed to be too small as compared to the coupled models. In VGQRM, the Fire-Induced Damage Zone (FIDZ) initiated at 150°C in the coupled models but was not formed in the mechanical models even at 1000°C. Similarly, for GQRM, the maximum extent of FIDZ at 1000°C was 2.90 m in the coupled models, whereas it did not exceed 10 cm in the mechanical models at the same temperature level. Likewise, in FQRM, the FIDZ was found to be 2.25 m in the coupled model and only 16 cm in the mechanical model at 1000°C. This variation in findings indicates that the mechanical models are insufficient in describing the thermal damage around an excavation during a fire event. This leads to the need for damage constitutive models to describe the coupled damage effect due to both mechanical and thermal loading.

CHAPTER 5

CONCLUSION

In this study, we have analyzed the effects of mine fires on different rock mass qualities by using numerical modeling. These effects were observed for the pre-, during-, and post-fire stages of a mine fire. In the stage before the occurrence of a mine fire, during regular day-to-day working conditions, the stress distribution was observed to intensify as the excavation depth increased.

During the occurrence of a mine fire, the results showed that the Fire-Induced Damage Zone (FIDZ) progressed with increasing temperatures in different patterns for different rock mass qualities. The first FIDZ appeared at 150°C in VGQRM, starting at the sharp edges and around the crown. In GQRM and FQRM, it starts earlier, at 70°C and 50°C, respectively, and spreads uniformly around the excavation. A tensile stress ring formed closer to the crown and floor regions at 600°C, then spread after each stage in VGQRM and GQRM. The damage zone affected the nearby openings starting at 850°C in VGQRM and at 1050°C in GQRM. This led to failure of the entire zone above the main excavation in VGQRM, and both upper and lower zones were majorly affected in GQRM when temperatures reached over 1050°C. High temperatures from fire also affected the bolts, starting at 190°C for VGQRM and 250°C for GQRM, rendering them completely inactive by 800°C and 900°C. In the case of FQRM, the damage was concentrated around the bolt region, loosening the bolts and making them ineffective by 500°C. The tensile ring in this case forms much later, at 850°C, and interacts with the upper opening at 1200°C. Overall, the damage zone in brittle rock mass VGQRM is more vertically spread, whereas it extends farther to the walls and floor in GQRM and is quite uniform in the case of FQRM.

The effects of the temperature increment on the mechanical properties of surrounding rock were experimentally analyzed to imitate the short-term post-fire conditions. An initial improvement in strength and stiffness was observed due to the increase in uniaxial compressive strength, elastic modulus, and internal friction angle until 400°C, followed by a drop to below initial values as the temperature increased to 1000°C. The tensile strength was observed to increase till 200°C and completely deteriorated afterwards. This remark also raises the need for a new material constitutive model for hard rocks that is capable of implementing the changes in strength and stiffness parameters with changing temperature levels. It was also noted that at 1100°C, the rock sample would no longer be defined as a solid-phase material.

The numerical study highlighted changes in the damage zone due to the presence of different support configurations. Applying heavier support in some cases delayed the extent of the damage zone, indicating a slight improvement in the rock stability. Moreover, the presence of excavations above the fire zone provided a clear manipulation in the progression of FIDZ, directly influencing its shape and extent.

Finally, the effects of the different road grades were also observed. Changing the grade of the underground mine ramp significantly affected the progression of the damage zone, especially at mid temperature levels. Shorter distances due to lower road grade lead to earlier interaction and merging between excavation boundaries, whereas it was delayed when the road grade was larger.

The mechanical models in this study were based on the thermal degradation of material properties derived from experimental analysis. The coupled thermomechanical models, on the other hand, relied on stage-wise accumulation of thermal and mechanical stresses due to increasing temperatures. Although the coupled models provide valuable insights on the extent and localization of the fire-induced damage expected after a fire, they do not fully show the damage evolution during the fire growth stage. To understand that, future research should include a coupled thermomechanical experimental setup performed under true triaxial loading to characterize the material behavior under different loading conditions.

Additionally, a damage constitutive model must be used for verifying the experimental setup as well as to understand the evolution of thermal cracks in the model. These suggestions for future research will offer a deeper understanding of the real-time damage effects and crack growth during a fire event and in the post-fire stage.

REFERENCES

Abraham, O., Dérobert, X., 2003. Non-destructive testing of fired tunnel walls: the Mont-Blanc Tunnel case study. NDT & E International 36, 411–418. https://doi.org/10.1016/S0963-8695(03)00034-3

Aksoy, C.O., Aksoy, G.G.U., Fişne, A., Alagoz, I., Kaya, E., 2024. Investigation of a conveyor belt fire in an underground coal mine: Experimental studies and CFD analysis. J South Afr Inst Min Metall 123, 589–597. https://doi.org/10.17159/2411-9717/1613/2023

Alemdag, S., Gurocak, Z., Gokceoglu, C., 2015. A simple regression based approach to estimate deformation modulus of rock masses. Journal of African Earth Sciences 110, 75–80. https://doi.org/10.1016/j.jafrearsci.2015.06.011

Aydan, Akagi, T., Kawamoto, T., 1993. The squeezing potential of rocks around tunnels; Theory and prediction. Rock Mech Rock Eng 26, 137–163. https://doi.org/10.1007/BF01023620

Aydan, O., Dalgic, S., 1998. Prediction of deformation behaviour of 3-lanes Bolu tunnels through squeezing rocks of North Anatolian fault zone (NAFZ), in: Proceedings of the Regional Symposium on Sedimentary Rock Engineering. Taipei.

Aydan, O., Kawamoto, T., 2001. The Stability Assessment of a Large Underground Opening at Great Depth , in: 1 7th Internationa! Mining Congress and Exhibition of Turkey- İMCET 2001. Ankara, pp. 277–288.

Barton, N., 2002. Some new Q-value correlations to assist in site characterisation and tunnel design. International Journal of Rock Mechanics and Mining Sciences 39, 185–216. https://doi.org/10.1016/S1365-1609(02)00011-4

Barton, N., Loset, F., Lien, R., Lunde, J., 1980. Application of the Q-system in design decisions. Subsurface Space 2, 553–561.

Barton, N., Pandey, S.K., 2011. Numerical modelling of two stoping methods in two Indian mines using degradation of c and mobilization of φ based on Q-parameters. International Journal of Rock Mechanics and Mining Sciences 48, 1095–1112. https://doi.org/10.1016/j.ijrmms.2011.07.002

Bhasin, R.K., Barton, N., Grimstad, E., Chryssanthakis, P., Shende, F.P., 1996. Comparison of predicted and measured performance of a large cavern in the Himalayas. International Journal of Rock Mechanics and Mining Sciences & Geomechanics Abstracts 33, 607–626. https://doi.org/10.1016/0148-9062(95)00082-8

Bieniawski, Z.T., 1978. Determining rock mass deformability: experience from case histories. International Journal of Rock Mechanics and Mining Sciences & Geomechanics Abstracts 15, 237–247. https://doi.org/10.1016/0148-9062(78)90956-7

Cai, M., 2009. A simple method to estimate tensile strength and Hoek-Brown strength parameter mi of brittle rocks, in: Diederichs, M., Grasselli, G. (Eds.), Proceedings of the 3rd CANUS Rock Mechanics Symposium. Mansour Group of Companies, Toronto.

Cai, M., Kaiser, P.K., Uno, H., Tasaka, Y., Minami, M., 2004. Estimation of rock mass deformation modulus and strength of jointed hard rock masses using the GSI system. International Journal of Rock Mechanics and Mining Sciences 41, 3–19. https://doi.org/10.1016/S1365-1609(03)00025-X

Cai, W., Zhu, H., Liang, W., 2022. Three-dimensional tunnel face extrusion and reinforcement effects of underground excavations in deep rock masses. International Journal of Rock Mechanics and Mining Sciences 150, 104999. https://doi.org/10.1016/j.ijrmms.2021.104999

Dinc, O.S., Sonmez, H., Tunusluoglu, C., Kasapoglu, K.E., 2011. A new general empirical approach for the prediction of rock mass strengths of soft to hard rock masses. International Journal of Rock Mechanics and Mining Sciences 48, 650–665. https://doi.org/10.1016/j.ijrmms.2011.03.001

El-Naqa, A., Al Kuisi, M., 2002. Engineering geological characterisation of the rock masses at Tannur Dam site, South Jordan. Environmental Geology 42, 817–826. https://doi.org/10.1007/s00254-002-0589-9

Erdakov, P., Khokhryachkin, D., 2005. Impact of fire on the stability of tunnels. Luleå University of Technology, Luleå.

Fehérvári, S., 2008. Characteristics of Tunnel Fires. Concrete Structures 9, 56–60.

Fernández-Alaiz, F., Castañón, A.M., Gómez-Fernández, F., Bascompta, M., 2020. Mine Fire Behavior under Different Ventilation Conditions: Real-Scale Tests and CFD Modeling. Applied Sciences 10, 3380. https://doi.org/10.3390/app10103380

Gao, K., Liu, Z., Tao, C., Tang, Z., Aiyiti, Y., Shi, L., 2021. Fire behaviors along timber linings affixed to tunnel walls in mines. PLoS One 16, e0260655. https://doi.org/10.1371/journal.pone.0260655

Ge, Z., Sun, Q., Yang, T., Luo, T., Jia, H., Yang, D., 2021. Effect of high temperature on mode-I fracture toughness of granite subjected to liquid nitrogen cooling. Eng Fract Mech 252, 107834. https://doi.org/10.1016/j.engfracmech.2021.107834

Hansen, R., 2023. Varying Heat Release Rates per Unit Area – The Impact in Underground Mines. Mining Revue 29, 1–28. https://doi.org/10.2478/minrv-2023-0028

Hansen, R., 2019. Fire behaviour of multiple fires in a mine drift with longitudinal ventilation. Int J Min Sci Technol 29, 245–254. https://doi.org/10.1016/j.ijmst.2018.05.005

Hansen, R., 2017. Fire behavior of mining vehicles in underground hard rock mines. Int J Min Sci Technol 27, 627–634. https://doi.org/10.1016/j.ijmst.2017.05.010

Hansen, R., 2013. Investigation on fire causes and fire behaviour: Vehicle fires in underground mines in Sweden 1988–2010. Västerås.

Hansen, R., 2010. Overview of fire and smoke spread in underground mines, in: Fourth International Symposium on Tunnel Safety and Security. Frankfurt am Main.

Hoek, E., Brown, E.T., 1997. Practical estimates of rock mass strength. International Journal of Rock Mechanics and Mining Sciences 34, 1165–1186. https://doi.org/10.1016/S1365-1609(97)80069-X

Hoek, E., Diederichs, M.S., 2006. Empirical estimation of rock mass modulus. International Journal of Rock Mechanics and Mining Sciences 43, 203–215. https://doi.org/10.1016/j.ijrmms.2005.06.005

Jalote, P., Kumar, A., Kumar, V., 1996. Geotechniques applied in the design of the machine hall cavern, Nathpa Jhakri Hydel Project, N.W. Himalaya, India. Journal of Engineering Geology 25, 181–192.

Jha, D.K., Kaushik, S.K., Sharma, T.P., 1998. High-temperature effect on mechanical properties of fibrous concrete, in: International Symposium on Innovative World of Concrete - 98. Calcutta, pp. 1.19-1.29.

Kalamaris, G., Bieniawski, Z., 1995. A rock mass strength concept for coal incorporating the effect of time., in: Eighth International Congress on Rock Mechanics. Rotterdam.

Ke, G., Zimeng, L., Jinzhang, J., Zeyi, L., Yisimayili, A., Zhipeng, Q., Yaju, W., Shengnan, L., 2020. Study on Flame Spread Characteristics of Flame-Retardant Cables in Mine. Advances in Polymer Technology 2020, 1–7. https://doi.org/10.1155/2020/8765679

Keski-Rahkonen, O., Holmlund, C., Loikkanen, P., Ludvigsen, H., Mikkola, E., 1986. Two full scale pilot fire experiments in a tunnel. Espoo.

Kim, K., Kemeny, J., Nickerson, M., 2014. Effect of Rapid Thermal Cooling on Mechanical Rock Properties. Rock Mech Rock Eng 47, 2005–2019. https://doi.org/10.1007/s00603-013-0523-3

Kirkland, C.J., 2002. The fire in the Channel Tunnel. Tunnelling and Underground Space Technology 17, 129–132. https://doi.org/10.1016/S0886-7798(02)00014-7

LaCroix, D., 2001. The Mont-Blanc Tunnel fire – what happened and what has been learned, in: Proceedings of the Fourth International Conference on Safety in Road and Rail Tunnels. Madrid, pp. 3–15.

Lahouar, M.A., Pinoteau, N., Caron, J.-F., Foret, G., Rivillon, P., 2018. Fire design of post-installed bonded rebars: Full-scale validation test on a 2.94 × 2 × 0.15 m3 concrete slab subjected to ISO 834-1 fire. Eng Struct 174, 81–94. https://doi.org/10.1016/j.engstruct.2018.07.069

Larsson, K., 2006. Fires in tunnels and their effect on rock: a review. Luleå.

Leitner, A., 2001. The fire catastrophe in the Tauern Tunnel: experience and conclusions for the Austrian guidelines. Tunnelling and Underground Space Technology 16, 217–223. https://doi.org/10.1016/S0886-7798(01)00042-6

Li, Z., Fortin, J., Nicolas, A., Deldicque, D., Guéguen, Y., 2019. Physical and Mechanical Properties of Thermally Cracked Andesite Under Pressure. Rock Mech Rock Eng 52, 3509–3529. https://doi.org/10.1007/s00603-019-01785-w

Lönnermark, A., Ingason, H., 2003. Large-scale fire tests in the Runehamar tunnel - Gas temperature and radiation, in: Ingason (Ed.), Proceedings of the International Symposium on Catastrophic Tunnel Fires (CTF). SP Swedish National Testing and Research Institute, Borås.

Lowndes, I., Morvan, H., Silvester, S., Pickering, S., Hart, R., Cai, Y., 2006. THE MODELLING OF FIRE SPREAD AND SUPPRESSION WITHIN UNDERGROUND MINE TUNNELS , in: Fifth International Conference on CFD in the Process Industries. Melbourne.

Lu, Y., Jiang, J., Wang, B., Chen, W., Ye, J., 2024. AI-based evaluation method of mechanical performance of shield tunnel structures after fire. Tunnelling and Underground Space Technology 150, 105858. https://doi.org/10.1016/j.tust.2024.105858

Ma, Z., Mäkeläinen, P., 2000. Parametric temperature–time curves of medium compartment fires for structural design. Fire Saf J 34, 361–375. https://doi.org/10.1016/S0379-7112(00)00008-4

Mielke, P., Nehler, M., Bignall, G., Sass, I., 2015. Thermo-physical rock properties and the impact of advancing hydrothermal alteration — A case study from the Tauhara geothermal field, New Zealand. Journal of Volcanology and Geothermal Research 301, 14–28. https://doi.org/10.1016/j.jvolgeores.2015.04.007

Narimani, S., Davarpanah, S.M., Vásárhelyi, B., 2023. Estimation of the Poisson's Ratio of the Rock Mass. Periodica Polytechnica Civil Engineering 68, 274–288. https://doi.org/10.3311/PPci.22689

NGI, 2022. Using the Q-system, 2nd ed. Norwegian Geotechnical Institute, Oslo.

NGI, 2015. Using the Q-system. Norwegian Geotechnical Institute, Oslo.

Nordlund, E., Zhang, P., Dineva, S., Saiang, C., Mainali, G., 2014. Impact of fire on the stability of hard rock tunnels in Sweden. Stockholm.

Ramamurthy, T., 1986. Stability of rock mass. Indian geotechnical journal 16, 1–75.

Ranasooriya, J., 2009. The Reliability of Rock Mass Classification Systems as Underground Excavation Support Design Tools. Curtin University of Technology, Perth.

Read, S., Richards, L., Perrin, N., 1999. Applicability of the Hoek-Brown failure criterion to New Zealand greywacke rocks, in: 9th International Congress on Rock Mechanics. Paris, pp. 655–660.

Serafim, J., Pereira, J., 1983. Considerations of the geomechanics classification of Bieniawski, in: International Symposium on Engineering Geology and Underground Construction. Lisbon, pp. 1133–1142.

Sheorey, P., 1997. Empirical rock failure criteria.

Singh, B., Goel, R., 2011. Engineering Rock Mass Classification. Elsevier. https://doi.org/10.1016/C2010-0-64994-7

Siratovich, P.A., von Aulock, F.W., Lavallée, Y., Cole, J.W., Kennedy, B.M., Villeneuve, M.C., 2015. Thermoelastic properties of the Rotokawa Andesite: A geothermal reservoir constraint. Journal of Volcanology and Geothermal Research 301, 1–13. https://doi.org/10.1016/j.jvolgeores.2015.05.003

Smith, A.G., Pells, P.J.N., 2008. Impact of fire on tunnels in Hawkesbury sandstone. Tunnelling and Underground Space Technology 23, 65–74. https://doi.org/10.1016/j.tust.2006.11.003

Somodi, G., Bar, N., Vásárhelyi, B., 2022. Correlation between the Rock Mass Quality (Q-system) method and Geological Strength Index (GSI), in: Fifth Symposium of the Macedonian Association for Geotechnics. Macedonian Association for Geotechnics, Ohrid, North Macedonia.

Tang, Z., Gao, K., Shan, Y., Zhu, C., Liu, Zeyi, Liu, Zimeng, 2022. Study of the Fire Behavior of Multilayer Cables in a Mine Tunnel. Energies (Basel) 15, 2059. https://doi.org/10.3390/en15062059

Tokashiki, N., Aydan, Ö., 2010. The stability assessment of overhanging Ryukyu limestone cliffs with an emphasis on the evaluation of tensile strength of rock

mass. Doboku Gakkai Ronbunshuu C 66, 397–406. https://doi.org/10.2208/jscejc.66.397

Trueman, R., 1998. n evaluation of strata support technique in dual life gateroads. University of Wales, Cardiff.

Turner, S., 2001. St Gotthard Tunnel Fire. New Civil Engineer 5–7.

Wang, F., Frühwirt, T., Konietzky, H., Zhu, Q., 2019. Thermo-mechanical behaviour of granite during high-speed heating. Eng Geol 260, 105258. https://doi.org/10.1016/j.enggeo.2019.105258

Wang, F., Konietzky, H., 2019. Thermo-Mechanical Properties of Granite at Elevated Temperatures and Numerical Simulation of Thermal Cracking. Rock Mech Rock Eng 52, 3737–3755. https://doi.org/10.1007/s00603-019-01837-1

Wang, F., Konietzky, H., Frühwirt, T., Li, Y., Dai, Y., 2020. Impact of cooling on fracturing process of granite after high-speed heating. International Journal of Rock Mechanics and Mining Sciences 125, 104155. https://doi.org/10.1016/j.ijrmms.2019.104155

Wasantha, P.L.P., Guerrieri, M., Xu, T., 2021. Effects of tunnel fires on the mechanical behaviour of rocks in the vicinity – A review. Tunnelling and Underground Space Technology 108, 103667. https://doi.org/10.1016/j.tust.2020.103667

XU, X., GAO, F., SHEN, X., XIE, H., 2008. Mechanical characteristics and microcosmic mechanisms of granite under temperature loads. Journal of China University of Mining and Technology 18, 413–417. https://doi.org/10.1016/S1006-1266(08)60086-3

Yertutanol, K., Akgün, H., Sopacı, E., 2020. Displacement monitoring, displacement verification and stability assessment of the critical sections of the Konak tunnel, İzmir, Turkey. Tunnelling and Underground Space Technology 101, 103357. https://doi.org/10.1016/j.tust.2020.103357

Yuan, L., Mainiero, R.J., Rowland, J.H., Thomas, R.A., Smith, A.C., 2014. Numerical and experimental study on flame spread over conveyor belts in a large-scale tunnel. J Loss Prev Process Ind 30, 55–62. https://doi.org/10.1016/j.jlp.2014.05.001

Yudhbir, Lemanza, W., Prinzl, F., 1983. An Empirical Failure Criterion For Rock Masses , in: 5th ISRM Congress. Melbourne.

APPENDICES

A. Stress-Strain Curves for Static Deformability Tests

The stress-strain curves for static deformability tests are given in this section. Graphs represent the changes in axial stress with increasing axial strain for various temperature levels for 1, 7, and 14 days.

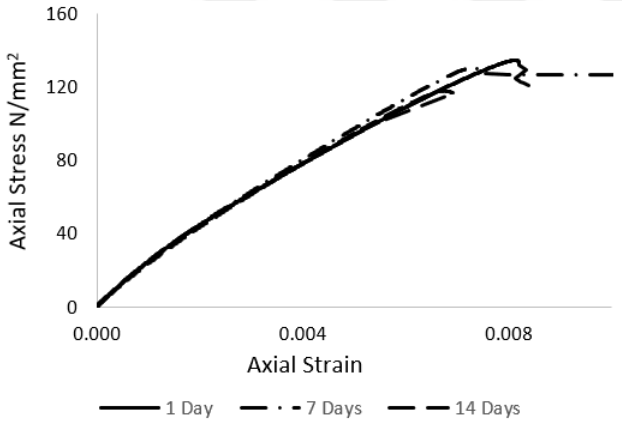

Figure A.1. Stress-strain curve for static deformability test at 100°C.

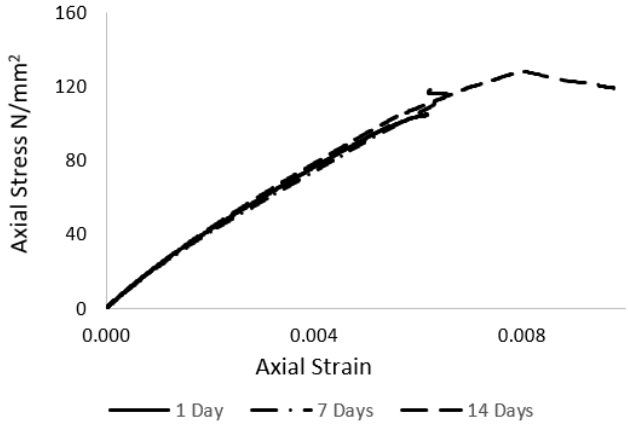

Figure A.2. Stress-strain curve for static deformability test at 200°C.

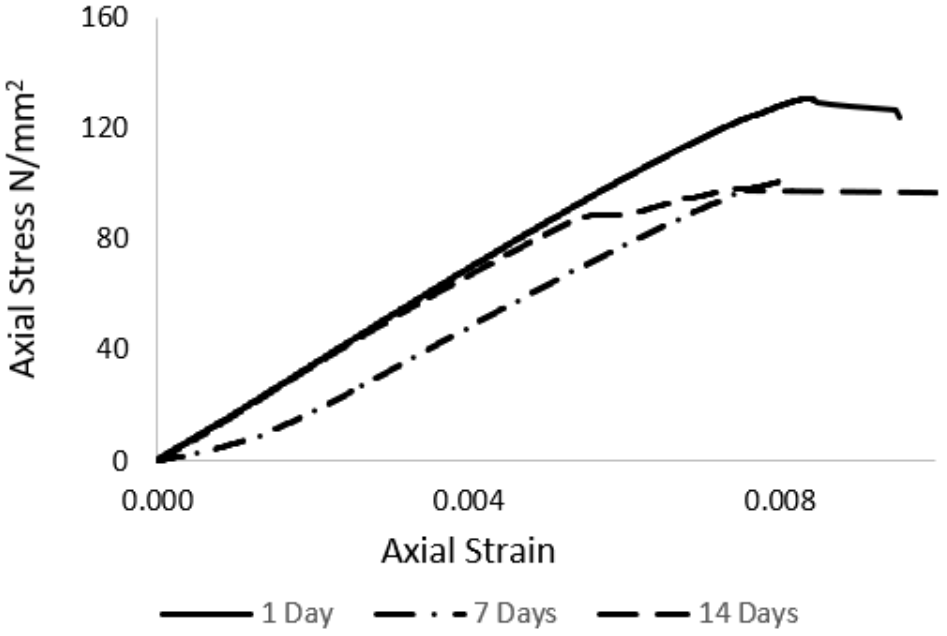

Figure A.3. Stress-strain curve for static deformability test at 400°C.

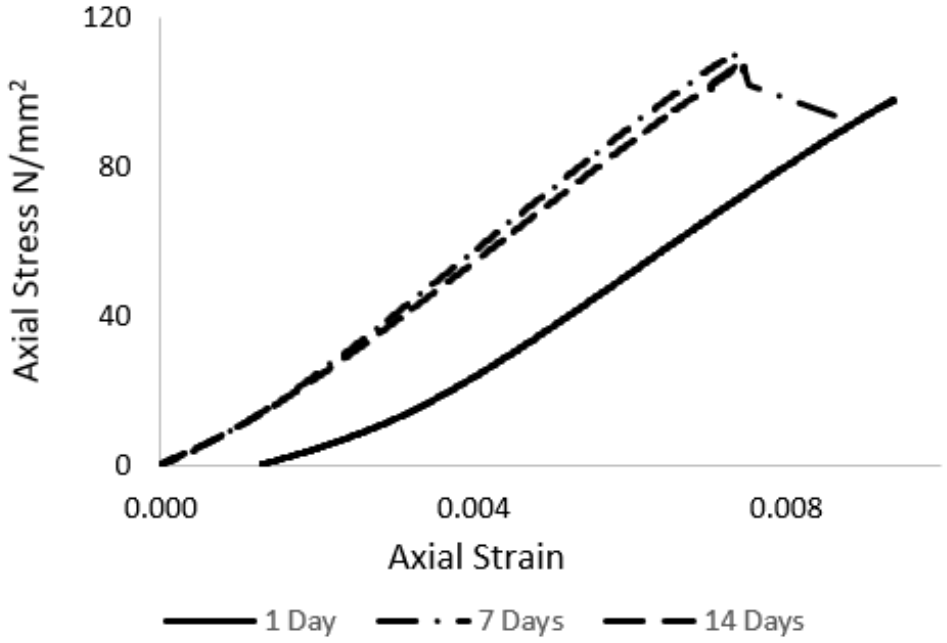

Figure A.4. Stress-strain curve for static deformability test at 600°C.

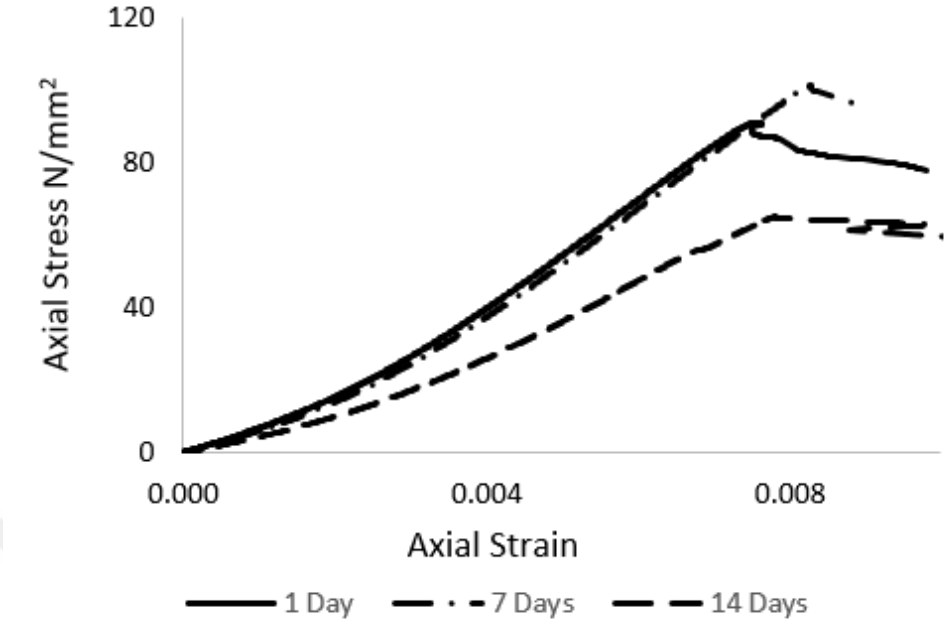

Figure A.5. Stress-strain curve for static deformability test at 800°C.

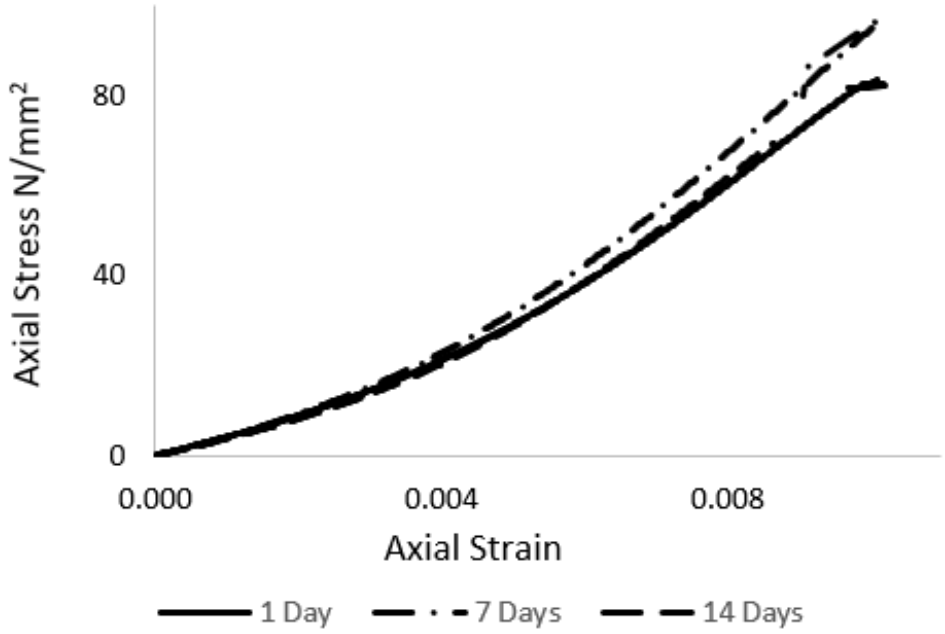

Figure A.6. Stress-strain curve for static deformability test at 1000°C.

B. Stress-Strain Curves for Triaxial Compression Tests

The stress-strain curves for triaxial compression tests are given in this section. The graphs represent the change in axial stress with increasing axial strain for a lateral compression values of 5 MPa, 10 MPa, and 15 MPa.

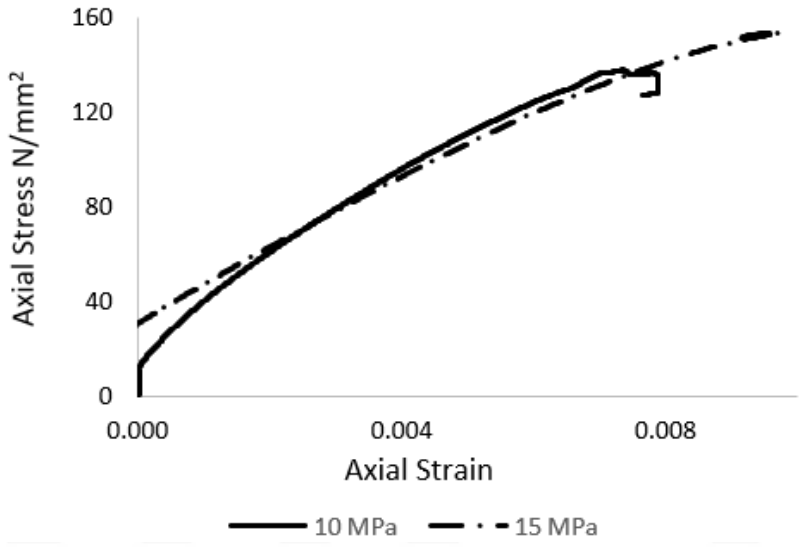

Figure B.1. Stress-strain curve for triaxial compression test at 100°C.

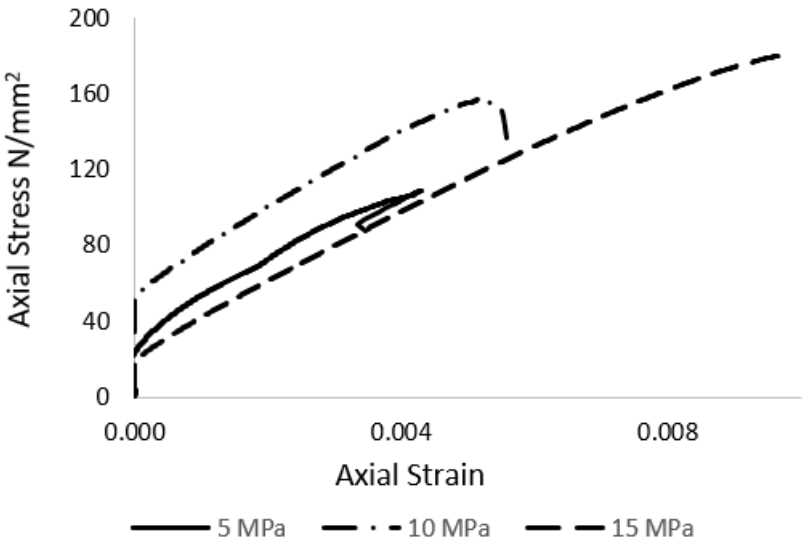

Figure B.2. Stress-strain curve for triaxial compression test at 200°C.

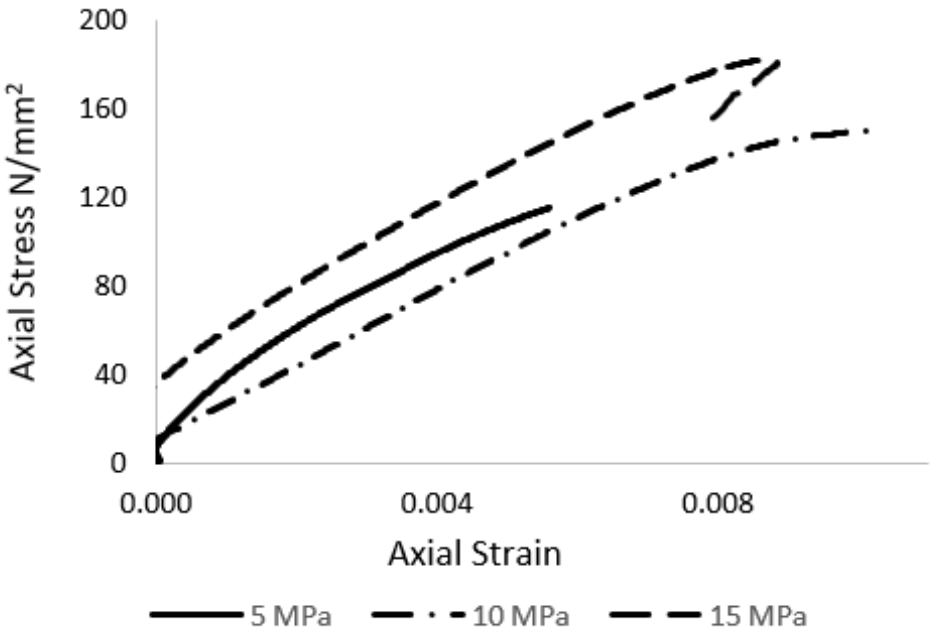

Figure B.3. Stress-strain curve for triaxial compression test at 400°C.

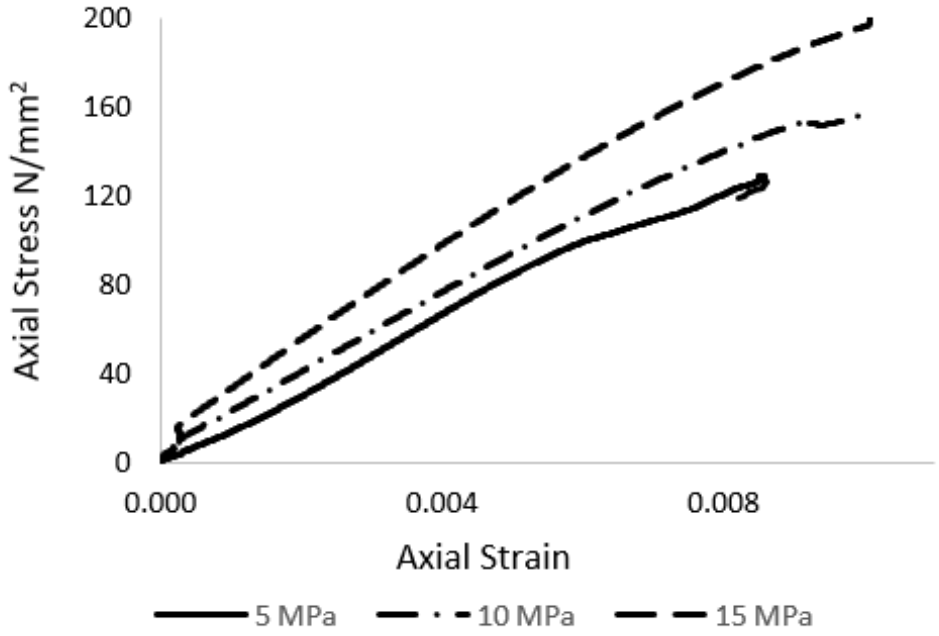

Figure B.4. Stress-strain curve for triaxial compression test at 600°C.

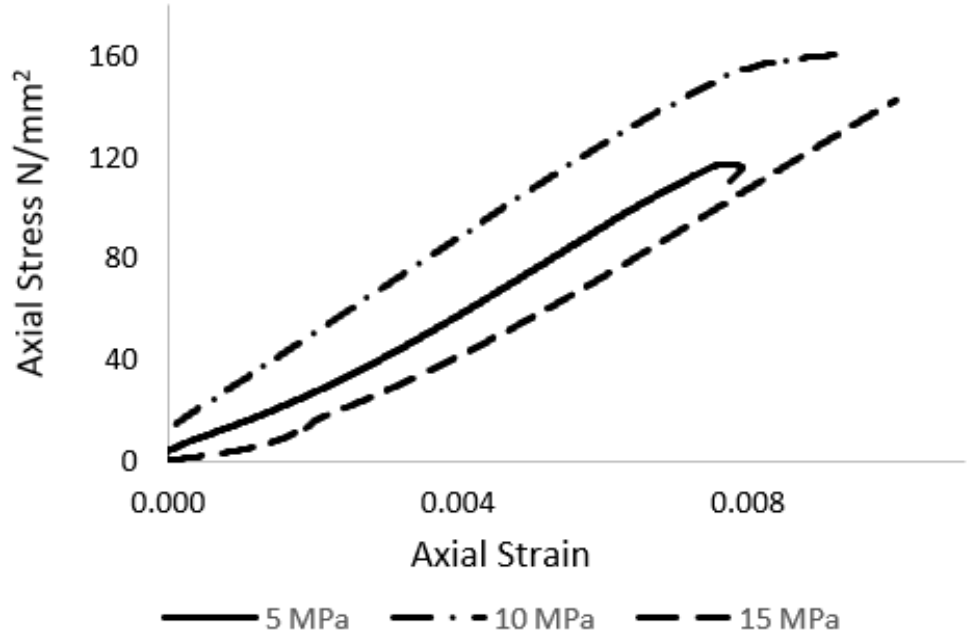

Figure B.5. Stress-strain curve for triaxial compression test at 800°C.

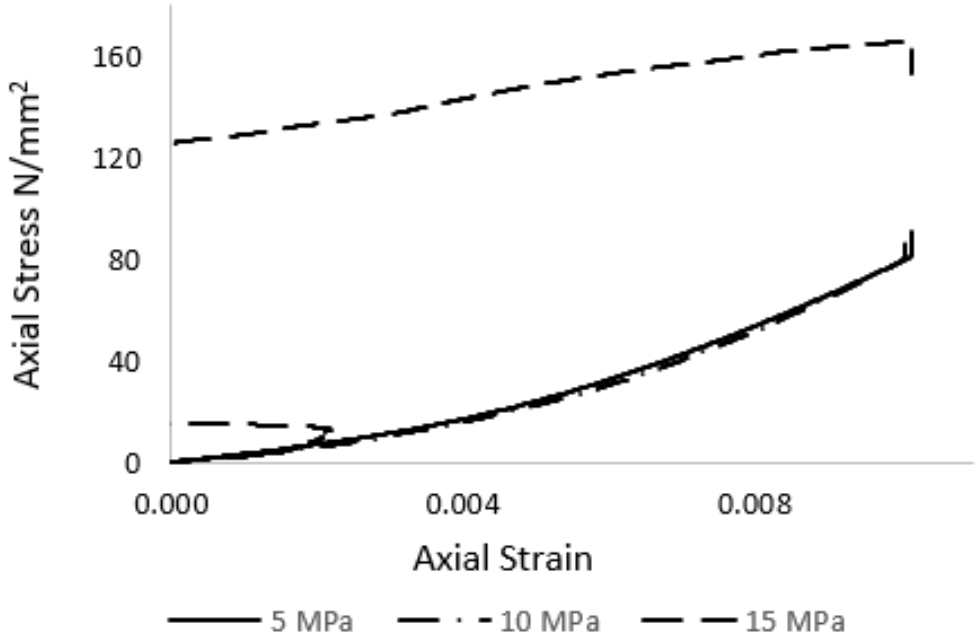

Figure B.6. Stress-strain curve for triaxial compression test at 1000°C.

C. Total Displacement Contours for Coupled Thermo-Mechanical Models

The total displacement contours around the fire-affected excavations in small-scale fire as well as large-scale fire cases are given in this section. The figures show the total displacement for VGQRM, GQRM, and FQRM at RT, 400°C, 800°C, and 1200°C for small-scale fire as well as at 1200°C for the case of a large-scale fire.

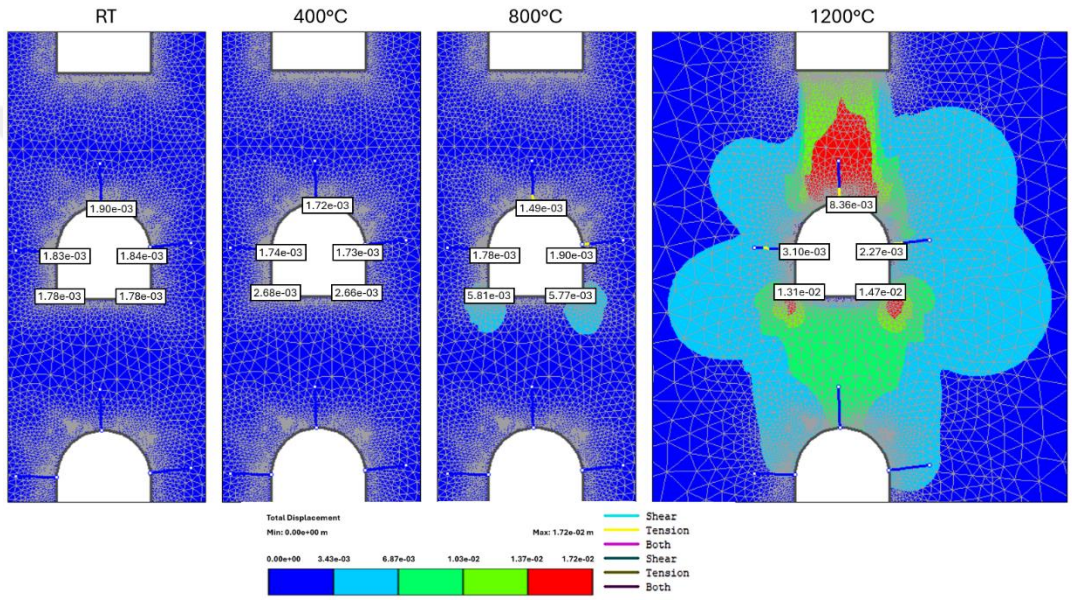

Figure C.1. Displacement contours around the fire zone (L2) at RT, 400°C, 800°C, and 1200°C in VGQRM in small-scale fire.

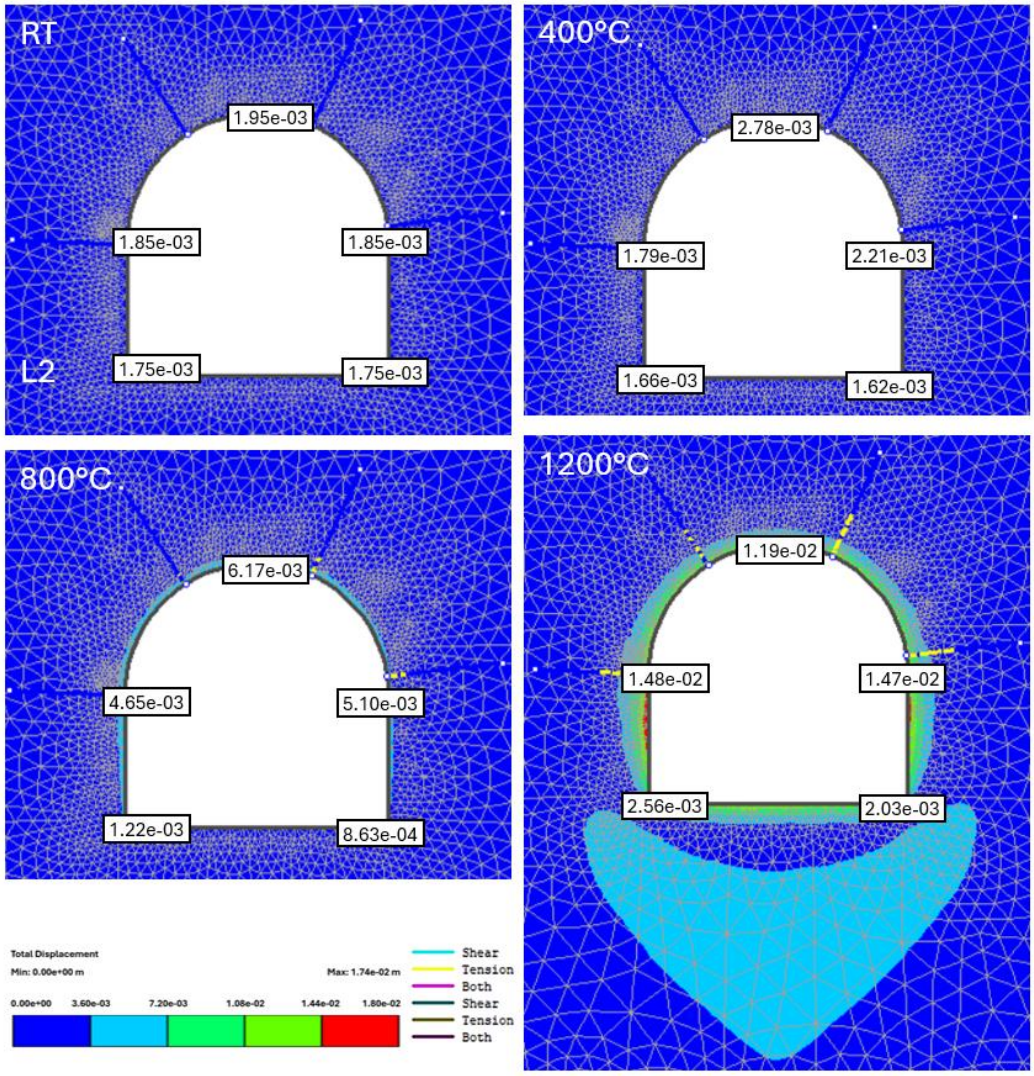

Figure C.2. Displacement contours around the fire zone (L2) at RT, 400°C, 800°C, and 1200°C in GQRM in small-scale fire.

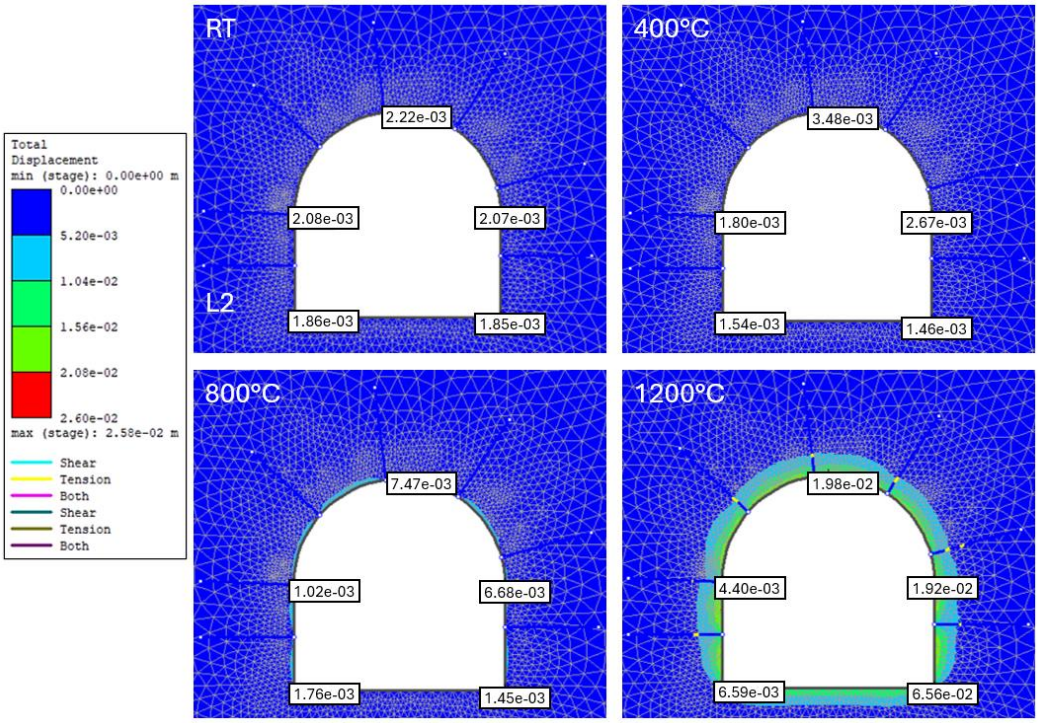

Figure C.3. Displacement contours around the fire zone (L2) at RT, 400°C, 800°C, and 1200°C in FQRM in small-scale fire.

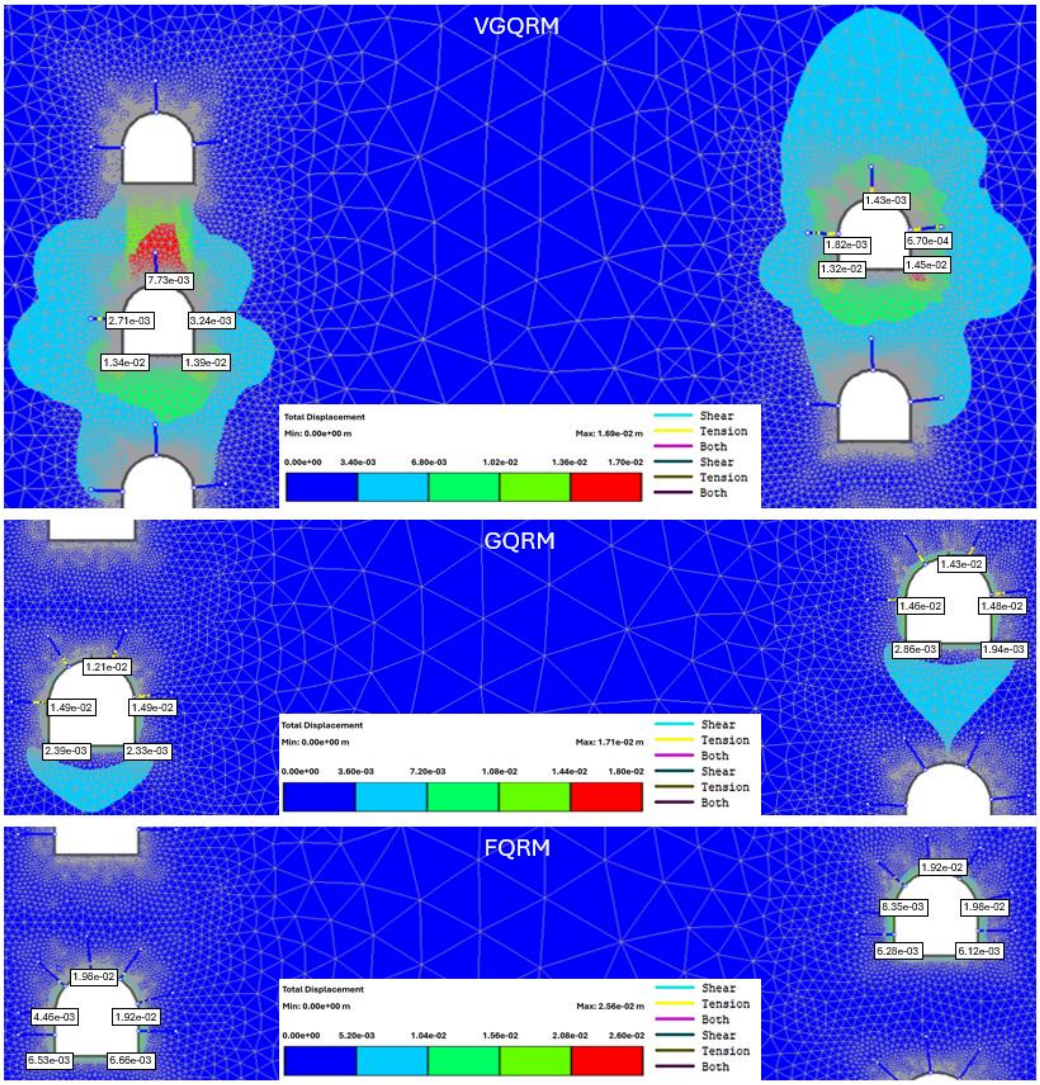

Figure C.4. Displacement contours around the fire zones (L2 and R1) at 1200°C in all three rock mass quality classes in large-scale fire conditions.